In Silico Tools for Investigating the Performance of Breast Cancer Imaging Technologies

by

Aunnasha Sengupta

A dissertation submitted in partial fulfillment
of the requirements for the degree of
Doctor of Philosophy
(Electrical and Computer Engineering)
in The University of Michigan
2022

Doctoral Committee:

Dr. Aldo Badano, Co-Chair
Professor Heath Hofmann, Co-Chair
Professor Jeffrey Fessler
Professor Lubomir Hadjiyski
Professor Pei-Cheng Ku
Professor Douglas Noll

Aunnasha Sengupta
aunnie@umich.edu
ORCID ID: 0000-0001-7102-6193

For all people

ACKNOWLEDGEMENTS

First and foremost, I would like to thank Dr. Aldo Badano and Prof. Hofmann for giving me this opportunity to continue my thesis work. Their leadership and guidance has been invaluable for pursuing novel ideas and producing good quality work in a timely fashion. I would also like to thank all members of the committee for taking the time to review my work.

Many thanks to the members of the VICTRE team at the US food and Drug Administration: Miguel Lago, Andreu Badal, Andrey Makeev, Rongping Zeng and Diksha Sharma for their help and support. Advice and constructive criticism that I received through discussions with the team was essential for developing my doctoral research.

Finally, I'd like to thank my husband and parents who have been my constant source of support and motivation.

TABLE OF CONTENTS

LIST OF FIGURES

Figure

LIST OF TABLES

Table

ABSTRACT

Breast cancer screening programs using two dimensional (2D) digital mammography (DM), have proven effective in early detection of cancer subsequently reducing breast cancer related deaths. A major drawback of DM arises from large amounts of overlapping breast tissues which may mimic or conceal abnormalities in a 2D image. Advanced breast imaging technologies like digital breast tomosynthesis (DBT) generating 3D information are now being considered as a replacement for DM in screening programs. However, the benefits of DBT based screening for earlier detection of cancer, across the various commercially available detector technologies, are yet to be established. The aim of this thesis is to investigate the influence of x-ray imager technologies and imaging modalities on the early detection of breast cancer using in silico trials. The first part of this thesis focuses on developing computational models that replicate the growth of cancerous lesions and the detector physics of commercially available DM/DBT systems. I propose a growth model for breast lesions based on biological and physiological phenomena accounting for the stiffness of surrounding anatomical structures. Depending on the breast local anatomical structures, a range of unique lesion morphology was realized. Imaging physics models were developed to simulate direct and indirect x-ray detector technology. Image quality metrics were compared against measured data from three commercially available DM/DBT systems. Finally, these tools combined with the VICTRE 1.0 in silico framework were used to design in silico trials to study whether DBT can facilitate the detection of breast cancer at earlier disease stages and for a range of detector technologies. The in silico studies suggest that while DBT shows clear advantages for detecting masses

at earlier stages, its benefits over DM for detecting micro-calcifications depend on the detector technology.

CHAPTER I

Introduction

1.1 Breast cancer and screening

Cancer remains the biggest hurdle towards increasing life expectancy in most countries across the world (*Bray et al.*, 2021). Several factors contribute to the increasing cancer incidence and mortality rates, such as population growth, aging as well as the distribution of risk factors, which vary with socioeconomic factors across the world. Compared to the 2018 reports (*Sung et al.*, 2020), female breast cancer (11.7%) has now overtaken lung cancer (11.4%) as the most commonly diagnosed cancer worldwide, as per the 2020 Globocan Cancer Statistics (*Sung et al.*, 2020) (see fig. 1.1 (a)). Amongst women, breast cancer is the most commonly diagnosed cancer worldwide (24.5%) and leading cause of cancer related deaths (15.5%) (*Sung et al.*, 2020).

The distribution of cancer related deaths amongst women, as shown in fig. 1.1 (b), reveals that although breast cancer incidence rates are high in developed countries in north America and western Europe, it is not the leading cause of cancer mortality among women. A breast cancer diagnosis is more likely to lead to mortality in the developing countries of the world. Developing countries account for 50% of the breast cancer cases and 60% of the deaths (*Jemal et al.*, 2011; *Bray et al.*, 2018). Although the incidence rates are lower in the developing countries, the mortality to incidence

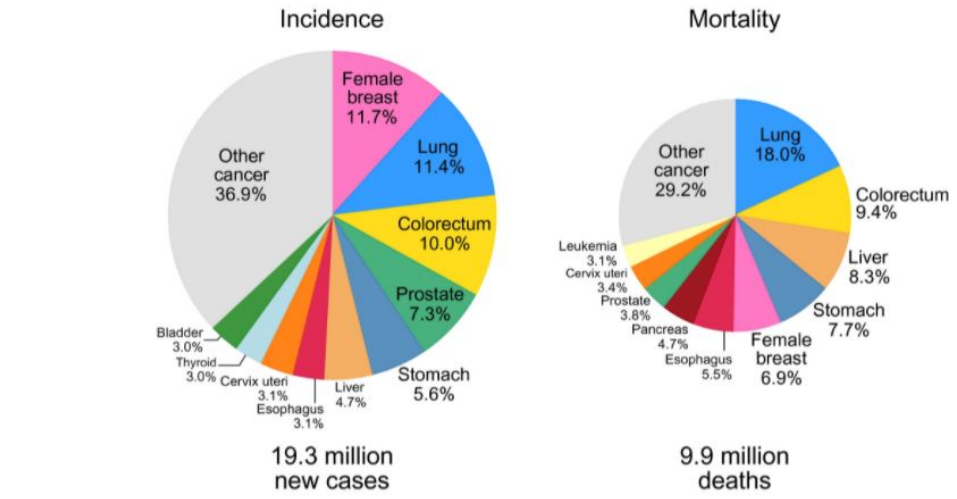

(a)

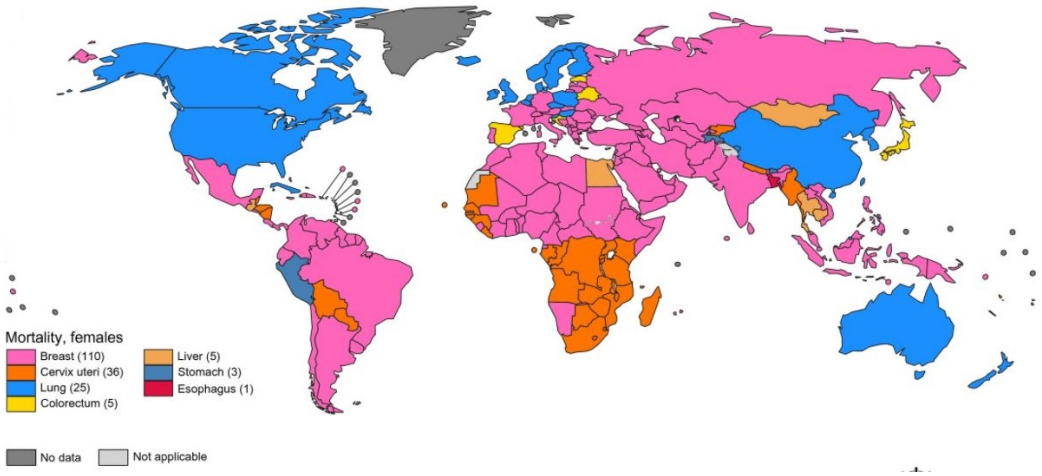

(b)

Figure 1.1: (a) Distribution of incidence and mortality rates for the top 10 most cancers and (b) most common cancer mortality amongst women worldwide. source: Globocan Cancer Statistics 2020 (*Sung et al.*, 2020)

ratio is much higher. In countries like India, the breast cancer incidence rate in 2017 was found to be 25.8 in 100,000 women and the mortality rate of 12.7 per 100,000 women (*Madhav et al.*, 2018). Moreover, the 5-year survival rate during 2010-2014 was found to be 66.1% in India, the lowest among 71 other countries that were surveyed (*Allemani et al.*, 2018). In comparison, the 5-year survival rates in developed countries like Australia and the USA were 89.5% and 90.2% respectively.

In general, the prognosis for a breast cancer diagnosis is good when detected at an early stage. In countries like India, only 5% of the diagnosed breast cancer cases are found to be in their earlier stages. This, combined with limited access to a good healthcare system, accounts for the higher mortality rates observed in these countries. Breast cancer screening programs have been recognized as an effective tool for early detection of cancer. In Brazil, introduction of a regional breast cancer screening program, resulted in an increased (from 14.5% to 43.2%) cancer detection rate at earlier stages. Additionally, several randomized clinical trials conducted across Europe and North America (*Nystrom et al.*, 1993; *Shapiro et al.*, 1988; *Moss et al.*, 1992; *Lee et al.*, 2010; *Duffy et al.*, 2002) concluded that the lower mortality rates in these countries are a direct consequence of detection of cancer at earlier stages facilitated through breast cancer screening programs.

1.2 Imaging for breast cancer screening

Currently, there are 4 diagnostic imaging technologies that are used for the detection of breast cancer: namely, breast tomosynthesis, mammography, magnetic resonance imaging (MRI), and ultrasound. MRI uses strong oscillating magnetic fields to render images of the breast. While this technique has high sensitivity to cancerous tumors it also can generate many false positives. Thus, it may not be suitable for screening programs but may be used as a supplemental imaging modality for women with extremely dense breasts (with a high content of fibroglandular tissues) (*Bakker*

et al., 2019). Breast ultrasound mainly relies on generating images using echos reflected from different tissues. This technique is extremely useful for differentiating between benign cysts and solid masses (*Stafford and Whitman*, 2011), which are usually cancerous. Digital breast tomosynthesis (DBT) and mammography (DM), are both based on generating x-ray images of the breast. DM is the current gold standard for imaging techniques used in breast cancer screening (*Marconi et al.*, 2019).

1.2.1 Digital Mammography

A mammogram is basically a 2-D x-ray image of the breast. This imaging technology relies on the fundamental idea that normal and cancerous tissues differ in their x-ray attenuation properties, leading to varying contrast levels in the DM image. The x-ray energy levels used for DM are chosen based on linear attenuation coefficients (μ) of healthy and cancerous breast tissues. A healthy human breast mainly consists of two types of tissues - adipose and glandular. While there is a large difference between the μ values for the adipose and cancerous tissues for a range of energy levels (*Bushberg et al.*, 2012), it is a much narrower gap for glandular tissues, especially for x-ray energy levels greater than 30 keV. It has also been shown that a higher contrast for ductal carcinoma relative to a glandular background can be achieved with low energy x-rays (*Bushberg et al.*, 2012). Hence mammograms generated using low-energy x rays (18-42 kVp) (*Boone et al.*, 1997), are an effective tool for detecting cancerous tumors.

Fig 1.2 (a) shows a general setup for the image acquisition process in DM. The x-ray photons transmitted or scattered by the compressed breast tissues impinge upon the x-ray detector after passing through the anti-scatter grid. These x-ray photons are absorbed by the x-ray detector and converted into electrical signals, which are then processed to create the 2D digital mammogram.

Since its introduction mammography has proven to be very effective in detection

of breast cancer. In certain populations it has been found to achieve high sensitivity values of 90.5% - 92.5 % (*Jacobsen et al.*, 2015). However, mammography is also extremely sensitive to breast density. It has been shown that for women with extremely fatty breasts, DM could achieve a sensitivity and specificity of 87.0% and 96.9% respectively. On the other hand, for women with extremely dense breasts, both the sensitivity and specificity reduced to 62.9% and 89.1% respectively (*Carney et al.*, 2003). High breast density basically means that the ratio of fibroglandular to adipose tissues is very high. As shown in fig. 1.2 (a), in a 2D x-ray image of the breast, as is the case with mammography, the presence of a large amount of overlapping fibroglandular tissues can mimic the presence of a cancerous lesion or hide underlying masses. This leads to higher false positives and negatives, observed in women with dense breasts. This is one of the major shortcomings of DM technology. Advanced versions of DM, DBT, have now been introduced to overcome these shortcomings.

1.2.2 Digital Breast Tomosynthesis

This method is very similar to DM, except that the x-ray tube in DBT systems is not stationary and instead moves in an arc (15-50°) (*Mackenzie et al.*, 2017) as shown in Fig 1.2 (b). As illustrated in the figure, if the x-ray tube is stationary, two overlapping objects of interest, appear as one in the 2D DM image. However, if the x-ray tube moves in an arc, it is possible to resolve the two objects in the projection views - wider the angle, better the resolution. These low-dose projection views are then reconstructed to create a volume of slices, each containing the breast information at various depths. Viewing the breast information in a slice by slice manner thus helps remove any ambiguity that may arise from overlapping layers of fibroglandular tissues.

As compared to DM, the introduction of DBT has been shown to increase the cancer detection rate by 15–30% and reduce the recall rate decreases by 15–20%

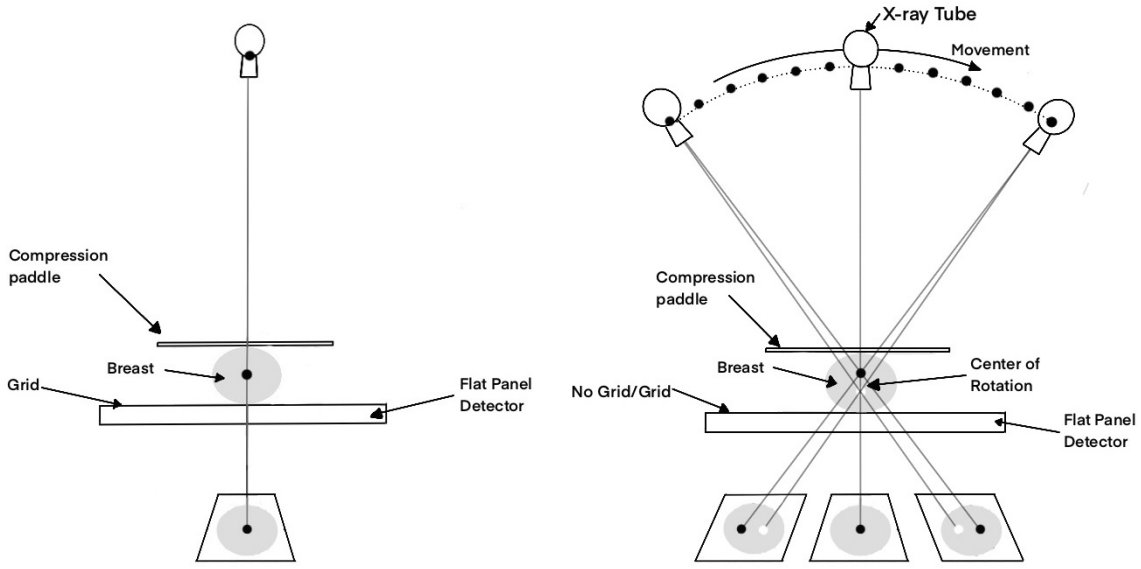

Figure 1.2: Image acquisition process for (a) DM and (b) DBT.

(*Iranmakani et al.*, 2020). Especially for non-calcified masses, DBT can not only increase the cancer detection rate (*Su et al.*, 2017; *Zuley et al.*, 2013), but also improve the diagnostic accuracy as compared to DM (*Su et al.*, 2017). It has also been found that for women with higher breast density, the sensitivity of DBT combined with 2D mammography (93%) was higher than just mammography (86%) (*Gilbert et al.*, 2015). Furthermore, it has been shown that using a combination of DBT and DM in screening programs can significantly improve the breast cancer detection rate, as compared to DM alone (*Rafferty et al.*, 2018; *Skaane et al.*, 2013; *Ciatto et al.*, 2013). Currently, DBT is also being considered as a replacement for DM in cancer screening programs. However, to do so, the benefits of DBT over DM for breast cancer breast screening with the goal to detecting cancer at its earlier stages, must be clearly demonstrated.

Although higher cancer detection rates in dense breasts can be achieved with the use of DBT, it has not been yet proven to reduce the incidence of interval cancers

(*Sechopoulos and Athanasiou*, 2020). It may be possible that since DBT is quasi-3D, obtaining projection views over a limited angular range, visibility of smaller lesions is still poor in DBT slices, especially for dense breasts. A true 3-D imaging modality, like dedicated breast computed tomography (CT), can overcome many of the limitations of DBT. Moreover, even though many studies have shown that the combination of DBT with DM can improve the cancer detection rate even for dense breasts, the same cannot be concluded about false positive rates. The results of the To-Be trial (*Wei et al.*, 2017) showed that while the use of DBT with SM (synthetic mammography, which is similar to DM, but generated using DBT data) reduced recall rates in low density breasts as compared to DM, the same was not the case for women with high density breasts. This would mean that using DBT with SM as compared to DM alone result in equivalent false positive rates. Finally, while it has been shown that DBT can improve cancer detection, it has not been determined whether increased cancer detection leads to lower mortality (*Jatoi and Pinsky*, 2020). In fact, it can result in over-diagnosis of non-lethal cancers and treatment-related mortality (*Jatoi and Pinsky*, 2020). So for all the reasons outlined above, it is evident that additional studies are required to justify whether the advantages of DBT for breast cancer screening outweigh the additional costs and training associated with it.

The National Cancer Institute–funded Tomosynthesis Mammographic Imaging Screening Trial (TMIST) (*Pisano*, 2018; *Lee and McCaskill-Stevens*, 2020) aims at addressing these concerns. The main outcome of the TMIST trial is to ascertain whether the use of DBT in screening programs can enable radiologists to find aggressive cancers at earlier stages, as compared to DM. This would allow doctors to remove the cancers before they can advance, and thereby reduce the number of advanced cancers in the population. The ultimate goal of the TMIST trial is to ascertain the choice of imaging modality best suited for breast cancer screening programs (*Lee and McCaskill-Stevens*, 2020). TMIST, the largest cancer screening trial funded by

NCI, is currently underway and involves enrolling over 100,000 women across several sites throughout North America. This study will include all the commercially available DBT/DM systems, that have received FDA approvals (*Pisano*, 2018) to ascertain whether the study outcomes depend on technology. However, this study is not expected to report its findings anytime in the near future (*Bell*, 2020).

The goal of this thesis is to investigate a limited version of TMIST using in silico imaging methods: (i) the effect of imaging modalities on the early detection of cancer and (ii) the effect of detector technology on cancer detection. In contrast to TMIST, we attempt to investigate these topics using a fast and cost-effective approach that does not involve irradiating asymptomatic women, by conducting these experiments in silico.

1.3 Available in silico frameworks

Traditionally, to investigate the effect of imaging modalities, imaging systems and intrinsic detector properties, lengthy clinical trials are conducted. These studies are time consuming and expensive. Such trials involve exposing asymptomatic women to unnecessary radiation and significantly slow down the regulatory process delaying patient access to advanced technologies. Every time there is a new idea or improvement in the imaging system or component, a technological iteration, it would not be possible to design and conduct another clinical trial. A faster and cost-effective alternative would be to implement sophisticated computational techniques, as a preclinical validation step to conduct such studies.

So far, VICTRE (*Badano et al.*, 2018; *Sharma et al.*, 2019) and OpenVCT (*Bakic et al.*, 2018) are the two available frameworks for conducting in silico trials involving breast imaging modalities. The limitations of the OpenVCT framework as compared to VICTRE arise from the implementation of (i) x-ray transport without scatter,(ii) an ideal detector model, (iii) breast masses without spiculations, (iv) low resolution

breast phantoms (0.1-0.2 mm spatial resolution), and (v) lack of detection rates corresponding to each breast density category. The goals for both in silico trials were to compare the performance of DBT and DM in detecting masses and calcifications. They arrived at similar conclusions that while higher detection rates for non-calcified masses can be achieved with DBT, detection of lesions with calcifications is comparable to DM. Other frameworks (*Elangovan et al.*, 2016b; *Vancoillie et al.*, 2020) that replicate the DBT image formation process have also been reported. However, they are yet to implement model observers and hence cannot be used to conduct completely in silico trials.

The work described in this thesis builds on the VICTRE (*Badano et al.*, 2018; *Sharma et al.*, 2019) framework and adds lesion growth and detector models to study the effect of imaging modality, x-ray detector and cancer progression on the final detection task.

1.4 Thesis Outline

In summary, this thesis will investigate the influence of x-ray imager technologies and imaging modalities (digital breast tomosynthesis (DBT) and digital mammography (DM)) on the early detection of breast cancer. Specifically, we will be addressing some of the aims of the TMIST trial, such as (i) evaluate DBT as a replacement for DM across different commercially used x-ray detector technologies and (ii) determine if DBT can detect breast cancer at earlier stages as compared to DM. None of these studies have been done before and are vital to determine if DBT can reduce the incidence of advanced cancers by detecting them at earlier stages. These studies will be extremely useful to make recommendations for breast cancer screening programs, in terms of the imaging modality of choice.

To perform these studies, we need to develop in silico frameworks that can replicate the different detector technologies and have a provision to include the growth

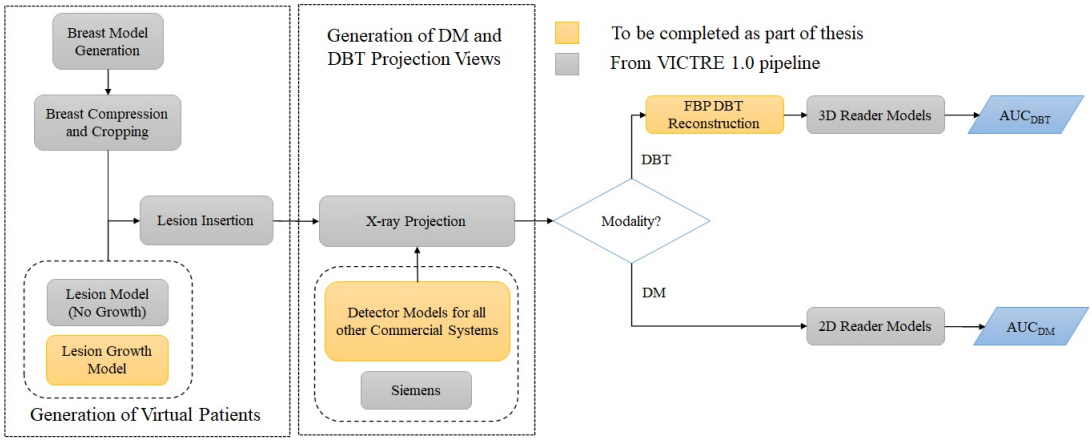

Figure 1.3: Contributions to the VICTRE 1.0 pipeline

of cancerous tumors. Currently, none of the in silico frameworks, described in the previous section have these capabilities. The first goal (Chapters 2 and 3) will be to develop new in silico tools that are required for our investigations. Fig. 1.3 illustrates the current VICTRE 1.0 platform and the modules that will be improved as part of this thesis. To study how breast cancer evolves in the in silico version, 3D models that mimic tumor growth and progression were developed (chapter 2). The imaging physics module in the VICTRE 1.0 pipeline, which currently emulates the Siemens DBT system, was adapted to mimic other commercially available systems in terms of detector technology and acquisition geometry (chapter 3). Chapter 4 describes the development of an open source version of filtered back-projection (FBP) reconstruction for DBT. The next half of the dissertation (Chapter 5 and 6) focuses on investigating the impact of detector technology and imaging modality on the detection of breast cancer using the tools developed in the earlier chapters. We first studied the performance of the commercially available systems. Specifically, we integrated the physics models developed in Chapter 3 with the breast, lesion and reader models from the VICTRE 1.0 pipeline for this study. The two main objectives of the study were to ascertain whether DBT outperforms DM across the different detector technologies and whether the type of imaging detector (direct vs indirect) has any

significant influence on the task of cancer detection.

1.4.1 Chapter 2: Simulating breast cancer progression

This chapter introduces a 3D voxelized breast lesion model representing different stages of growth. Several approaches (*Dukov et al.*, 2019; *Bliznakova et al.*, 2019, 2003; *de Sisternes et al.*, 2015) have been reported in the past for simulating 3D voxelized breast lesions, as shown in fig. 1.4. These models can be categorized as parameterized or patient derived. Parameterized models are developed using simple mathematical or analytical equations to describe the shape or surface of the lesions (see fig. 1.4 (a) to (d)). These lesions are described using either simple shapes like spheres or ellipsoids (*Bliznakova et al.*, 2003), random walk algorithms (*Hintsala et al.*, 2009), diffusion limited aggregation algorithms (*Rashidnasab et al.*, 2013) or a Gaussian sphere model (*de Sisternes et al.*, 2015). While these models allow flexibility in terms of resolution and range of lesion morphology, realism is a major concern. To address this concern, Dukov et al. (*Dukov et al.*, 2019) introduced the patient derived model, which uses real images of breast cancer cases. The lesions are segmented from patient images generated using 3D imaging modalities like DBT and CT. The 2D lesion slices are then stacked to create the final lesion morphology. While this approach may generate more realistic lesions, it suffers from several shortcomings, including limited resolution of the tumor model, limited number of lesion shapes, and the need to establish institutional review board (IRB) approvals for obtaining patient data. Moreover, none of these previous approaches can be extended to incorporate growth as they are not based on any biological phenomena.

In comparison to the previous efforts, the work described in this chapter accounts for the biological factors that can affect the growth and morphology of the tumor such as interstitial tumor pressure, diffusion of metabolites as well as stiffness of the surrounding tissues. This chapter builds on a previously reported model (*Tang et al.*,

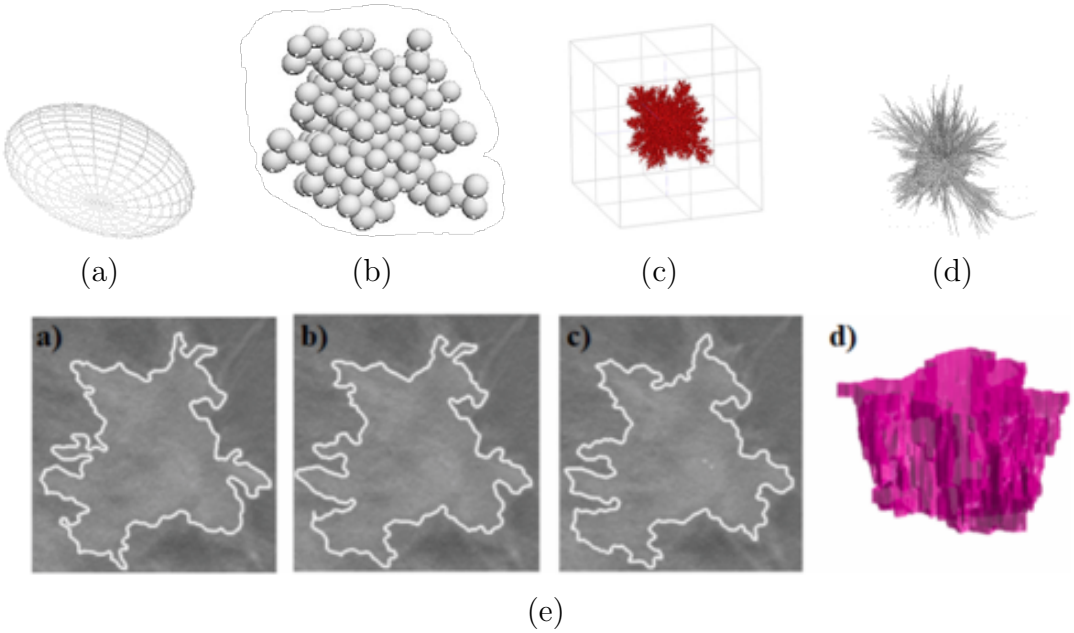

Figure 1.4: Lesion models based on (a) simple shapes like ellipsoids (image source: *Bliznakova et al.* (2003)), (b) random walk algorithms, (image source: *Hintsala et al.* (2009)) (c) diffusion limited aggregation algorithm (image source: *Rashidnasab et al.* (2013)), (d) Gaussian sphere model (image source: *de Sisternes et al.* (2015)) and (e) patient data (image source: *Dukov et al.* (2019))

2014), incorporating the effect of the stiffness of local anatomical structures on the final lesion morphology. The model allows preferential proliferation of tumor cells in the more elastic regions of the breast like pockets of adipose tissues, while stunting their growth through stiffer structures like ligaments. This approach allows growth of realistic lesions informed by their local anatomical features.

1.4.2 Chapter 3: Modeling x-ray detector physics

Table. 1.4.2 describes all the commercially available DM/DBT systems that have received FDA clearance. Currently there are two types of x-ray detector technologies that are used in these systems - direct (based on amorphous selenium (a-Se)) and indirect (based on cesium iodide (CsI:Tl)). Currently, a-Se is the photoconductor of choice for x-ray imagers in most FDA approved DBT and DM systems such as the

Hologic Selenia Dimensions, the Siemens MAMOMAT Inspiration and the Fujifilm Innovality (*Mackenzie et al.*, 2017) as reported in table 1.4.2.

Manufacturer	Siemens Inspiration	GE Senographe Pristina	Hologic Selenia Dimensions	FujiFilm Innovality
Pixel Pitch (μm)	85	100	70	50
Detector	a-Se	CsI	a-Se	a-Se
Detector Thickness (μm)	200	250	200	200
Number of DBT Projections	25	9	15	15
Angular Range	50°	25°	15°	15°
Anode/Filter	W/Rh	Mo/Rh	W/(Rh or Al)	W/(Rh or Al)
Filter thickness(mm)	0.05	0.025	0.05 (Rh) or 0.5 (Al)	0.05 (Rh) or 0.7 (Al)
SID (cm)	65.5	66	70	65

Table 1.1: Description of all FDA approved DBT systems (*Mackenzie et al.*, 2017; *Sechopoulos*, 2013). (SID stands for source to imager distance)

Direct detectors, as shown in fig. 1.5, using x-ray sensitive materials like amorphous selenium (a-Se), convert the incident x-ray photons to electric charge. A fraction of the incident x-rays, determined by the thickness and attenuation coefficient of Se, is absorbed in the a-Se detector layer. Each absorbed x-ray photon creates a primary photo-electron through the photo-electric effect(*Que and Rowlands*, 1995a). This primary electron carries a large amount of kinetic energy and as it travels through the Se layer, it collides randomly with Se atoms and creates thousands of secondary electron–hole pairs, until all its kinetic energy is lost. The high electric field generated across the detector, causes the electrons and holes to drift along the field lines to be collected by the pixel and top electrodes, respectively. The electronic charges are collected and accumulate on the pixel capacitor and finally read out using back-end electronics.

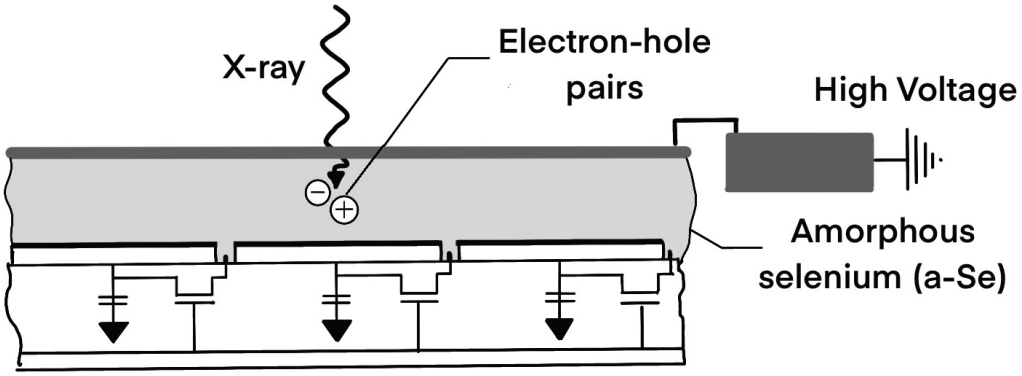

(a)

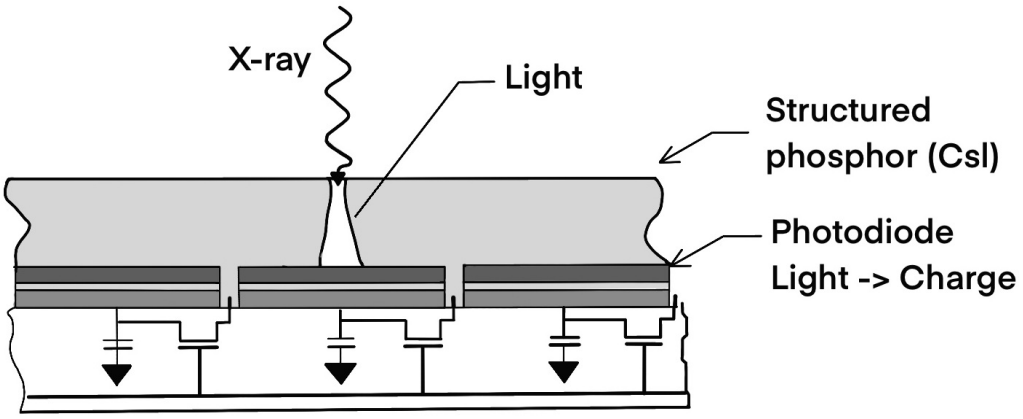

(b)

Figure 1.5: Cross-sections of (a) direct and (b) indirect x-ray detectors.

Indirect x-ray detectors based on scintillating materials like thallium-doped cesium iodide (CsI:Tl) convert the incident x-ray energy to charge in a two step process. These detectors first absorb the incident x-ray energy and convert it into optical photons. The photo-electric effect is also the main x-ray interaction in CsI:Tl detectors (*Yaffe and Rowlands*, 1997)). However, instead of creating secondary electron-hole pairs, the primary electrons generate light quanta. The optical photons are then converted into electric charge by a large photodiode array. The charge stored on the storage capacitor is then read out using back end electronics, similar to the a-Se based direct detector.

Our group recently reported on an in silico version of the SIEMENS Mammomat Inspiration DM and DBT system using an open source GPU-accelerated Monte Carlo x-ray imaging simulation code, MC-GPU (*Badal et al.*, 2020a). The MC-GPU code implements a realistic x-ray source model with the tomosynthesis acquisition geometry and a detector model for the direct-conversion a-Se detector. Chapter 2 builds on the previous version of the MC-GPU codes to mimic the imaging performances of two other FDA-approved DM/ DBT systems, such as Hologic Selenia Dimensions and the General Electric Senographe Pristina systems. Although the Hologic system also uses a direct-conversion detector, it suffers from resolution loss due to signal crosstalk. Similarly, spread of optical photons is typical in the CsI:Tl based indirect detector, used in the GE system. We improved on the current detector model to incorporate both these phenomena.

The performance of these models were evaluated by simulating standard image quality metrics used in clinical practice such as modulation transfer function (MTF), noise power spectrum (NPS) and detective quantum efficiency (DQE) and comparing them with measured data.

1.4.3 Chapter 4: Open source FBP reconstruction for DBT

This chapter describes the development of an open source version of the FBP reconstruction algorithm for DBT using single-threaded C. This is an extention to the C codes developed by Leeser et al. (*Leeser et al.*, 2014) for cone-beam computed tomography (CBCT) reconstruction, incorporating the differences in acquisition geometries between the two imaging technologies. The C based FBP implementation was tested using mathematical and anatomical phantom data and the results were compared with a previously verified MATLAB implementation. The C implementation resulted in significant improvements (up to 9 times) in computational speed over the MATLAB one, which is crucial for running large in silico trials.

1.4.4 Chapter 5: Investigating the link between DQE and cancer detectability

This chapter integrates computational models of different detector technologies, developed in chapter 3, with the VICTRE in silico pipeline to evaluate the effect of detector technology on breast cancer detection. One of the advantages of in silico approaches is that hypothetical systems can be modeled and compared. So to remove all other confounding and contributing factors, the same DM/DBT system geometry and x-ray acquisition parameters, modeled to mimic the Siemens Mammomat Inspiration system, was used to evaluate the three detectors. The effect of the detector technologies were evaluated for two manifestations of breast cancer: spiculated masses and micro-calcifications. This study allowed us to gain insight into the relationship between image quality metrics and the clinical performance that can be achieved with different detector technologies. While the relationship between detectors' image quality metrics and performance in DM may be well understood, the same cannot be concluded for DBT.

1.4.5 Chapter 6: The first ever longitudinal trial investigating breast cancer imaging techniques

Although the advantage of DBT for the detection of larger masses has been demonstrated through various studies, it remains to be seen if DBT offers similar benefits at earlier stages of cancer progression, when tumor sizes are smaller. To investigate this, this chapter describes first ever in silico longitudinal trial reported in literature. To mimic cancer progression, the computational model for simulating the growth of breast cancer lesions developed as part of chapter 2, were used. This model, integrated with the VICTRE pipeline is used to create a cohort of in silico patients each with an unique manifestation of cancer recorded at 5 stages of progression. Digital patients with varying breast densities, from dense to fatty are considered. This study demonstrated the benefits of DBT as compared to DM at earlier stages of tumor development.

CHAPTER II

In Situ Tumor Model for Longitudinal In Silico Imaging Trials

2.1 Abstract

In silico trials have garnered widespread support as an alternative way of evaluating novel imaging technologies as compared to lengthy and expensive clinical studies. To facilitate in silico studies for assessing the performance for earlier detection of cancer, a method to simulate tumor growth and morphological variations at various stages of disease is needed. We introduce a computational model for simulating the growth of breast cancer lesions based on biological and physiological phenomena accounting for the stiffness of surrounding anatomical structures. Ligaments are considered as the most rigid structures with a elastic modulus in the range of $8x10^4$-$4x10^5$ kPa (pressure multiplicative factor of 10^6), while fat (elastic modulus varying from 0.5 to 25 kPa, and pressure multiplicative factor of 10) and glandular tissues (elastic modulus varying from 7.5 to 66 kPa, and pressure multiplicative factor of 45) constitute the more elastic regions of the breast. In the model, tumor cells are less likely to grow through stiffer structures like ligaments and instead preferentially proliferate in the more elastic regions of the breast. Depending on the breast local anatomical structures, a range of unique lesion morphology can be realized. We modeled

the growth of simulated lesions within volumes extracted from 50 μm fatty breast models generated with the open-source, freely available VICTRE (Virtual Imaging Clinical Trials for Regulatory Evaluation) imaging pipeline. The imaging component of the VICTRE pipeline models the Siemens Mammomat Inspiration mammography system, which was used to generate the digital mammogram (DM) images for each breast model containing the lesions. Using these DMs, we show the imaging characteristics of the lesions blending with the anatomical backgrounds in DM images depicting several time points in the growth of the tumor.

2.2 Introduction

Three-dimensional (3D) digital breast tomosynthesis (DBT) is being considered to replace digital mammography (DM) as the imaging modality of choice in breast cancer screening programs. As compared to DM, DBT has been shown to increase the cancer detection rate by 15–30% and reduce the recall rate by 15–20% (*Iranmakani et al.*, 2020). Especially for non-calcified masses, DBT, compared to DM, not only can increase the cancer detection rate (*Su et al.*, 2017; *Zuley et al.*, 2013), but also improve diagnostic accuracy (*Su et al.*, 2017). However, the primary goals of breast cancer screening programs not only are to increase the cancer detection rate, but also to lower breast cancer-related mortality by reducing the number of advanced cancers in the population. Hence, it is imperative to establish whether DBT systems can replace DM for increasing the detection of aggressive cancers at earlier stages. Traditional clinical trials designed to conduct such studies usually are very lengthy, expensive and may involve exposing women to unnecessary radiation. Such trials can significantly slow down regulatory evaluation, delaying patients access to safe and effective advanced technologies. New concepts or technological improvements in the imaging system and its components are currently evaluated by designing and conducting new clinical trials. A faster and cost-effective alternative is the implementation of sophisticated

computational techniques, in silico trials (*Badano et al.*, 2018; *Bakic et al.*, 2018; *VICTRE Github Repository*, 2018), as an alternative source of regulatory evidence. The goal of our work, described in this paper, is to model the growth of breast lesions for longitudinal in silico trials studying the effect of breast cancer progression on imaging performance.

To facilitate the modeling of cancer progression within computational trial pipelines, we developed a 3D voxelized breast lesion model representing different stages of growth. Table 2.1 summarizes approaches that have been reported for simulating 3D voxelized breast lesions, including patient-derived and parameterized models. While the patient-derived models contain features from actual patient data and thus may look more realistic (*Dukov et al.*, 2019; *Bliznakova et al.*, 2019), they suffer from several shortcomings, including limited resolution of the tumor model, limited number of lesion shapes, and the need to establish institutional review board (IRB) approvals for obtaining patient data. On the other hand, the parameterized mathematical models enable the generation of a larger number of lesion shapes with variable resolution (*Bliznakova et al.*, 2003). Additionally, none of the models summarized in table 2.1 are based on biological phenomena. In comparison to the previous efforts, the work described in this chapter takes into account the biological factors that can affect the growth and morphology of the tumor such as interstitial tumor pressure, diffusion of metabolites as well as stiffness of the surrounding tissues.

Patient-Derived Models
Segmentation of 2D slices from DBT or breast computed tomography (bCT) volumes and stacked to create the final 3D tumor morphology(*Dukov et al.*, 2019; *Bliznakova et al.*, 2019)
Mathematical Models
Simple shapes (e.g., ellipsoids/spheres) (*Bliznakova et al.*, 2003)
Random walk model(*Hintsala et al.*, 2009)
Diffusion limited aggregation model (*Rashidnasab et al.*, 2013)
Gaussian sphere model with iterative fractal branching (*de Sisternes et al.*, 2015)

Table 2.1: Methods for breast lesion models from the literature.

Tumor growth consists of avascular and vascular phases. During the avascular phase, the tumor grows up to a few mm(*Chaplain*, 1996), depending on the diffusion of vital nutrients into the tumor from the surrounding tissue. Due to rapid cell division within a confined region, cells located toward the center experience very high interstitial pressure. Vasculature and the lymphatic system also play a vital role in the increase in the interstitial pressure in tumors. In normal tissues, most of the fluid that filters into the interstitial space, gets reabsorbed into the microvasculature system, while the rest is taken by the lymphatic system. In tumors, the lymphatic system is not so well defined and if the reabsorption of the fluids is not rapid enough, while the tumor cells are still proliferating, the fluid build up could add to the interstitial pressure(*Jain*, 1987). In the vascular phase, when blood vessels start to grow into the tumor, they add to the interstitial pressure as well. The interstitial pressure is extremely high at the core and reduces toward the tumor periphery. This gradient in interstitial pressure induces an outward convection of vital nutrients, depriving the core cells of oxygen (O_2) and giving rise to a necrotic core. The cells near the tumor periphery taking part in cell division are termed "active cells," while cells in the middle of the necrotic core and active cells are called "quiescent cells." In response to hypoxia, tumor cells begin the process of secreting chemicals known as tumor angiogenesis factors (TAFs), inducing new blood vessels to sprout from existing ones. The new vessels gradually penetrate the tumor, providing an adequate blood and nutrient supply required to maintain its growth. The vascular growth phase of breast cancer represents the moment when lesions become palpable (*Gavaghan et al.*, 2002). Breast cancer screening programs aim to detect cancer before lesions reach the vascular stage.

Previous computational and theoretical efforts have attempted to predict pattern formation in nature. Among them, the reaction-diffusion model developed by Turing is one of the most popular analytical frameworks for the explanation of spatial

biological pattern formation (*Turing*, 1952; *Kondo and Asal*, 1995). Turing, in his 1952 seminal paper, proposed that the temporal variation of the concentrations of two different diffusible morphogens, the activator and the inhibitor, can create patterns by reacting with each other. His model was used by Chaplain et al. (*Chaplain*, 1996) to simulate the avascular growth of cancerous tumors, noting that some biological chemicals could inhibit and promote tumor growth. However, this initial model did not consider any effect of surrounding interstitial tumor pressure that could affect the flow rates for the different metabolites and growth factors. Factoring the interstitial pressure into Turing's original model led to the advection-reaction-diffusion model. Advection involves the rate of change of metabolites and growth factors toward the tumor core due to gradual increases in interstitial tumor pressure from rapidly-dividing cells. This model has been used to simulate the growth of several types of tumors (*Chaplain*, 1996; *Lujan et al.*, 2019; *Yan et al.*, 2017; *Frieboes et al.*, 2010; *Sauer et al.*, 2020; *Tang et al.*, 2014), including aggressive glioblastomas (*Yan et al.*, 2017; *Frieboes et al.*, 2010). A similar approach has been used to simulate the growth of breast lesions for MRI studies (*Weis et al.*, 2013a). Although the work by Weis et al. explored the effect of the lesion's microenvironment on the diffusion of drugs and nutrients, it did not account for the growth of anisotropic lesions. This is a major drawback of previous efforts. In this article, we describe, for the first time, an approach for modeling the growth of anisotropic breast cancer lesions unique to their breast environments. We have also developed a method for adding spiculations to the lesions at various stages of growth. Finally, we show digital mammography (DM) images of growing lesions within anatomical breast digital models using the freely available, open-source VICTRE (Virtual Imaging Clinical Trials for Regulatory Evaluation) in silico imaging pipeline (*Badano et al.*, 2018; *VICTRE Github Repository*, 2018), depicting several stages of tumor growth.

2.3 Methods

2.3.1 Tumor dynamics

Growth dynamics, based on advection-reaction-diffusion equations of this model, were adapted from Tang et al. (*Tang et al.*, 2014). As shown in Fig. 1, the model begins with the calculations of interstitial tumor pressure as a combination of cell and vessel perfusion induced pressures. For simplicity, we have ignored the contribution of the lymphtic system to the tumor pressure. Additionally, the vessel perfusion induced pressure contributes to the interstitial tumor pressure only in the vascular phase. Since we are focussing on the avascular phase in this work, our model begins with the calculation of interstitial tumor pressure resulting from rapid cell division in a confined space. This pressure is calculated as a Gaussian-like function, with the highest pressure being exerted at locations closer to the tumor cell, as expected. In other words, the cell- induced pressure P experienced by a tumor cell located at X_0, due to N neighboring cells, located at X_i can be expressed as:

$$P_{X0} = \sum_{i=1}^{N} p_i \times \exp(\frac{-(l(X_0, X_i))^2}{2(\sigma_{Xi})^2}). \tag{2.1}$$

Here, $l(X_0, X_i)$ is the euclidean distance between two locations in the tumor, and p_i is a constant related to interstitial tumor pressure. Please note that in the original publication by Tang et al., p_i is expressed as a function of the tumor cell density, θ. However, in the actual computational implementation, p_i was defined as a constant. The value of p_i was determined empirically (*Tang et al.*, 2014):

$$\sigma_{Xi} = \sigma_0 \frac{\theta^2}{\theta^2 + 0.5^2} + 0.05, \tag{2.2}$$

where θ is the tumor cell density calculated as the ratio of the number of grid points in

the surroundings occupied by tumor cells to the total number of neighboring locations (26 in our implementation). The value of the constant σ_0 (0.15) was determined empirically (*Tang et al.*, 2014).

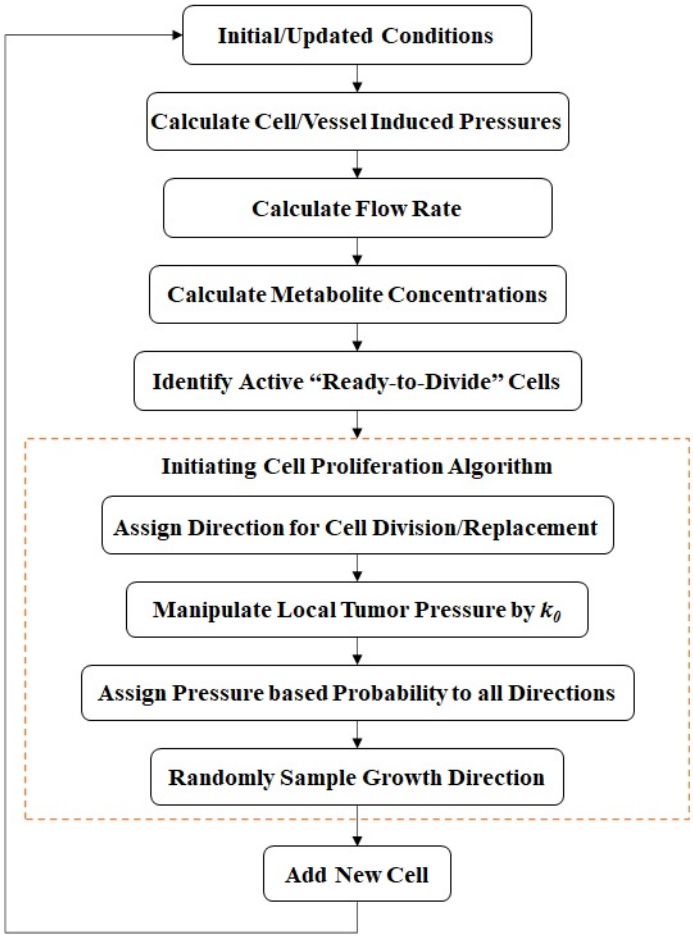

Figure 2.1: Algorithm for anisotropic tumor growth based on pressure fields.

This model focusses on O_2 and carbon dioxide (CO_2) as the main macromolecules that affect the growth of the tumor. Other nutrients such as glucose, amino acids, fatty acids, vitamins, and micronutrients also play an important role in the growth of tumors. However, modeling their transport and permeability across the cell's plasma membrane is a complex process (*Tang et al.*, 2014). So for simplicity, only the effect of oxygen O_2 is considered in this model. Although O_2 is the only nutrient considered,

it is crucial for aerobic metabolism in cells. Oxygen plays an important role in the tumor growth process by aiding cell metabolism, angiogenesis and metastasis. The gradients of pressure affecting the flow rate of the macromolecules such as O_2 and carbon dioxide (CO_2) and their final concentrations are calculated using advection-reaction-diffusion equations, such as:

$$\frac{\partial n}{\partial t} = D_n \nabla^2 n - \nabla.(u.n) + \rho_0 R_i P_w - \lambda_0 A_i, \tag{2.3}$$

where n (mol/m^3) represents O_2 concentration, D_n is the diffusion constant in m^2/s and u is the flow rate, ρ_0 is the rate of oxygen supply in mol/(m^{3}sec), R_i is the radius of a blood vessel and P_w is the pressure gradient through the vessel wall. A_i is the cell activity and λ_0 with units of mol/(m^{3}s). Please note that equation 2.3 is equivalent to the combination of equations 6, 7 and 8 in the original publication. [1] is an empirically-determined constant. The first and second terms on the right side of the equation represent diffusion and advection, respectively, while the third term is a source of O_2 and the fourth represents cell activity consuming O_2. The concentration of CO_2 also can be determined using similar equations, but with the cell activities acting as a source of CO_2. All parameter values used in the growth model including diffusion coefficients, supply and consumption rates of the various metabolites, and initial values of the nutrient and waste concentrations are summarized in Table 1 in the original publication by Tang et al.(*Tang et al.*, 2014). References have also been provided to justify some of these choices, while the others have been optimized to cover the transition of the tumor from its avascular to vascular phase with reasonable computational efficiency. Based on the metabolite concentrations, tumor cells are classified as active, quiescent or necrotic. Only certain active cells with energies greater than a threshold are allowed to divide. The algorithm is initiated with 5

[1] The units reported in the original publication by Tang et al. (*Tang et al.*, 2014) are not consistent.

active cells which are organized in a random anisotropic shape in adjacent voxels. As the cell enters the division algorithm, it is considered to be placed at the center of a cube with 26 neighboring locations for potential proliferation. So far this algorithm is based on the work by Tang et al. The major addition in this work is the cell proliferation informed by the stiffness of the various tissues in the local microenvironment of the tumor. In order to achieve this in situ growth, the pressures along certain directions were manipulated in proportion to the stiffness of the surrounding tissues, which was determined using their elastic moduli. A proliferation probability, inversely proportional to the tumor pressure, is assigned to each of the 26 locations. Finally, the location for cell division is randomly sampled, and a new cell is added.

The simulation time scale for tumor growth is recorded in cell life cycles (CLCs). One CLC represents approximately 25 iterations of the code, after which cells gain enough energy to divide based on O_2 and CO_2 concentrations.

2.3.2 In situ growth

We relied on the assumption that tumor morphology is to some degree correlated with the mechanics of the tumor's surrounding tissue types, and grew tumors inside volumes extracted from a breast model comprised of adipose, glandular and ligament tissues. Other anatomical structures included in the breast volume were ducts, arteries and veins. The hypothesis is that varying the elasticity of these different anatomical structures influences the shape of the growing lesion. This has been corroborated by previous reports (*Stein et al.*, 2007; *Helmlinger et al.*, 1997) which showed that tumors are very sensitive to their microenvironments and that their growth is inhibited when exposed to high mechanical stress. Earlier models depicting growth of breast lesions (*Weis et al.*, 2013b) and gliomas (*Garg and Miga*, 2008) have incorporated the effect of mechanical stress by coupling the stress factor to the cell diffusion coefficient through an exponential function. One of the major drawbacks

of the previous approach by Weis et al. (*Weis et al.*, 2013b), is that even after including the effect of tissue mechanics, the growth model generated fairly isotropic tumors with minor perturbations at the edges. The only anisotropic lesions shown in Weis' article were generated using morphology derived from patient data. Weis et al.'s model was developed to predict the number of tumor cells rather than their final morphology. In addition, Weis' model described 2D lesion growth and is not suitable for generating 3D voxelized lesion models required for conducting in silico trials.

In our work, we directly coupled the mechanical constraints exerted by the local tissue structures to the cell proliferation algorithm. Stiffer tissues do not allow tumor cells to deform or grow into them. Tumor cells, therefore, preferentially grow into more elastic regions of the breast. The algorithm is illustrated in Fig 2.1. We varied the value of k_0 proportionally to the elastic constants of the tissues surrounding the proliferating tumor cell. The local pressures are manipulated by k_0:

$$P^n{}_{X0} = k_0 \times P_{X0}. \tag{2.4}$$

Here, P_X is the total interstitial tumor pressure calculated at X using equations described in the original publication by Tang et al.(*Tang et al.*, 2014). Following the algorithm shown in Fig. 2.1, a cell proliferation probability was assigned to each of the neighboring 26 locations, such that locations that had more elastic tissues (and lower pressures) had higher probabilities. Finally, a location for cell division was randomly sampled, and a new cell added in that location.

The elastic modulus for adipose, glandular and ligament tissues (*Gefen and Dilmoney*, 2007) and corresponding k_0 values are shown in Table 2.2. One of the most frequently-detected types of cancer is ductal carcinoma in situ (DCIS) (*Sakorafas and Tsiotou*, 2000), which starts out from within the ducts (*Coleman*, 2019). If left

untreated, most cases develop into invasive breast cancer (IBC) (*Risom et al.*, 2021). DCIS originates from the epithelial cells in the ducts and sometimes grows along the ducts for a prolonged (up to several years) period of time, after which it invades the surrounding tissues (*Erbas et al.*, 2006). To simulate lesions representing DCIS, ductal fluid was assigned a k_0 value of 1. Since fat may not be as elastic as ductal fluid, we assigned a k_0 value of 10 to the voxels representing fat. So far we have found no evidence that tumors that originate in other tissues of the breast, penetrate and continue growing inside blood vessels. Angiosarcoma of the breast is a rare form of cancer that originates in the blood vessels. However, this only accounts for 1 % of the all breast tumors (*Arora et al.*, 2014) and thus we have ignored this type of cancer for our current study. So in this work, other structures included in the breast model, such as arteries, veins and skin were considered to be statistically impenetrable, with a k_0 value of 10^6.

Tissue Type	**Elastic Modulus [kPa]**	**Pressure multiplication factor (k_0)**
Fat	0.5-25	10
Glandular	7.5-66	45
Ligaments	80000-400000	10^6

Table 2.2: Pressure multiplicative factor based on Elastic Modulus for different tissue types.

2.3.3 Local anatomy modeling

We used the breast models developed by Graff et al.(*Graff*, 2016) to simulate lesion growth in situ. As compared to previous approaches described in literature (*Bakic et al.*, 2001, 2002, 2003; *Bliznakova*, 2016; *Bliznakova et al.*, 2003), the breast model developed by Graff et al.(*Graff*, 2016) includes anatomical features such as vasculature, ductal network and a realistic breast shape in addition to the adipose and glandular tissues. These features make the breast model by Graff et al. an attractive option for our application.

In order to create anisotropic pressure maps based on the local anatomy, we extracted 1cm x 1cm x 1cm volumes from fatty breast models (*Graff*, 2016) generated with the VICTRE toolbox (*Badano et al.*, 2018; *Sharma et al.*, 2019; *VICTRE Github Repository*, 2018). Locations for volume extraction were chosen randomly from a list of potential candidates generated for each breast model. Volumes for lesion growth were selected after confirming that they lay within the breast boundary and had no overlap with air, muscle, nipple or skin.

The extracted anatomies were 3D voxelized volumes, with each voxel representing a different tissue type. Fig. 2.2a shows a central slice from one of the extracted volumes. Adipose and glandular tissues are represented by black and blue, while the white voxels indicate ligaments. As we can see from the figure, the ligaments are interspersed with many black (fat) voxels or "holes." While the presence of such minute holes in the breast model may not affect the appearance of the much larger DM or DBT images, they can affect the shape of tumors growing in their vicinity. Since these holes are represented as voxels of fat, a significant number of tumor cells can penetrate the ligaments through these holes resulting in isotropic shapes and leading to unrealistic morphology.

To address this issue, we developed an algorithm (see Fig. 2.2 b to control the penetrability of the ligaments. First, the ligaments were segmented and a MATLAB-based smoothing function (*MATLAB Documentation*, 2006) was used to fill the holes and thicken the ligaments. The thicker ligaments then were reinserted into the original volume by voxel substitution. We used a Gaussian smoothing function. By varying the standard deviation of the Gaussian function, we could control the number of holes in the ligaments, and consequently, their effect on tumor shape. An example of the process for reducing the number of holes in the ligaments is shown in Fig. 2.2 c.

Once the processing of the extracted volume was completed, we translated it into a 3D map of k_0 values corresponding to the voxel tissue types. This map then was

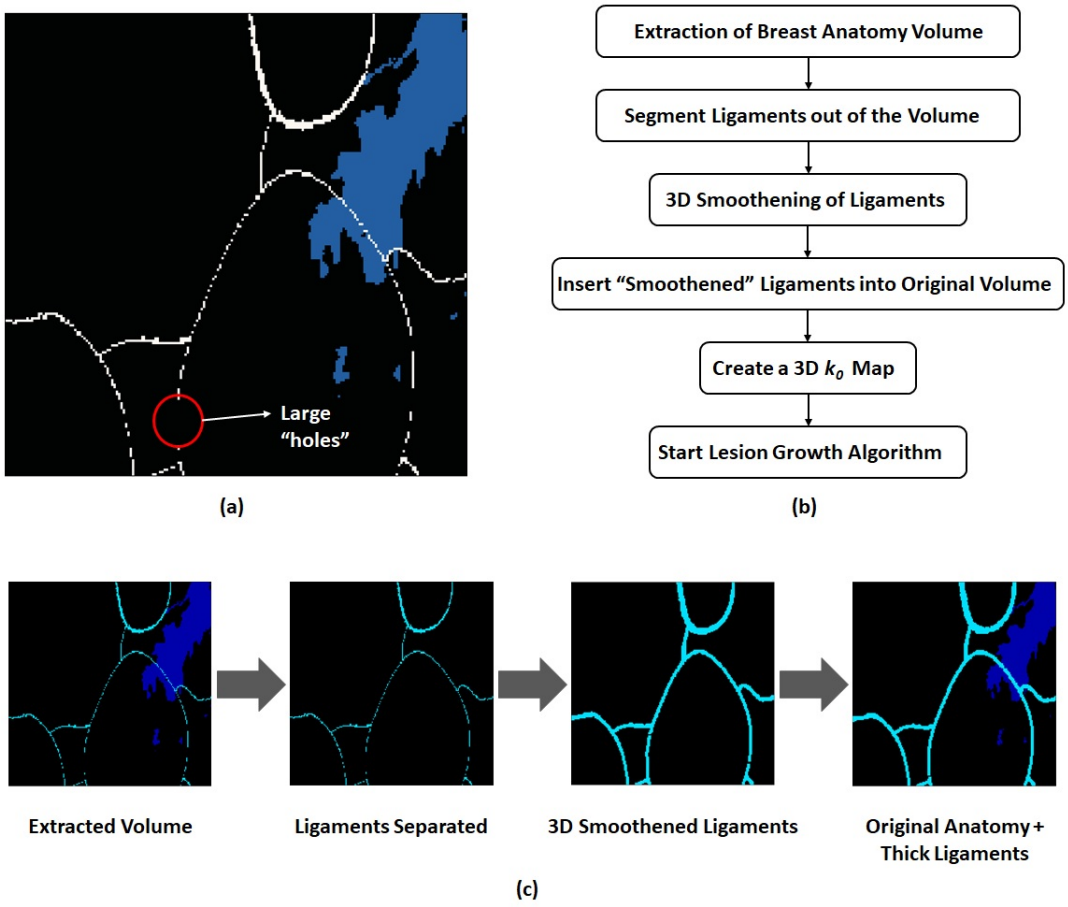

Figure 2.2: Postprocessing of extracted anatomy volumes to reduce the number of holes. (a) A central slice from a 1cm x 1cm x 1cm anatomy volume extracted from a fatty breast model. The black regions are fat, blue is glandular tissues and white are ligaments. An example of large holes in the ligaments is encircled. (b) Flowchart for postprocessing of the extracted volumes to reduce holes and (c) Process for reducing the number of holes in the ligaments. Fat and glandular tissues are represented by black and dark blue. Ligaments are indicated in cyan.

used to manipulate the local tumor pressures during the cell proliferation process, as shown in Fig. 2.1.

2.3.4 Addition of spiculations

One of the most common indicators of breast cancer in DM or DBT images is the presence of a mass with thin, needle-like lines called spicules, radiating from its

center (*Seto and Mardiyana*, 2019). Spicules are formed as a result of direct invasion of the tumor or through a desmoplastic reaction with its surrounding tissues (*Griff and Dershaw*, 2002). To date, no report has addressed the modeling of spicule growth based on biological processes.

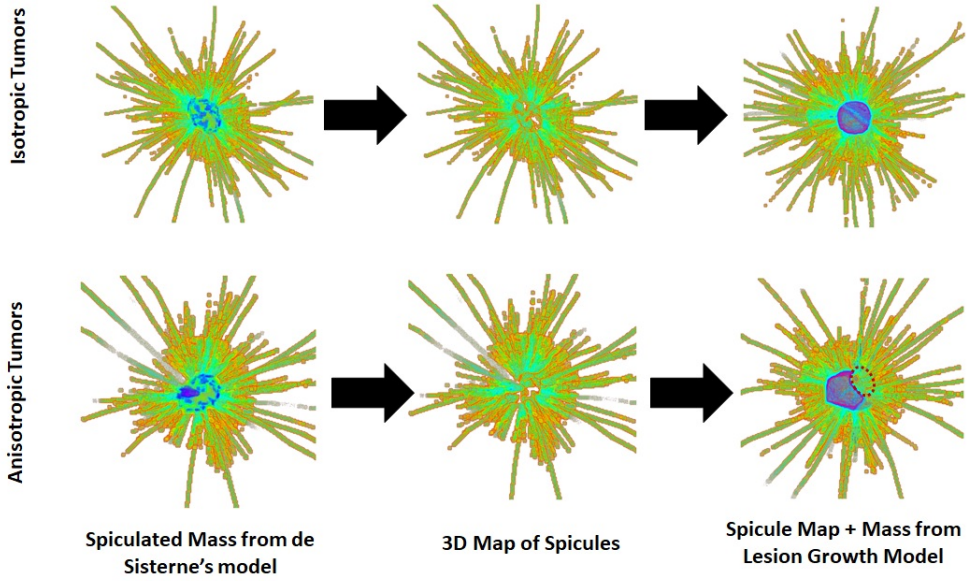

Figure 2.3: Process of generating spiculated lesions for isotropic and anisotropic central masses. The spicules are indicated in yellow while the central mass is blue.

We modeled the growth of spicules following a technique by Elangovan et al.(*Elangovan et al.*, 2016a). In their work, the authors discussed creating spiculated lesions with a central mass generated using a diffusion-limited algorithm and attaching a set of spicules to the mass surface. They generated spicules manually by scrolling through patient DBT slices with spiculated masses, marking the points where they first appeared, and using 3D interpolation techniques to produce a 3D spicule skeleton. This method requires access to patient data and appropriate informed consent approvals. We describe here a similar approach that, instead of relying on patient data, used our implementation of de Sisterne's model (*de Sisternes et al.*, 2015) to create a 3D map of spicules, as shown in Fig. 2.3. Using de Sisterne's model, we generated a

3D voxelized spiculated mass with the central mass and spicules represented by voxel values 1 and 2, respectively. As the central mass (represented in blue in Fig. 2.3) and spicules (represented in yellow in Fig. 2.3) are differentiated by their voxel values, we could easily segment and create a 3D map of the spicules. With de Sisterne's model for spicules, we could control the number of spicules, their length and curvature. Finally, we attached the segmented spicules of varying lengths to the mass corresponding to different time points from our lesion growth model. This method works well for isotropic and most anisotropic masses. In some cases in which the central mass is highly anisotropic, some gaps (encircled in dotted red in Fig. 2.3) can be seen.

2.3.5 Imaging

Lesion models were saved at various stages of growth and inserted in the same fatty breast models using voxel replacement. The DM projections were generated using the GPU-accelerated Monte Carlo (MC-GPU) x-ray transport simulation code (*Badal et al.*, 2020b), developed as part of the VICTRE pipeline (*Badano et al.*, 2018; *Sharma et al.*, 2019; *VICTRE Github Repository*, 2018). The MC-GPU codes replicated the technical specifications and imaging characteristics of the Siemens Mammomat Inspiration system, currently in clinical use for DM and DBT. The MC-GPU codes were used to model a direct 200 μm amorphous selenium based detector with 2816 $\times$ 3584, 85 μm pixels. The radiographic spectrum suitable for the fatty breast models was simulated using a tungsten anode with a peak tube voltage of 30 kVp, filtered with 50 μm rhodium and 1 mm beryllium. To generate the DM images for each breast model containing the lesions, 3.7x10^{1}1 histories were used, which took 38 minutes on a system with 2 GeForce GTX 1080 NVI-DIA GPUs and 32 GB of memory. The lesions were realized as denser (up to x1.5) glandular tissue for visualization purposes. All processing of raw images generated by the MC-GPU codes

was performed using ImageJ, by first converting them to 16-bit images, followed by enhancing image contrast.

2.4 Results

2.4.1 Modeling local anatomy

Fig. 2.4 illustrates the effect of preprocessing of ligament holes. The first column on the left shows slices of volumes extracted from a fatty breast model, postprocessed with a Gaussian filter-based convolution kernel of varying standard deviations. Adipose and glandular tissues are in black, while ligaments are in green. The lesion itself is in red. We noted that, as expected, the number of holes in the ligaments decreased with an increase in the standard deviation of the smoothing function. This enabled tumor cells (in red) to penetrate into the fatty regions (in black, see Fig. 2.4, 2.5, 2.6) of the breast, lacking the expected growth inhibition due to the presence of ligaments, and resulting in isotropic growth (see row 1 of Fig. 2.4). By increasing the standard deviation of the Gaussian filter-based convolution kernel, we were able to thicken the ligaments and obtain a range of breast lesion morphologies at different breast locations, depicted in column 2 of Fig. 2.4. The third column shows simulated DMs containing the same lesions. Additional figures showing these effects at different locations in the breast are included in the supplementary material.

Figs. 2.5 and 2.6 show similar effects of postprocessing of the extracted local anatomy volumes, discussed in Section 3.1, at other locations in the breast model. In short, a higher standard deviation would result in more holes in the ligaments being filled, thus generating more anisotropic shapes controlled by the ligaments. Some of the differences in the lesion morphology may be quite subtle in the DM ROIs (rows 2 and 3 of Figs. 2.5 and 2.6), owing to the presence of overlapping tissues.

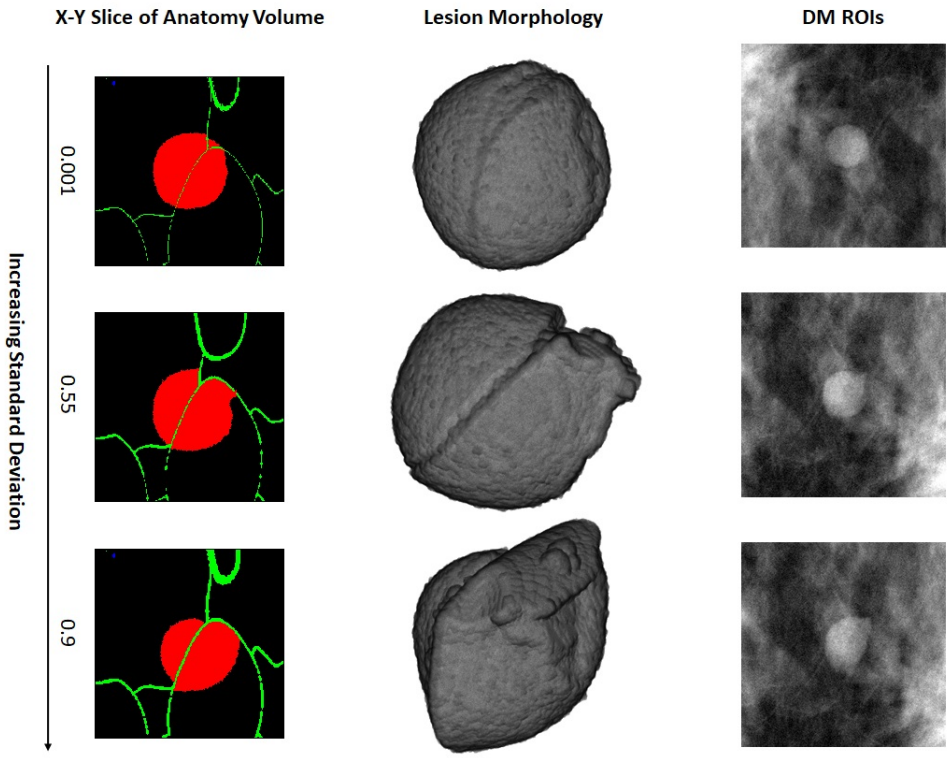

Figure 2.4: Effect of postprocessing of extracted anatomy volumes on final lesion morphology. Column 1 shows slices of a volume extracted from a fatty breast model, postprocessed with a Gaussian filter based convolution kernel of varying standard deviation. The number of holes in the ligaments decrease with an increase in standard deviation. Column 2 shows the 3D voxelized lesion alone while column 3 shows ROIs from simulated DMs containing the same lesion in column 2.

2.4.2 Effect of local anatomy on morphology

Fig. 2.7 (rows 1, 2 and 3) shows different lesion morphologies realized using this model. Column 1 shows the lesion shapes while Column 2 includes some local anatomy information. The green and blue voxels represent ligaments and ducts, while the lesion is indicated in red. The first two rows show the effect of ligaments on lesion morphology. Ligaments in the second row had fewer holes compared to those in the first row, resulting in much more restricted lesion growth. The third row represents the growth of DCIS, in which the tumors originate within ducts, grow along them, and then overflow into the surrounding fatty and glandular regions. The third

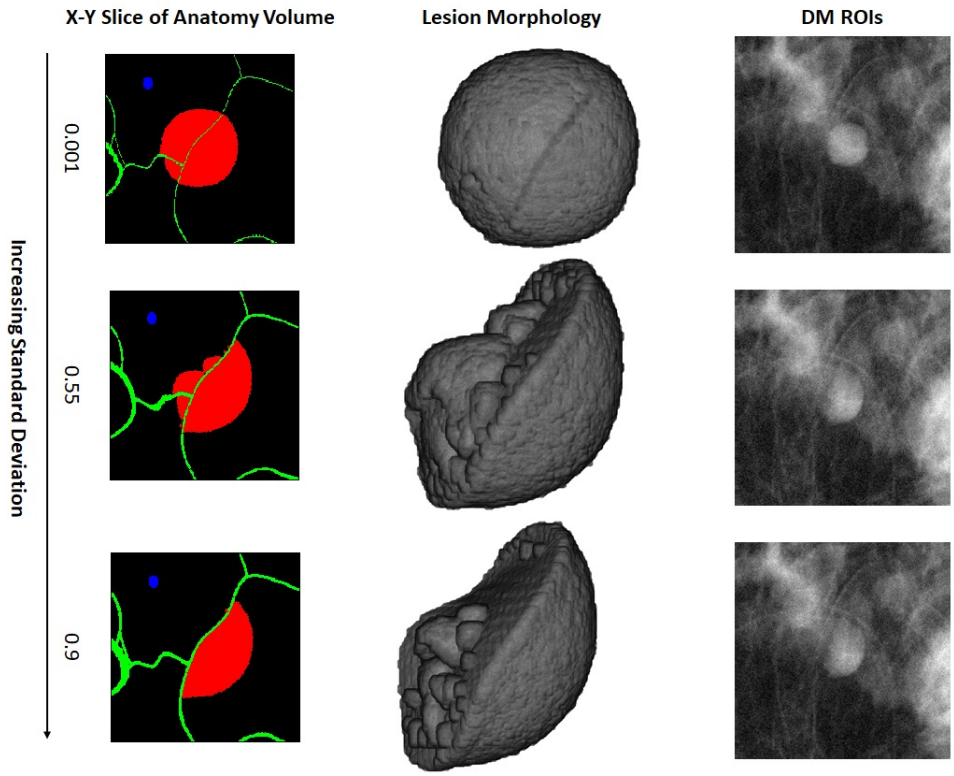

Figure 2.5: Effects of postprocessing of the extracted local anatomy volumes on the final lesion morphology. Column 1 shows x-y slices of a volume extracted from location 2 from a fatty breast phantoms, postprocssed with a Gaussian filter based convolution kernel of varying standard deviation. Adipose and glandular tissues are black, ducts are blue, while ligaments are indicated in green. The number of holes in the ligaments decrease with an increase in standard deviation. Column 2 shows the 3D voxelized lesion alone while column 3 shows ROIs from simulated DMs containing the same lesion in column 2.

column shows ROIs from simulated DMs generated using the VICTRE pipeline. The lesions,circled in red, are quite difficult to see, as they were imaged with attenuation coefficients similar to those of normal glandular tissues with a slightly (1.3 times) higher density.

Fig. 2.7 (rows 4, 5 and 6) shows a variety of models that result in isotropic growth. Column 1 shows the lesion alone. Columns 2 and 3 include information about the local anatomy where they were grown. Column 2 shows a central x-y slice of the volume containing the tumor, while Column 3 depicts the entire volume. As we can

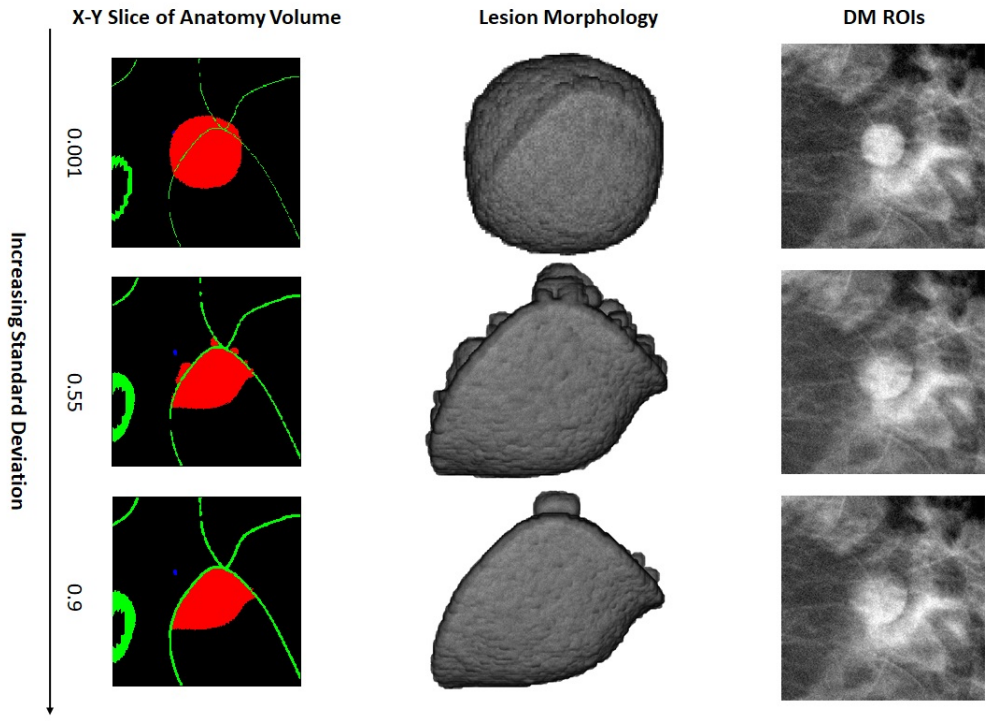

Figure 2.6: Effects of postprocessing of the extracted local anatomy volumes on the final lesion morphology. Column 1 shows x-y slices of a volume extracted from a fatty breast phantom, postprocssed with a Gaussian filter-based convolution kernel of varying standard deviation. Adipose and glandular tissues are black, ducts are blue, while ligaments are indicated in green. Lesions are in red. The number of holes in the ligaments decrease with an increase in standard deviation. Column 2 shows the 3D voxelized lesion alone, while Column 3 shows ROIs from simulated DMs containing the same lesion as that in Column 2.

see in the first two rows, the lesion does not interact with the ligaments, and mostly grows isotropically. The lesion in the second row does encounter some glandular tissue; hence, its shape is more irregular in comparison to the growth in the first row. The third row represents the case in which the tumor encounters a ligament with a large number of holes. These holes allow the cells to migrate to the other side of the ligaments, resulting in isotropic growth. Fig. 2.8 shows the generation of anisotropic and isotropic masses, and the subsequent attachment of a 3D spicule map. The third column shows projections of the spiculated masses alone, demonstrating the fine appearance of the spicules in the projections. The last column shows ROIs

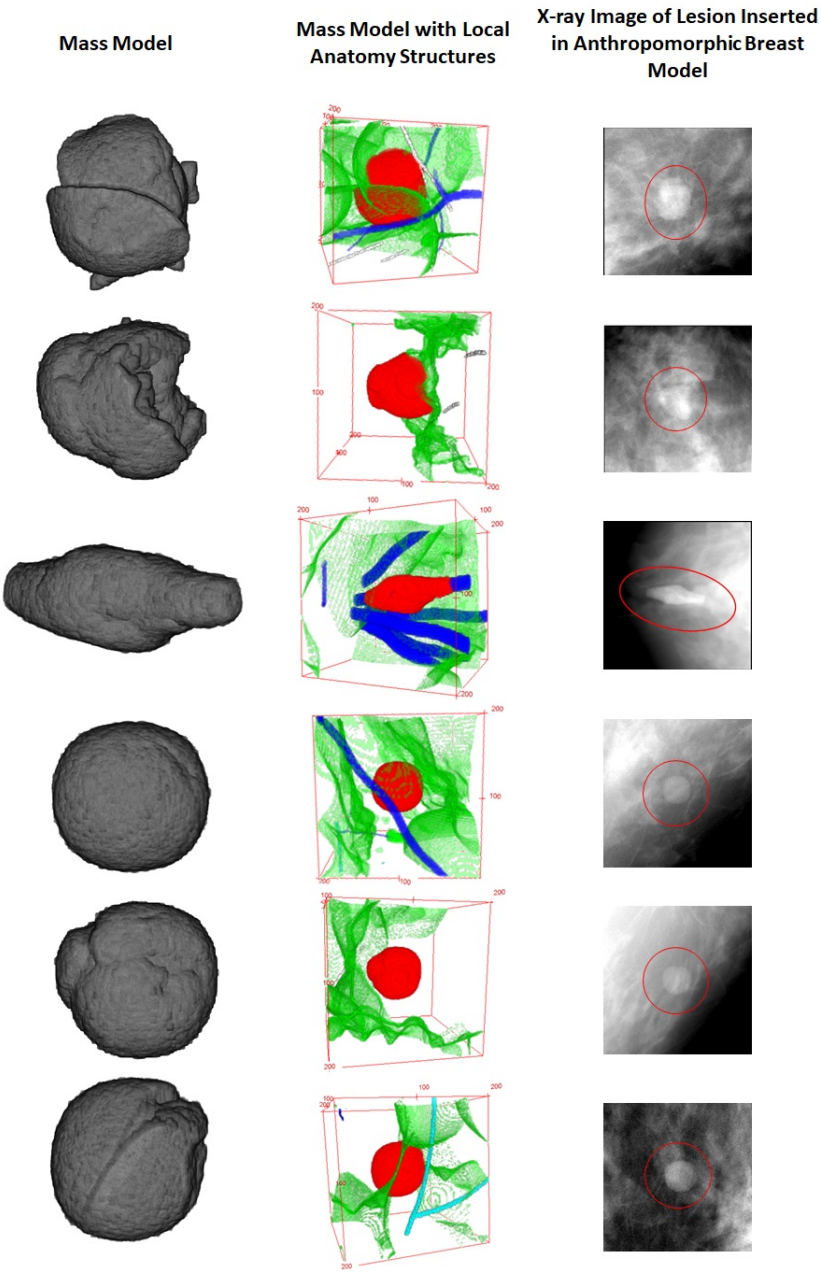

Figure 2.7: Lesions and their appearance in renderings and in the DM images. Lesions (column 1) grown in situ. The second column includes local anatomy information. The third column are DM ROIs containing the lesions in the first column. All lesions were imaged as glandular tissues, but with higher density. For better visibility, the lesions in all rows were imaged with 1.3 times higher density, except for the one in the third row, which was imaged with 1.8 times higher density.

of the spiculated masses imaged along with their respective breast environments. To improve contrast and visibility of the spicules in the ROIs, the lesions were imaged as calcium oxalate masses. In the x-ray projections, locations with a larger density of lesion cells per unit volume appear brighter. The lesion core is densely packed with cells, while the spicules are thin hair like structures with relatively low density of cells. Hence the core appears brightest as compared to the periphery and the spicules.

All ROIs in Figs. 2.4 and 2.7 contain the central masses shown in Column 2, with 3D spicule maps attached to them. However, since these lesions were imaged as dense glandular tissues, the fine spicules no longer were visible, due to overlapping tissues.

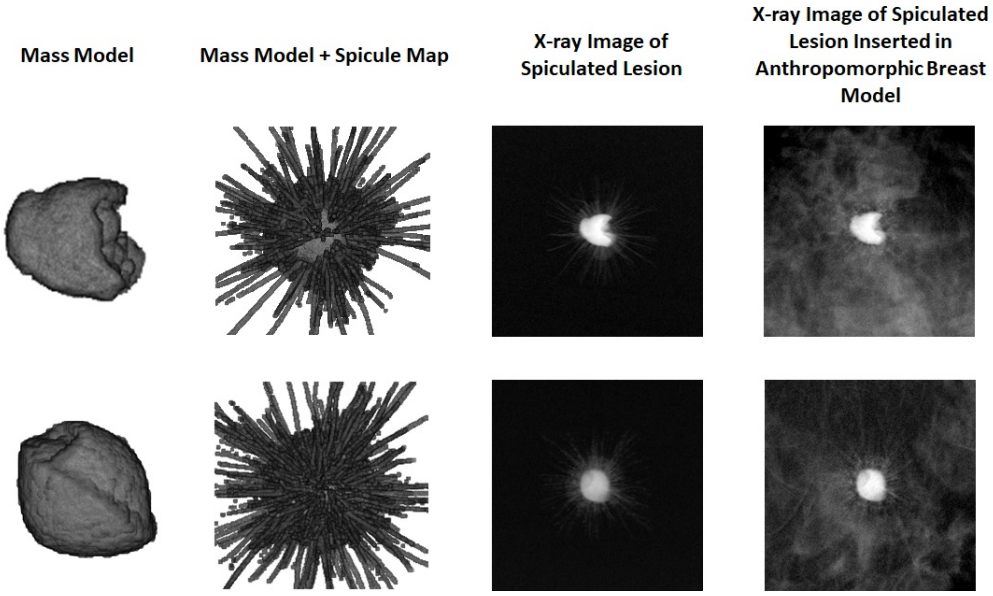

Figure 2.8: Examples of spiculated masses. Column 1 shows the central mass alone, while the second column shows the mass overlapped with spicules. The third and fourth columns show projections of the lesions alone and with appropriate tissue background respectively.

Fig. 2.9 illustrates the ROIs from DM images of breast models with lesions at different locations and stages of growth. To improve the contrast of the lesions, their attenuation was set to be similar to that of glandular tissue, but with 1.5 times-higher density, so that the smallest lesion, at 10 CLCs, could be distinguished from

the normal anatomy.

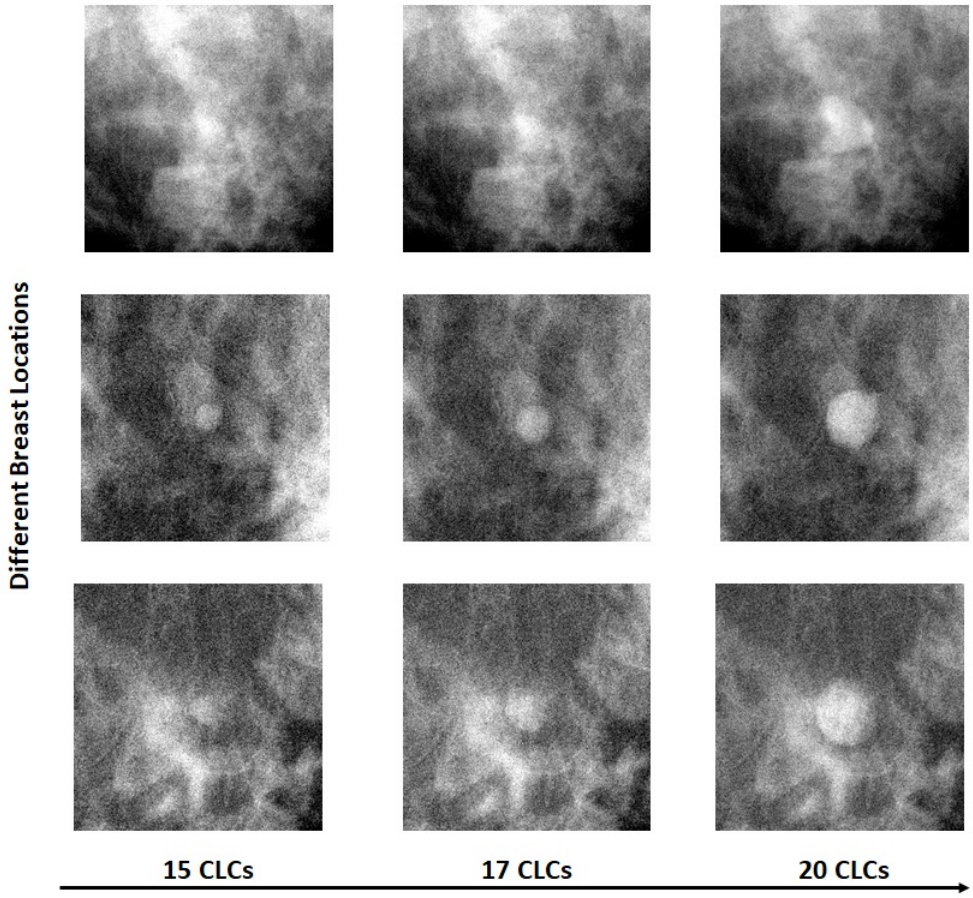

Figure 2.9: Lesion growth from an imaging point of view. 250 x 250 pixel ROIs selected from simulated DM images generated using the VICTRE pipeline and breast model containing a disc-like lesion at different locations in the breast model and at different stages of growth (CLCs).

2.4.3 Comparison with patient images

As an initial step toward validating our model, we compared our simulated DMs of fatty breast models, containing lesions grown at different locations, with real mammograms containing masses with similar shapes. Fig. 2.10 shows real mammograms, in the left column, containing malignant tumors with ill-defined margins. Column b shows simulated DMs generated using the VICTRE pipeline with a similar tumor. The inset ROIs show a magnified version of the same mass, but with higher contrast

to facilitate better visibility. Column C shows more examples of ROIs from real as well as simulated DMs containing microlobulated and ill-defined masses. After comparing the masses in the left and right columns, we noted that qualitatively our model could be said to generate masses that are similar to those in real cases.

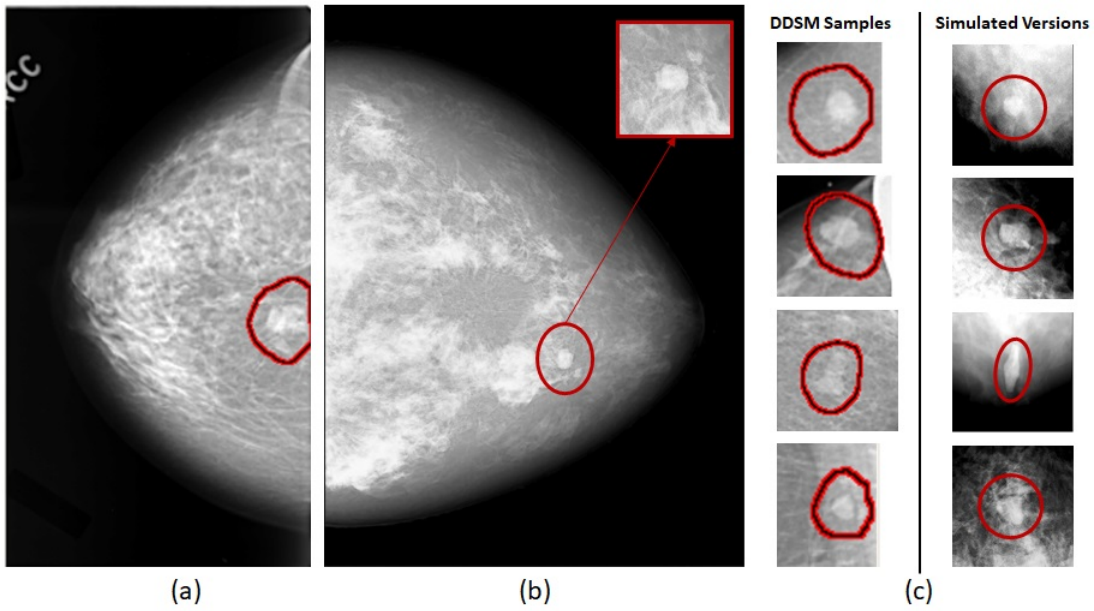

Figure 2.10: Comparison with patient images. (a) Real mammograms from the DDSM dataset with a malignant tumor with ill defined margins, (b) Simulated DM of a fatty breast model with similar lesions tumor growing inside. The inset 250 X 250 pixel ROI shows a magnified version of the same mass, but with better contrast, (c) Pairs of ROIs from real as well as simulated DMs containing malignant tumors with ill-defined and microlobulated margins.

2.5 Discussion

In this chapter, we presented a novel technique for coupling tumor growth dynamics with tissue mechanics, aimed at generating anisotropic and realistic breast lesions. Unlike previous approaches that realized lesions as arbitrary shapes, we modeled the growth of lesions informed by concentrations of neighboring metabolites and the mechanical properties of the local microenvironment. This allowed for the creation of

a range of lesion morphologies unique to their surrounding anatomical structures. While this was a useful step toward simulating biologically-relevant lesion growth, our study had some limitations.

Although it has been shown that this model can be used to generate a range of lesion morphologies, there are several cases in which the lesion looked like an almost perfect sphere in the simulated DMs, as shown in the third column of Fig. 2.7 (rows 4, 5 and 6). Malignant tumors rarely look as isotropic in the DMs. One way to address this issue would be to add texture to the fatty and glandular tissues, which currently appear to be unrealistically uniform throughout the breast models. This would result in more nonuniformities in the morphology grown in textured environments.

Another shortcoming of this model is the appearance of spicules in the DM ROIs. We added spiculations to the masses by overlapping the 3D masses with spicule maps generated using de Sisterne's algorithm(*de Sisternes et al.*, 2015). Currently our model does not account for the growth of spicules. Additionally, the spicules are not visible in DM ROIs when imaged as denser glandular tissues, which is not the case in real DMs.

The lesion models discussed in this article were generated using breast anatomy volumes extracted only from fatty breast models. We plan to test the same model for generation of masses using volumes extracted from other breast types, including dense, scattered glandularity and heterogeneously dense models. The variation in the fat and glandular content in the other three breast types could result in increased variability of lesion morphology.

The growth dynamics that informed tumor growth in this work also tracked the number of quiescent and necrotic cells. We did not investigate how the presence of necrosis could affect the appearance of lesions in the DMs. In silico modeling of other imaging technologies such as contrast enhanced imaging can also benefit from the simulation of necrotic cells facilitated through our model. Additionally,

the growth dynamics also modeled the effects of angiogenesis with new blood vessels penetrating the lesion. However, since we grew the lesions in situ, these new blood vessels that facilitated angiogenesis must have originated from those already present in the extracted breast volume. This adds another level of complexity that was not explored in this chapter.

Currently, this study does not include a rigorous validation of the growth simulation. To pursue an investigation to determine how realistic the simulation is, we would have to observe the growth of breast lesions within the human body and compare it to our results. This is impossible to do, because once a breast lesion is detected, it will most likely be treated and not allowed to develop further. Another approach could be to compare our simulations to growth of xenograft mouse models of breast cancer(*Li et al.*, 2015). While this is an avenue that we would like to pursue in the future, currently it is beyond the scope of this chapter. While it is important to validate the growth, for our applications, it maybe sufficient to demonstrate that our model can be used to generate realistic mammograms. To do so, we included a subjective comparison of our lesion models with patient data by observing simulated DM with mammograms from the DDSM dataset. In the future, we plan to pursue a more robust validation of our model via a reader study. One possible design for such a study is a two-AFC reader study comparing DM ROIs containing lesions generated using this model with those containing lesions from a previously-validated model(*de Sisternes et al.*, 2015). If the readers are unable to distinguish between the two, it would follow that the two models generate similar lesion morphology. However, since the comparison would not involve real cases, we would not be able to make claims about realism. DM images of breast models containing our lesion model and those from de Sisterne's model (*de Sisternes et al.*, 2015) could be generated. All models in the in silico VICTRE framework (*Badano et al.*, 2018; *Sharma et al.*, 2019) required for generating the DM images would be the same, except for the lesion models. Readers

then could evaluate a side-by-side ROI pair from DM images containing the lesion, in order to identify differences.

2.6 Conclusions

We have presented a 3D computational model for simulating the growth of breast cancer lesions. Unique features of this model are the correlations between tumor morphology and the mechanical properties of breast tissues. With this model, we generated masses of various shapes unique to the local anatomical structures in which they grew. Using the VICTRE pipeline, we generated DM images of fatty breast models containing the lesions at different locations and stages of growth.

The lesion model described here could facilitate longitudinal research studies (*Langendijk et al.*, 2001; *Osoba et al.*, 2000; *Steele et al.*, 2000) investigating the progression of cancer. Our interest is in using the growth model as part of an effort to build an in silico version of the National Cancer Institute-funded Tomosynthesis Mammographic Imaging Screening Trial (TMIST) (*Pisano*, 2018). The primary end point of the trial is to investigate whether DBT can reduce the incidence of advanced breast cancer. Our model would be used to grow lesions at different stages into breast phantoms of varying densities. The primary outcome would be the difference in the area under the curve (AUC) of receiver operating characteristic (ROC) curves for the DM and DBT imaging modalities at different stages of growth possibly leading to a differential between the technologies in the detection of earlier, smaller lesions. This would enable the scientific community to gain insight into whether there are advantages of replacing DM with DBT for detecting breast cancers at earlier stages. Additionally, a similar methodology could be applied to studying lesion growth in other parts of the human body, including the brain and the liver. All codes used in this work (*VICTRE Github Repository*, 2018) along with a few extracted anatomy volumes for reproducing results shown in this article have been made freely available (*MATLAB Codes*

Repository, 2022).

CHAPTER III

Computational Models of Direct and Indirect X-Ray Breast Imaging Systems for in Silico Trials.

3.1 Abstract

In silico trials have garnered widespread popularity as fast and cost-effective alternatives to their clinical counterparts, for evaluating new concepts or improvements in imaging technology. To facilitate in silico studies that investigate modalities like digital mammography (DM) and breast tomosynthesis (DBT), it is important to develop models replicating the variety in imaging performance of the DM and DBT systems, observed across manufacturers.

We recently reported on an in silico version of the SIEMENS Mammomat Inspiration DM and DBT system using an open source GPU-accelerated Monte Carlo x-ray imaging simulation code, MC-GPU. The MC-GPU code implements a realistic x-ray source model with the tomosynthesis acquisition geometry and a detector model for the direct-conversion amorphous Selenium (a-Se) detector. We build on the previous version of the MC-GPU codes to mimic the imaging performances of two other FDA-approved DM/ DBT systems, such as Hologic Selenia Dimensions (HSD) and the General Electric Senographe Pristina (GSP) systems. Although the HSD system also uses a direct-conversion detector, it suffers from resolution loss due

to signal crosstalk. Similarly, spread of optical photons is typical in the thallium-doped cesium iodide (CsI:Tl) based indirect detector, used in the GSP system. In this work, we developed a hybrid technique to model the optical spread and signal crosstalk in these systems. MC simulations are used to track each x-ray photon till its first interaction within the x-ray detector. On the other hand, the signal spread in the x-ray detectors is modeled using previously developed analytical equations. This approach allows us to preserve the modeling accuracy offered by MC methods in the patient body, while speeding up secondary carrier transport using analytical equations in the detector. The analytical optical spread model for the indirect detector includes the depth-dependent spread and collection of optical photons and relies on a pre-computed set of point response functions that describe the optical spread as a function of depth. To understand the capabilities of the computational x-ray detector models, we compared image quality metrics typically used in clinical practice, simulated with our models against measured data. Specifically, we tested the resolution and noise properties of the models using modulation transfer function (MTF), normalized noise power spectrum (NNPS) and detective quantum efficiency (DQE).

We found that the simulated image quality metrics such as MTF, NNPS and DQE were in reasonable agreement with experimental data. To demonstrate the imaging performance of the three DM/DBT systems, we integrated the detector models with the VICTRE pipeline and simulated DM images of a fatty breast model containing a spiculated mass and a calcium oxalate cluster. In general, we found that the images generated using the indirect model appeared more blurred with a different noise texture, as compared to the systems with direct detectors.

We have presented computational models of three commercially available FDA-approved DM/DBT systems, which implement both direct and indirect detector technology. The updated versions of the MC-GPU codes that can be used to replicate three systems are available in open source format through GitHub.

3.2 Introduction

Two dimensional (2D) digital mammography (DM) is currently considered to be the gold standard for breast cancer screening programs. Since its introduction nearly 30 years ago, it has proven to be very effective in detecting breast cancer, achieving sensitivities up to 90.5% to 92.5% in certain populations (*Jacobsen et al.*, 2015). However, mammography is also extremely sensitive to breast density. While sensitivity rates for women with extremely fatty breasts could be as high as 87%, it drops to 63% for women with dense breasts (*Carney et al.*, 2003). This is mainly due to the large amounts of overlapping fibroglandular tissues in dense breasts that can mimic the presence of a cancerous lesion or can hide underlying masses in mammograms, a major shortcoming of this technology. Digital breast tomosynthesis (DBT), a limited angle tomographic technique, has been introduced to overcome these shortcomings by generating 3D information of the breast. However, optimizing image quality for DBT involves trade-offs between multiple interrelated parameters. For instance, a wide angular range can provide better separation of overlapping tissues, but reduces in-plane resolution and increases scan time, which is prone to patient motion. Usually long, time-consuming and expensive experiments are conducted for these studies. A cost effective and faster alternative is the use of sophisticated computational methods.

Currently there are several systems available in the market that offer both DM and DBT capabilities, of which the SIEMENS Inspiration Mammomat (SIM), HOLOGIC Selenia Dimensions (HSD), and General Electric (GE) Senographe Pristina (GSP) and Fuji Film systems have received FDA approvals. These systems differ from one another in terms of detector technology, system geometry parameters, x-ray beam quality, number of projection views and reconstruction algorithms. Table 3.1 shows characteristics of the SIM, HSD and GSP systems, modeled as part of this chapter. All systems apart from GSP are based on direct a-Se based x-ray detectors.

Different approaches have been used in the past for modeling x-ray detectors.

Device	SIM	GSP	HSD
Pixel Pitch (μm)	85	100	70 (binned for DBT)
Detector	a-Se	CsI	a-Se
Conversion layer thickness (μm)	200	250	200
DBT Projections	25	9	15
Angular Range	50°	25°	15°
Anode/Filter	W/Rh	Mo/Rh	W/(Rh or Al)
Filter thickness (mm)	0.05	0.025	0.05 (Rh) or 0.5 (Al)
SSD (cm)	65.5	66	70
Source to COR (cm)	65.5	62	70

Table 3.1: Description of three commercially available and FDA-approved DBT systems (*Mackenzie et al.*, 2017; *Sechopoulos*, 2013).

Monte Carlo (MC) simulations, derived from first principles, are the most accurate as they calculate interactions of every x-ray particle with each material layer within the detector. Previous MC simulations by Fang et al. (*Fang et al.*, 2012) also include detailed 3D spatial and temporal transport of charge carriers. Such MC packages have been developed for both direct a-Se (*Adnani et al.*, 2021; *Fang et al.*, 2012) and indirect CsI based detectors (*Badano and Sempau*, 2006; *Sharma and Badano*, 2013; *Sharma et al.*, 2012), however, they demand high processing power and result in long computational times. So they are not ideal candidates for use as part of in silico trials which often require thousands of patient models to be imaged. Analytical models are another way of simulating imager performance which are faster and do not require as much processing power. These models study the propagation of the signal and noise through x-ray detectors as series of blurring and gain stages. Some analytical models derive the detector statistics and image quality metrics in the spatial domain (*Freed et al.*, 2010; *Badano et al.*, 2011), while others harness the powers of Fourier space (*Sengupta et al.*, 2019; *Kim et al.*, 2008; *Zhao and Rowlands*, 1995) (see appendix chapter on cascaded modeling). The latter is called cascaded systems modeling, and is as a relatively simple way of predicting imaging performance of x-ray detectors. These models, however, can not be directly used for generating

mammograms and tomosynthesis images and need to be combined with ray tracing and scatter generation algorithms. Moreover, these models often employ arbitrary fitting functions, which are not derived from physics, to achieve a reasonable match with measured data. Post-processing schemes are another approach for modeling performances of different detectors. Mackenzie et al. described a method for adjusting real images, using measured data, by altering their sharpness, noise and contrast-to-noise ratio to represent that of the target systems. Although this is a fast and convenient method for modeling DM/DBT imaging performance, it is mainly an algorithm for manipulating images without modeling any detector physics. In this chapter, we use a hybrid technique for modeling the detector physics. Following the approach described by Badal et al. (*Badal et al.*, 2020a), based on MC x-ray simulations, each x-ray photon is tracked till its first interaction within the x-ray detector. Within the detector, we simplified the interactions a lot. We did not model Compton scattering and only k_α fluorescence emission is considered and tracked within the detector. We also did not model the transport of the secondary carriers (either electron-hole pairs or optical photons). For the direct-conversion detector, we assume that there is negligible charge sharing between pixels due to presence of strong electric fields. On the other hand, we model the optical spread in indirect detectors using analytical equations developed and validated by Freed et al. (*Freed et al.*, 2010). This approach allows us to preserve the modeling accuracy offered by MC methods in the patient body, while speeding up secondary carrier transport using analytical equations in the detector.

To understand the capabilities of the computational models, we compared image quality metrics typically used in clinical practice, simulated with our models against measured data. Specifically, we tested the resolution and noise properties of the models using modulation transfer function (MTF), normalized noise power spectrum (NNPS) and detective quantum efficiency (DQE). For GSP system, we compared our

simulated curves against data published in literature (*Oduko and Mackenzie.*, 2019). For the HSD and SIM systems (*Andrey et al.*, 2018; *Konstantinidis*, 2011), we used the MTF, NNPS and DQE data measured at our FDA labs.

3.3 Methods

Direct detectors

Currently, a-Se based direct-conversion detectors are the imaging technology of choice for most FDA approved DM/DBT systems, as noted in Table 3.1. These detectors directly convert the incident x-ray photons to electric charge pulses. The photo-electric effect is the main interaction that occurs between the incident x-ray photons and Se atoms (*Que and Rowlands*, 1995a), which generates a primary photo-electron. As this highly energetic photo-electron travels through the Se layer, it creates several secondary electron-hole pairs by ionizing several Se atoms. These electrons and holes are directed towards either the top or the bottom electrode by the strong electric field applied across the detector. Finally, the charges are collected and accumulated on the pixel capacitor and are read out using back-end electronics. Our group recently reported on a direct detector model (*Badal et al.*, 2020a), based on MC x-ray transport simulations, adapted from PENELOPE 2006 (*Salvat et al.*, 2006). This model was used to emulate the imaging performance of the SIM system, for an in silico imaging trial evaluating DBT as a replacement for DM (*Badano et al.*, 2018). In this chapter, we will be first presenting the equations for direct a-Se based detector, developed for SIM system. The model is mainly adapted from the work by Badal et al. (*Badal et al.*, 2020a), but includes an improved method for simulating the additive electronic noise. We will also be presenting modifications to the direct detector model to emulate performance of the HSD system.

SIM model

Fig. 3.1 shows the model for the direct a-Se based detector (*Badal et al.*, 2020a). As shown in the figure, the model includes the effects of fluorescence escape, a-Se ionization energy as well as additive electronic noise. The complete model and further details can be found in Badal et al. (*Badal et al.*, 2020a). In each simulation, a large number of x-ray photons are generated and tracked, in terms of position, energy and direction, from the source, through the breast model to the detector. Inside the detector, as shown in Fig. 3.1, an x-ray photon, n, with energy E_n, is tracked till its first photoelectric interaction. It is possible that the x-ray photon, depending on its entrance angle, leaves the detector without any interaction at all. The model also takes fluorescence effects into account by generating and tracking a new x-ray (based on the fluorescence yield probability) with energy E_k, in a random direction. The simulation thus tallies the total energy deposited in each detector pixel (X, Y) as shown in Fig. 3.1:

$$E(X,Y) = \sum_{0}^{P(X,Y)} E_n + \sum_{0}^{P_{Fl}(X,Y)} (E_n - E_k) + \sum_{0}^{Fl(X,Y)} E_k. \tag{3.1}$$

The energy deposited in each pixel is used to sample a mean number of electron-hole pairs N_{ehp} from a Gaussian distribution, using the a-Se ionization energy W_0 and Swank factor A_s to calculate the mean and the standard deviation:

$$N_{ehp}(X,Y) = \mathcal{G}(\mu_{ehp} = \frac{E(X,Y)}{W_0}, \sigma_{ehp} = \sqrt{\frac{E(X,Y)}{W_0}\sqrt{\frac{1}{A_s - 1}}}). \tag{3.2}$$

In the original work by Badal et al. (*Badal et al.*, 2020a), to replicate the presence of electronic noise, a random sample from a Poisson distribution is added to the mean detected signal in each pixel:

$$N_d(X,Y) = \mathcal{G}(\mu_d = \mu_{ehp} + N_e, \sigma_d = \sigma_{ehp} + \sqrt{N_e}). \tag{3.3}$$

Please note that we add the standard deviations for each process, and not the variances. As it is difficult to estimate the contribution of each error component, we overestimate the variance in the distributions by adding the standard deviations.

However, in this work since we are using an electronic noise value, N_e that is described as a RMS value (*Konstantinidis*, 2011), it should be ideally added to only the standard deviation and not the mean. Moreover, we found that with the original model, varying the electronic noise, even at lower exposures, did not produce the expected variations in the noise power spectrum plots. So, we propose the following electronic noise model:

$$N_d(X,Y) = \mathcal{G}(\mu_d = \mu_{ehp}, \sigma_d = \sigma_{ehp} + N_e). \tag{3.4}$$

The pixel values are calculated using g_0, a random number sampled from a Gaussian distribution described with zero mean and a standard deviation of 1, as:

$$PV(X,Y) = \mu_d + g_0\sigma_d \tag{3.5}$$

Here, μ_d and σ_d are the mean and standard deviation of the distribution in equation 3.4.

The complete set of parameters used in this model are described in Table 3.2.

Badal et al. simulated MTF, NNPS and DQE curves and compared them to measured data. However, the NNPS and DQE curves were plotted for a single exposure level. In this work, we show the variation of the NNPS and DQE curves with exposure and compare them with measured data.

HSD model

The HSD system also employs the a-Se based direct detector technology, similar to the SIM system. However they differ in system geometry and other image acquisition

Parameter	Value	Description
W_0	50 eV	a-Se Effective Energy
γ	16 eV	CsI detector gain (*Howansky et al.*, 2017)
A_s	0.99	Swank Factor for a-Se and CsI (*Howansky et al.*, 2017)
N_e	5200 e/pixel	Electronic Noise (*Konstantinidis*, 2011)
E_k	11.223 keV	Fluorescence Energy for a-Se
	33 keV	Fluorescence energy for CsI
O^z	-	Depth-dependent point spread function for CsI detectors
x_o, y_o	-	Pixel coordinates of O^z
E_n	-	Energy of x-ray photon n
$P(X,Y)$	-	Number of photons that reach pixel (X,Y) after only a photoelectric interaction
$P_{Fl}(X,Y)$	-	Number of photons that reach pixel (X,Y) and produce fluorescence
$Fl(X,Y)$	-	Number of fluorescent x-ray photons that reach pixel (X,Y)
x, y	-	Coordinates of the x-ray photon's location of interaction in the detector
z	-	Height of interaction
PV	-	Pixel values
N_{ehp}	-	Mean number of electron hole pairs
N_d	-	Mean detected signal
$K_{crosstalk}$	-	Crosstalk kernel for the HSD system
ρ_c	-	Matrix coefficients of the crosstalk kernel for the HSD system

Table 3.2: Model parameters for the direct and indirect x-ray detectors (*Badal et al.*, 2020a).

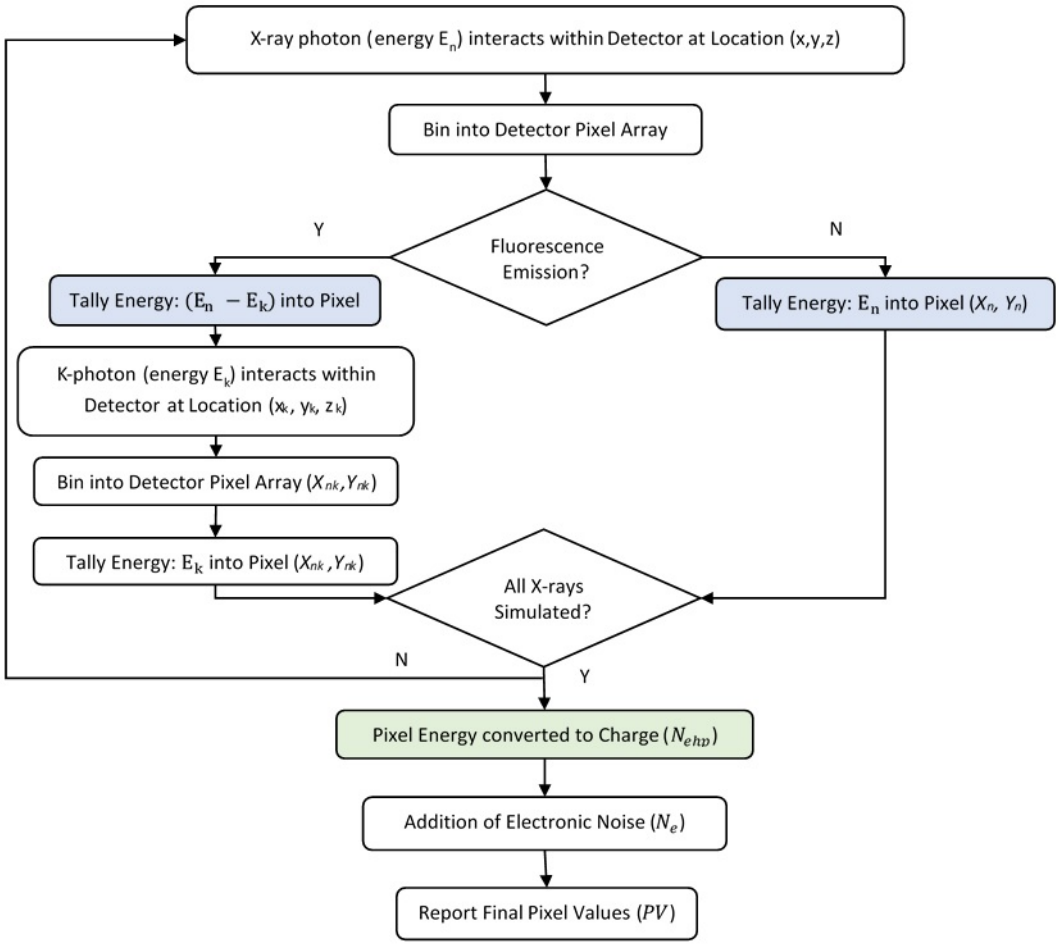

Figure 3.1: Generic model for x-ray detectors. It is applicable, as is, to direct a-Se based detectors. For the HSD and GSP systems, the entire x-ray photon energy is not tallied within a single detector pixel, which affects the method for tallying energies in the detector pixels (blue boxes). For the HSD system, a crosstalk kernel is used to distribute a small fraction of the incident energy to the neighboring 8 pixels. A depth-dependent point spread function is used to define the extent of the optical blur in indirect detector based GSP system. For indirect CsI based detectors,the process of conversion of pixel energy to charge carriers (green boxes) is also modified.

parameters as noted in Table 3.1. The HSD system has a smaller pixel size (70 μm), compared to the SIM system (85 μm). Ideally, smaller pixel sizes should translate to higher spatial resolution of the imaging system, or a better MTF. However previous studies have shown that the MTF at the Nyquist frequency for the HSD detector

is 0.35, which is much lower than a MTF of 0.5 for the SIM detector (*Mackenzie et al.*, 2017). There are several factors that could contribute to the deterioration of the resolution properties for the HSD system such as: (i) introduction of controlled blurring to counter noise aliasing issues from smaller pixels, (ii) trapping of charges within the detector's blocking layer and (iii) cross talk between detector pixels. For this model, we assume that the crosstalk between the pixels is the primary cause of the loss of resolution for the HSD detector.

Crosstalk occurs when a small amount of collected charges during an exposure in a pixel contaminates its neighbouring pixels. The main type of crosstalk that we have considered here is electrical crosstalk, which is a result of pixel-to-pixel charge diffusion. The x-ray generated charges could undergo the lateral movement to the adjacent charge accumulation areas. This lateral movement strongly depends on the pixel architecture, charge accumulation areas, and intra-pixel sensitivity distribution. Electrical crosstalk is a major concern in many imaging technologies, including CMOS sensors (*Mahato et al.*, 2018).

For the HSD system, we assume that when a single pixel is illuminated, the signal is mainly located in the incident pixel and the neighboring 8 pixels share a small fraction of the total signal. To describe this mathematically, we developed a crosstalk kernel, represented by a 3×3 matrix (*Mahato et al.*, 2018):

$$K_{\text{crosstalk}} = \begin{bmatrix} \alpha & \beta & \alpha \\ \beta & 1-4(\alpha+\beta) & \beta \\ \alpha & \beta & \alpha \end{bmatrix} \tag{3.6}$$

Here, β is the fraction seen by the adjacent pixels, while α is a smaller fraction seen by the diagonal pixels. In reality, there can exist a noticeable asymmetry along the rows and columns of the imager which eventually introduces an asymmetry in the kernel coefficients between rows and columns as well as in the four corners. However,

physical measurements will have to be performed to verify the true nature of crosstalk in the the HSD imager. For simplicity, we have assumed a symmetrical crosstalk kernel, with $\alpha = 0.02$ and $\beta = 0.04$. The values for α and β were estimated to provide the most reasonable match with the measured data. Thus, the central pixel would accumulate 76% of the incident signal. So, instead of tallying the entire x-ray photon energy in a single pixel, a small fraction of it is spread to its neighboring pixels, to reproduce the detector crosstalk. The total energy aggregated in each pixel for the HSD detector could be expressed as:

$$E(X,Y) = \sum_{0}^{P(X,Y)} E_n \rho_c + \sum_{0}^{P_{Fl}(X,Y)} (E_n - E_k)\rho_c + \sum_{0}^{Fl(X,Y)} E_k \rho_c. \tag{3.7}$$

Here ρ_c could be any of the matrix coefficients in $K_{crosstalk}$, based on where the original signal is collected. The rest of the model is the same as the SIM detector.

Indirect detectors

Indirect x-ray detectors based on scintillating materials like thallium-doped cesium iodide (CsI:Tl) convert the incident x-ray energy to charge in a two step process. These detectors first absorb the incident x-ray energy and convert it into optical photons. The photo-electric effect is also the main x-ray interaction in CsI:Tl detectors. However, instead of creating secondary electron-hole pairs, the primary electrons generate light quanta. The optical photons are then converted into electric charge by a large photodiode array. The charge stored on the storage capacitor is then read out using back-end electronics, similar to the a-Se based direct detector.

Depth-of-interaction effects

Depending on the depth at which the the optical photons are generated, they can travel longer distances within the scintillator, before they are detected by the photodiode. This phenomenon introduces an additional spread of the signal, which is

not observed in direct detectors and needs to be modeled. Previous work by Freed et al. (*Freed et al.*, 2010) suggests that the depth dependent optical spread of the optical photons in CsI scintillators is best described by a Lorentzian function:

$$L^z(x,y) = \frac{1}{(1 + c_1^2(x^2 + y^2))}. \tag{3.8}$$

Here, c_1 is related to the full-width-at-half-maximum (FWHM) of the spread, τ, as:

$$c_1 = \frac{2}{\tau} = \frac{2}{g_0 z + g_1}. \tag{3.9}$$

τ is modeled as a linear function of the height of interaction, z measured from the bottom of the detector. Freed et al.(*Freed et al.*, 2010) fit the full-width-at-half-maximum of the Lorentzian as a linear function of depth to data from a full Monte Carlo model of the indirect detector, MANTIS(*Sharma and Badano*, 2013), to estimate g_0 and g_1 to be 0.17 and 15.44 μm respectively (*Freed et al.*, 2010). 1D profiles of $L^z(x,y)$ plotted from the point of interaction as a function of the depth, as shown in fig. 3.2. The depth-dependent collection efficiency can be approximately modeled as a linear function of z (*Freed et al.*, 2010):

$$\zeta_z = 0.01(b_0 z + b_1). \tag{3.10}$$

Here, b_0 and b_1 are fitting parameters with values of -0.0029 and 0.9164 (*Freed et al.*, 2010). These coefficients describe a linear fit(*Freed et al.*, 2010) to the collection efficiency as a function of depth, generated using MANTIS simulations(*Sharma and Badano*, 2013). The resulting collection efficiency as a function of depth is shown in fig. 3.2.

Finally, the depth-dependent optical point spread function, O^z can be calculated

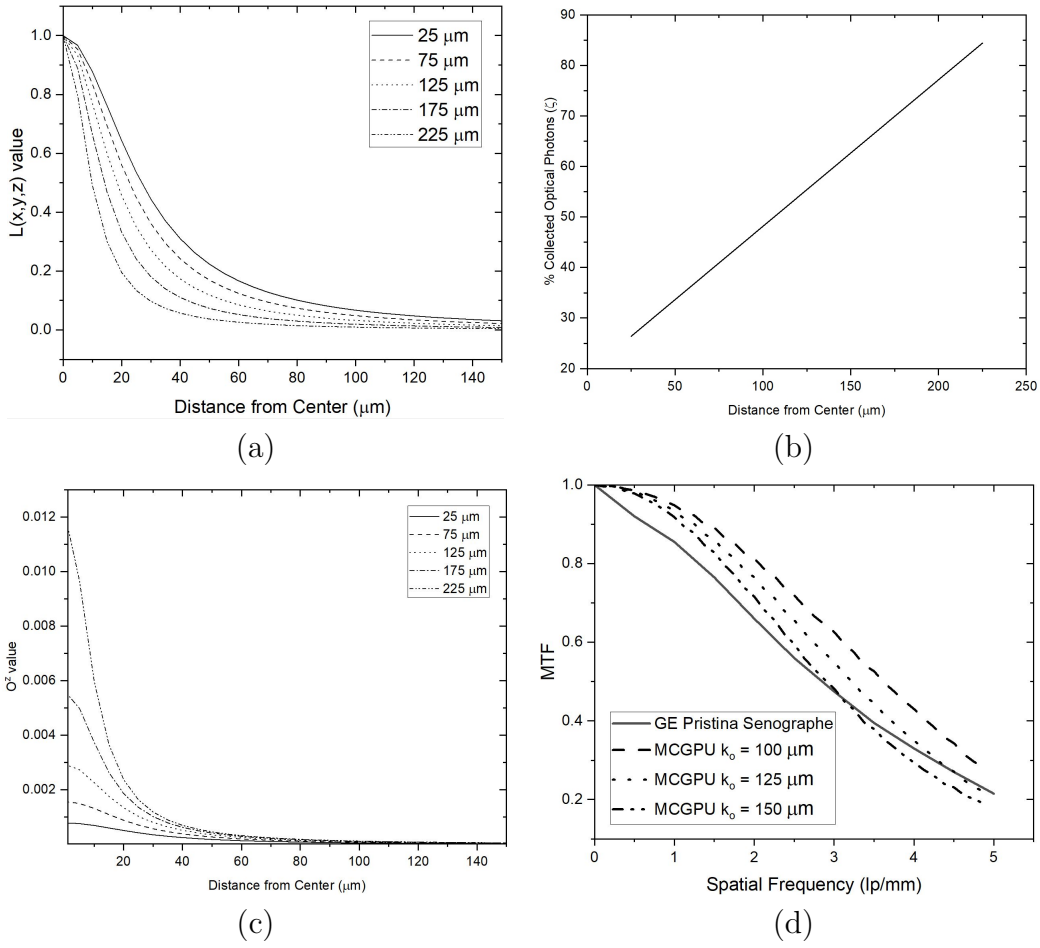

Figure 3.2: (a) Optical photon spread ($L^z(x, y)$), (b) Collection efficiencies ζ, (c) Normalized depth dependent optical point spread function, O^z at various depths inside the detector (25-225 μm) and (d) Variation of MTF with the kernel size of O^z. The variable, k_o, represents the lateral distance (orthogonal to z) from the point of interaction.

as:

$$O^z = \frac{\zeta_z}{N} L^z(x, y), \tag{3.11}$$

with a normalization factor

$$N = \sum L^z(x, y). \tag{3.12}$$

Fig. 3.2 (d) includes MTFs generated using $O(z)$ functions computed up to distance, k_o, ranging from 100 - 150 μm from the location of interaction. The variable, k_o, represents the lateral distance (orthogonal to z) from the point of interaction, i. e.,

the limits for variables x and y in equation 3.12. As expected, more extensive kernel sizes capture more of the tails in the $O(z)$ function and yield an MTF lower-frequency drop. MTFs calculated using the response functions computed up to 125 μm differ from the measured data by 9% on average.

GSP model

Fig. 3.3(a), shows modifications to the direct model (see Fig. 3.1), for replicating an indirect CsI based detector. Ideally, an unique O^z response function should be calculated for each x-ray photon based on its depth of interaction. However, this computation could considerably slow down the entire simulation. So instead, the optical spread is implemented using a pre-computed set of the O^z functions at various detector depths of 25, 75, 125, 175 and 225 μm. Based on the x-ray photon's depth of interaction, the corresponding O^z function is selected, which determines the distribution of the x-ray energy in the neighboring detector pixels.

Thus, similar to the direct detector model, the total energy of simulated x-ray photons aggregated in the indirect detector pixel (X,Y) can be calculated as:

$$E(X,Y) = \sum_{0}^{P(X,Y)} E_n O^z(x_o, y_o) + \sum_{0}^{P_{Fl}(X,Y)} (E_n - E_k) O^z(x_o, y_o) + \sum_{0}^{Fl(X,Y)} E_k O^z(x_o, y_o). \tag{3.13}$$

Here, x_o, y_o denotes the pixel coordinates of O^z, that overlap with the detector pixel (X,Y), as a function of the physical coordinates x and y of the x-ray photon's interaction location within the detector. For cases where O^z does not overlap with the detector pixel (X,Y), then the photon energy does not contribute to the pixel signal ($O^z = 0$). Equation 3.13 is very similar to eq. 3.7, except that for the HSD, the signal is spread to a fixed number of detector pixels and the kernel is always perfectly aligned with the detector array. On the other hand, O^z is centered at the point of

interaction, which may or may not be perfectly at the middle of its corresponding detector pixel.

As, shown in Fig. 3.3, the pixel energy is then used to sample a mean number of optical photons N_{op}, from a Gaussian distribution:

$$N_{op}(X,Y) = \mathcal{G}(\mu_{op} = \frac{E(X,Y)}{\gamma}, \sigma_{op} = \sqrt{\frac{E(X,Y)}{\gamma}\sqrt{\frac{1}{A_s - 1}}}). \tag{3.14}$$

The number of charge carriers generated by the photodiode is finally sampled from a Poisson distribution:

$$N_{ehp}(X,Y) = \mathcal{G}(\mu_{ehp} = \eta\mu_{op}, \sigma_{ehp} = \sigma_{op} + \sqrt{\mu_{ehp}}). \tag{3.15}$$

The electronic noise is added to each pixel using the same equations for the direct detector:

$$N_d(X,Y) = \mathcal{G}(\mu_d = \mu_{ehp}, \sigma_{ehp} = \sigma_{ehp} + N_e. \tag{3.16}$$

The pixel values are then calculated as follows,

$$PV(X,Y) = \mu_d + g_0\sigma_d. \tag{3.17}$$

The complete set of parameters used in this model are described in Table 3.2.

Experimental comparison

We compared the imaging performance predicted by the computational models against measured data using image quality metrics typically used in clinical practice. There are several metrics that could be used for characterizing DM/DBT systems such as modulation transfer function (MTF), normalized noise power spectrum (NNPS), detective quantum efficiency (DQE), signal-to-noise ratio (SNR), contrast detail curves etc. In this work, we will be focusing sharpness/resolution (MTF) and

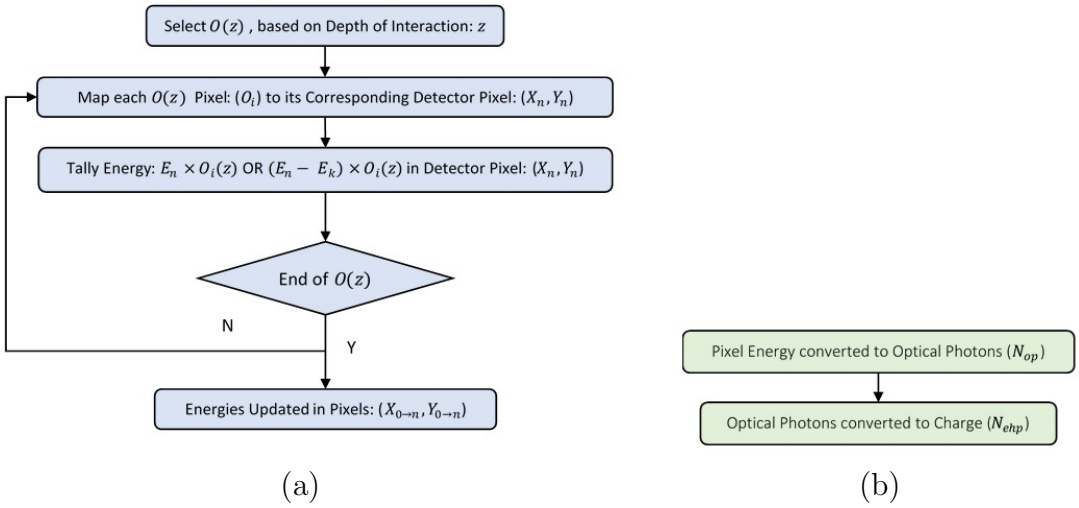

Figure 3.3: Modifications to flowchart in Fig. 3.1 for modeling an indirect CsI based detector. (a) Implementation of depth dependent spread of optical energy. This flowchart will replace the blue boxes in Fig. 3.1. (b) Conversion of pixel energy to charge carriers in indirect detectors. This will replace the green box in Fig. 3.1.

noise (NNPS) properties of the DM/DBT systems. Using the MTF and NNPS data, we will also be generating DQE data:

$$DQE(f) = \frac{MTF^2(f)}{K_a q_0 NNPS(f)}. \tag{3.18}$$

Here, q_0 is the mean x-ray photon fluence per unit air kerma and K_a is the air kerma at the detector entrance.

The simulated results for the SIM model were compared to experimental measurements performed on the same ANRAD detector used in the SIM system, previously published by Makeev et al. (*Andrey et al.*, 2018). The measured data for the GSP system was obtained from the equipment report for the system released by the National Health Service (NHS) in UK (*Oduko and Mackenzie.*, 2019). We measured the image quality metrics for the HSD system in the labs at the FDA White Oak campus.

All measurements for the HSD system (model number SDM-05000-2DC) were performed using the W/Rh anode and filter combination at 28 kVp with the antiscatter

grid out as recommended by the IEC standard. A 1mm thick aluminium filter was attached at the tube head, instead of a thick block of PMMA. We first acquired several flat field images at different current and exposure time (mAs) levels, to calculate the response function of the detector. A freely available ImageJ plugin (*Donini et al.*, 2014), was used to calculate the response function and linearize all the images to ensure that the pixel value maintains a linear relationship with energy absorbed per unit area in the detector. The MTF was measured using the slanted edge method, with a 120×60 mm^2 0.8 mm thick stainless steel plate as a test device. The edge of the plate was placed at approximately 2.7° angle with respect to the detector rows. The edge spread function, line spread function and subsequently the MTF were calculated using the ImageJ plugin (*Donini et al.*, 2014). The NNPS and finally DQE curves were calculated using the same plugin with the linearized flat field images at various exposure levels. The air kerma at the detector level was measured using a radcal ionization chamber with a dosimeter.

Using the same acquisition parameters as the physical measurements, edge images were simulated using an in silico version of the steel edge model for the various system models. Similarly, we also simulated flat-field images at various exposure levels. The air kerma level was estimated by calculating the average energy deposited in a 2 × 2 × 2 mm^3 air volume at the entrance of the detector. The same ImageJ plugin (*Donini et al.*, 2014) was used to extract the MTF, NNPS and DQE data for the simulated images.

3.4 Results

Experimental Data

Fig. 3.4 shows all the measurements from the HSD system that we performed. As expected, the average pixel values, shown in Fig. 3.4 (a), follow a linear relationship

with the incident air kerma. The response function was calculated to be a straight line with a slope of 2.208 and y axis intercept of 53.412. The y axis intercept basically represents an internal offset that the HSD system applies. Fig. 3.4 (b) shows the system MTFs along two orthogonal directions. For ideal detector with square pixels, the MTF plots along the two orthogonal directions should coincide. However, for the HSD system, the MTF along the horizontal direction is lower than that in the vertical direction, especially in the lower frequencies. Crosstalk between gate lines along the horizontal direction could possibly contribute to the observed degradation of spatial resolution. Figs. 3.6 (b) and (c), show the variation in the NNPS and DQE characteristics with incident air kerma.

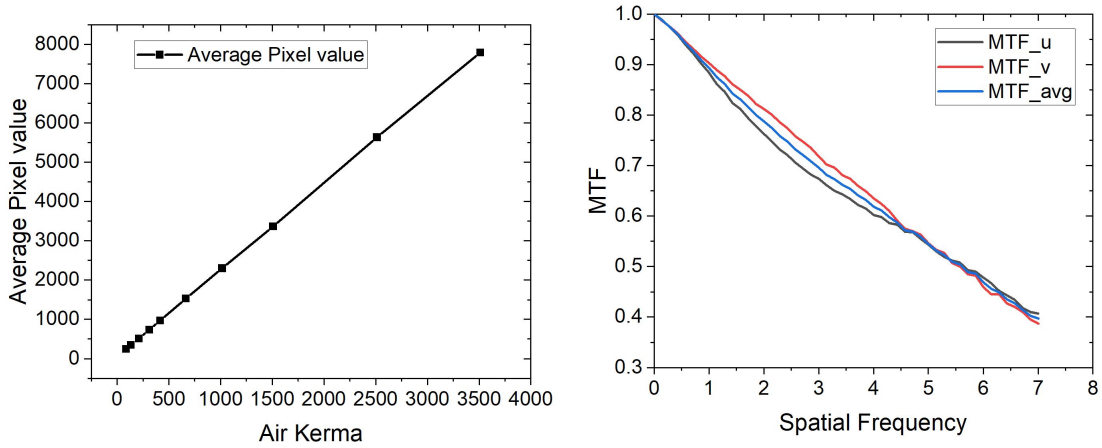

(a) (b)

Figure 3.4: Measured data from the HSD system. (a) Response curve (b) MTF plots along two orthogonal directions

Comparison with experimental data

Fig. 3.5 shows the MTF, NNPS and DQE plots for the GSP system. The red and black plots represent simulated and measured data respectively. The MTF shown in Fig. 3.5(a) is simulated using a O^z function computed up to 125 μm from the location of interaction. In a previous publication (*Sengupta et al.*, 2022), we have shown that the MTF at lower frequencies drops when longer tails up to 150 μm are included in the

O^z function. However, we observed that the simulated MTF matched the measured data for the GSP system best when computed up to 125 μm. On average the difference between the measured and simulated MTF data is 9%. The simulated NNPS curves are compared against measured data in Fig. 3.5(b), for three air kerma levels from 20 μGy to 134 μGy. As the figure shows, the shapes of the measured and simulated NNPS plots match closely and on average the difference between them is 18%. Fig. 3.5(c) shows the simulated DQE plots compared against measured data. While, the shapes of simulated and experimental plots look similar, the DQE(0) values for the simulated curves are higher than that of the measured data.

Fig. 3.6 and Fig. 3.7 show the MTF, NNPS and DQE plots for the DM/DBT systems that use direct detector technology. In previous work (*Sengupta et al.*, 2022), we simulated the MTF plots for the HSD system using the same model for the SIM system accounting for their differences in geometry. We found that the there was significant difference (up to 30 %) between the simulated and measured plots. By introducing an additional source of signal spread from the inter-pixel cross talk, we observed that the simulated MTF better represented the measurements (see Fig. 3.6 (a)). On average the difference between the measured and simulated MTF data is 4%. As shown in Fig. 3.6, the difference in the blue and red plots illustrates the effect of crosstalk and the subsequent degradation of the detector's resolution properties. The simulated NNPS curves are compared against measured data in Fig. 3.6(b), for three air kerma levels from 86 μGy to 210 μGy. As the figure shows, the shapes of the measured and simulated NNPS plots match closely but the absolute values are very different. There is a good match at lower exposure levels of 86 μGy. However, the HSD system seems to introduce additional sources of noise at exposure levels greater than 100 μGy, which we have not modeled. This is reflected in the DQE measurements as well, shown in Fig. 3.6(c). Contrary to the expected trend, the DQE curve for the lowest exposure is higher than those for higher exposure levels.

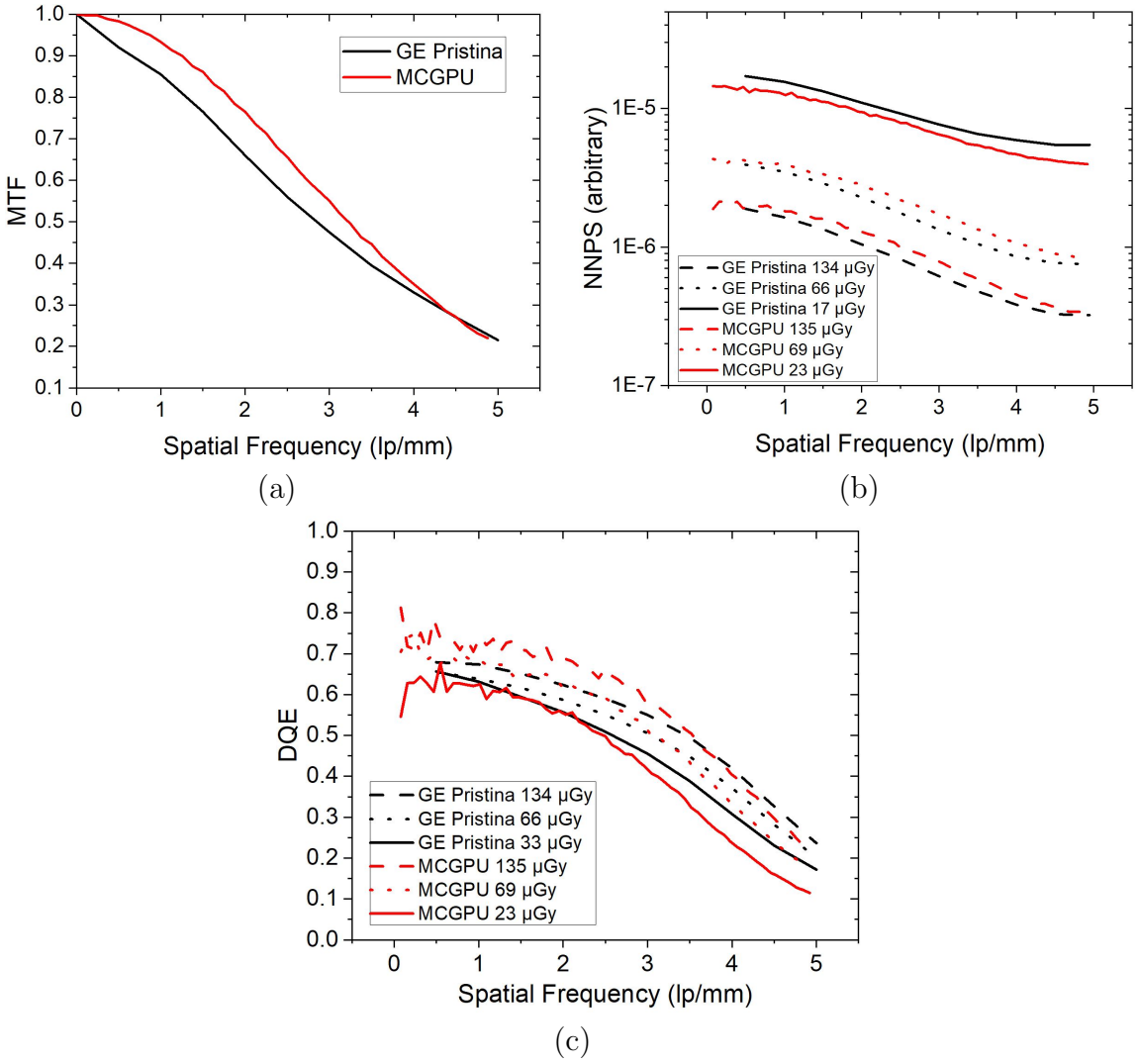

Figure 3.5: Comparison of simulated image quality metrics with experimental data for the GSP system. (a) MTF plots computed from vertical edge images (b) NNPS plots extracted from flatfield images at various air kerma levels and (c) DQE plots. The red and black plots represent simulated and measured data respectively.

Moreover, DQE(0) values for the HSD system at similar exposure levels are much lower than the observed values for the GSP and SIM systems. So there is significant discrepancy between the measured and simulated DQE curves for the HSD system.

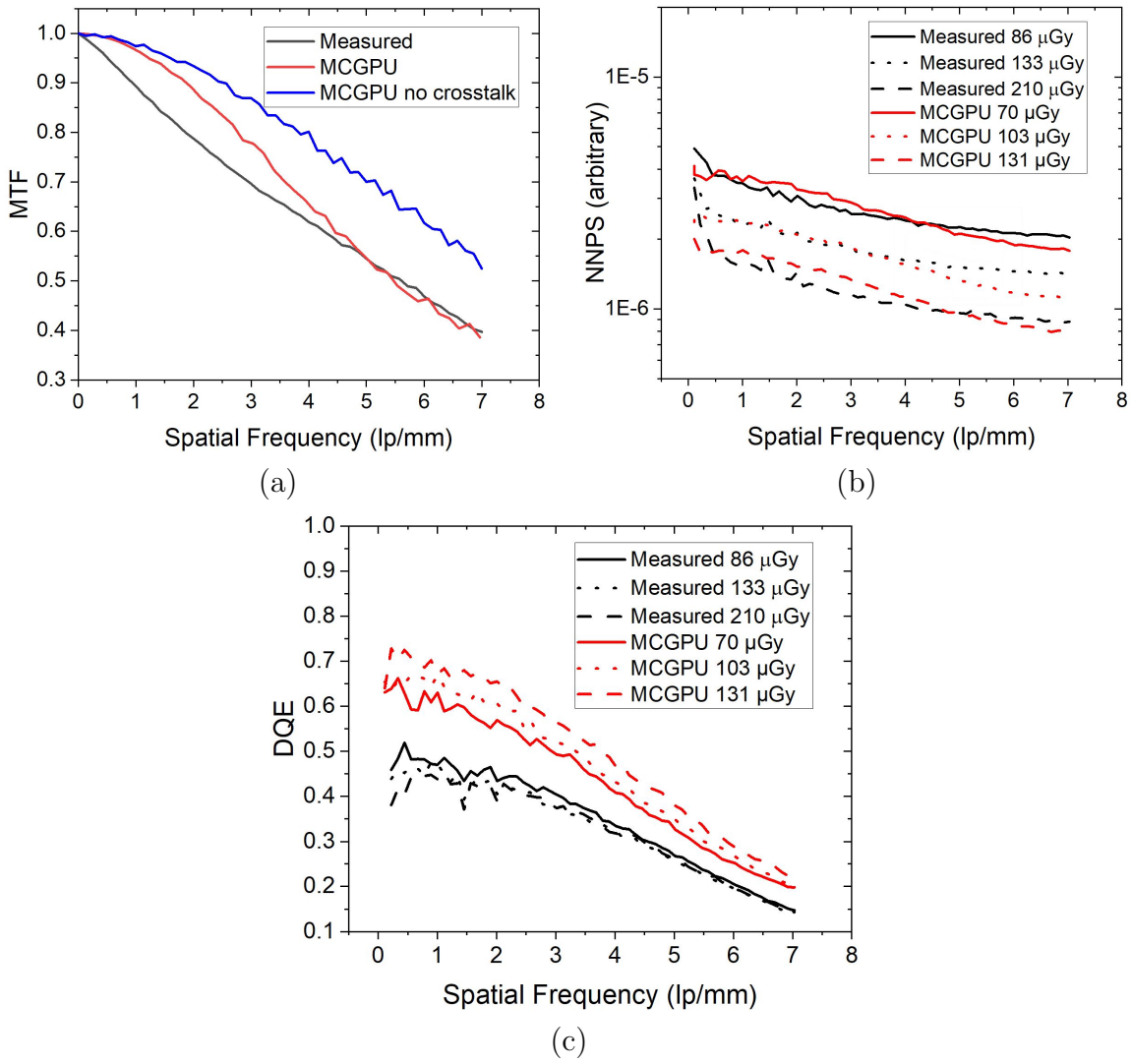

Figure 3.6: Comparison of simulated image quality metrics with experimental data for the HSD system. (a) MTF plots computed from vertical edge images (b) NNPS plots extracted from flat-field images at various air kerma levels and (c) DQE plots.The red and black plots represent simulated and measured data respectively.

Effect of electronic noise

Fig. 3.8 shows the variation of the NNPS and DQE plots with electronic noise. Physics suggests that increase in electronic noise should result in increase of the NNPS plots and reduction of DQE at low exposure levels. We simulated flat-field images for the HSD system using both noise models described in this chapter. The flat-field

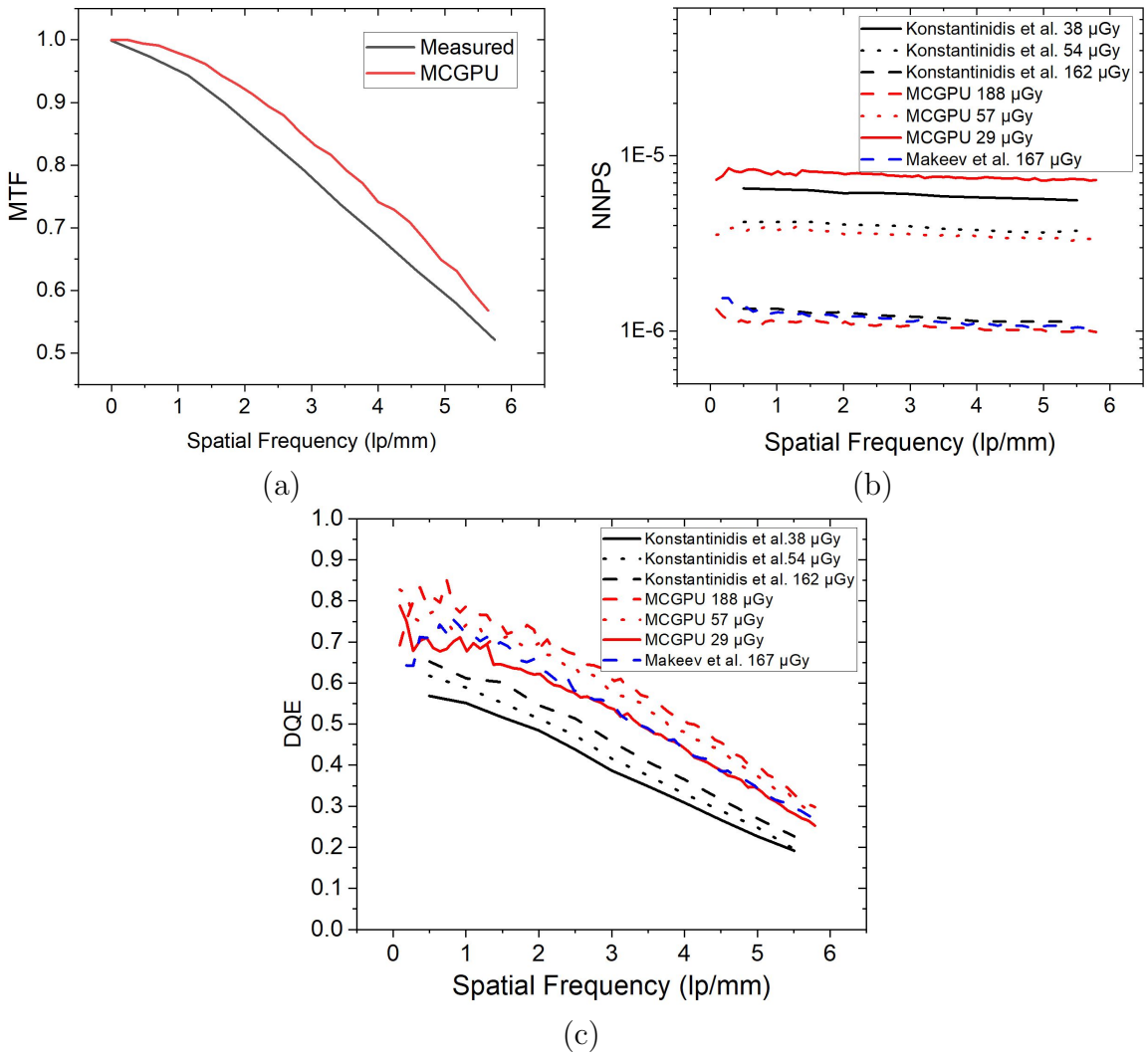

Figure 3.7: Comparison of simulated image quality metrics with experimental data for the SIM system. (a) MTF plots computed from vertical edge images (b) NNPS plots extracted from flat-field images at various air kerma levels and (c) DQE plots. The red and black plots represent simulated and measured data respectively.

were simulated at an air kerma level of 70 μGy at the detector, which is the lowest that can be achieved with the HSD system. The electronic noise was varied from a very low level of 2000 to 8000 electrons RMS. It has been shown that lower levels of electronic noise of 1250 electrons can be achieved, but with CMOS passive pixel flat panel sensors (*Hamamatsu C9732DK CMOS PPS Detector*, 2015), instead of the traditional TFT based passive pixel sensors used in the DM/DBT systems. As

shown in Fig. 3.8 (a) and (b), with the older noise model proposed by Badal et al., there is no variation in the NNPS plots or in the DQE plots, which is contrary to the expected trend. The model proposed by Badal et al. increases the mean pixel values by the electronic noise value (5200 electrons for the HSD model) and their standard deviation by its square root (72 electrons). Since the standard deviation increases by a very small amount compared to the average pixel value, which is of the order of 10^5 electrons, the effect of varying electronic noise is not reflected in the NNPS or DQE curves. However, instead of changing the mean pixel values, the noise model proposed in this chapter increases their standard deviation by the electronic noise value. Figs. 3.8 (c) and (d) illustrate the expected trend in the NNPS and DQE characteristics. With increasing electronic noise, the NNPS plots increase, while DQE drops. Since electronic noise is white noise, which does not vary with spatial frequency, flattening of the NNPS curves especially at higher frequencies and electronic noise values can be observed in Fig. 3.8.

Fig. 3.8 also includes measured data from the HSD system at 86 μGy (black dotted line). Both the NNPS and DQE data generated using the noise model proposed by Badal et al. shows a significant deviation, especially at higher frequencies on the NNPS. In comparison, the curves generated with the noise model introduced in this work better match the measured data. While the effect of electronic noise is important, it should be noted that its effect is only significant at very low exposure levels. At clinically relevant exposure levels for mammograms are acquired, quantum noise is the dominant component. However, electronic noise could play an important role in the acquisition of low exposure projections for DBT.

We also investigated the difference in simulation times for the three models for generating an edge image for MTF calculations. For a total of 1.7×10^{10} primary x rays, the timings on 4 GeForce GTX 1080 GPUs are 15, 18, and 790 s respectively for the SIM, HSD, and GSP model. For simulating mammograms of a fatty breast

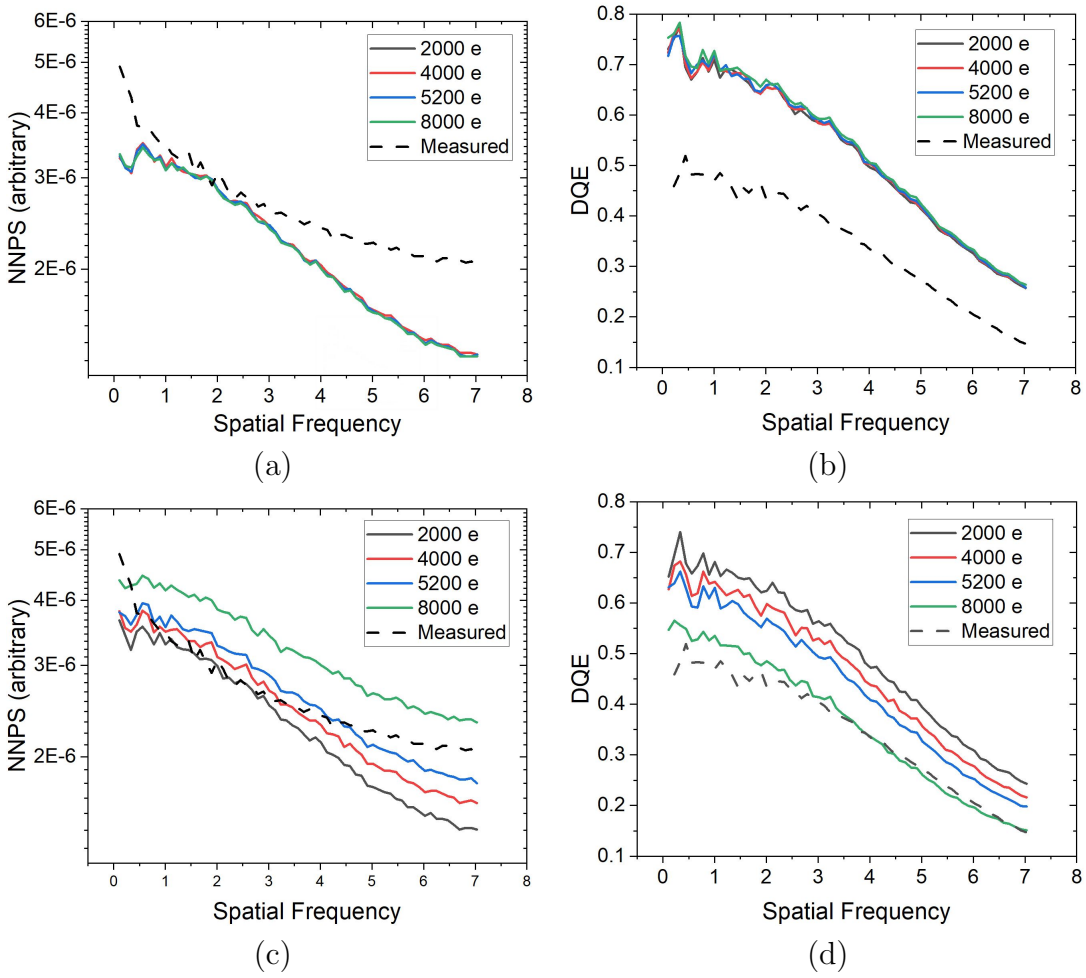

Figure 3.8: Variation of NNPS and DQE characteristics with electronic noise at 70 μGy. (a), (b) with noise model proposed by Badal et al. (c) and (d) with noise model proposed in this chapter.

model shown in fig 3.9, using a total of 3.7×10^{11} histories, the timings on 2 GeForce GTX 1080 GPUs are 3165, 3233 and 42859 s respectively for the SIM, HSD, and GSP models. As expected, the GSP system slows down the computational speed considerably, as compared to the SIM and HSD systems due to the need for mapping each point in the O^z function into the corresponding detector pixel. However, this method is still faster compared to full MC approaches(*Sharma and Badano*, 2013; *Sharma et al.*, 2012) used in the past.

Fig. 3.9 (b) and (c) shows ROIs from fatty breast model, containing spiculated

masses and microcalcification clusters as the signals, imaged using the three detector models. An example DM simulated with the SIM model is depicted in Fig. 3.9 (a). This breast model was generated using the VICTRE (*Sharma et al.*, 2019; *VICTRE Github Repository*, 2018) pipeline. For generating these example images, the x-ray spectrum, source to detector distance, number of histories and other system parameters were kept identical and only the detector model was changed to highlight any differences due to changes in the detector technology without the influence of system characteristics. For viewing the calcification clusters and masses in the DMs, the same ROI sizes in the object space and image processing methods were used. As shown in the fig. 3.9 (b), the ROIs generated using the direct detector models look quite similar, but since the pixel sizes vary across the 3 systems, the ROI sizes in pixels are different, In addition, the GSP ROIs look blurred and the noise texture appears different, as compared to the systems with direct detectors.

3.5 Discussion

In this chapter, we have developed models from first principles to replicate the performance of three FDA approved DM/DBT systems. These models were used to simulate standard image quality metrics such as MTF, NNPS and DQE, which are used to evaluate imaging performances of DM/DBT systems. The simulated image quality metrics showed a reasonable match with measured data.

While this was an useful first step towards developing in silico versions of DM/DBT systems available on the market, there are some limitations of the study. Although the results (see Fig. 3.5 and Fig. 3.7) for systems like SIM and GSP show a close match with the measured data, a significant difference was observed for the HSD system. It should be noted that the measured data for the HSD system also shows significant deviation from measured data for the SIM system which uses the same detector technology. We have accounted for the lower MTF properties by including

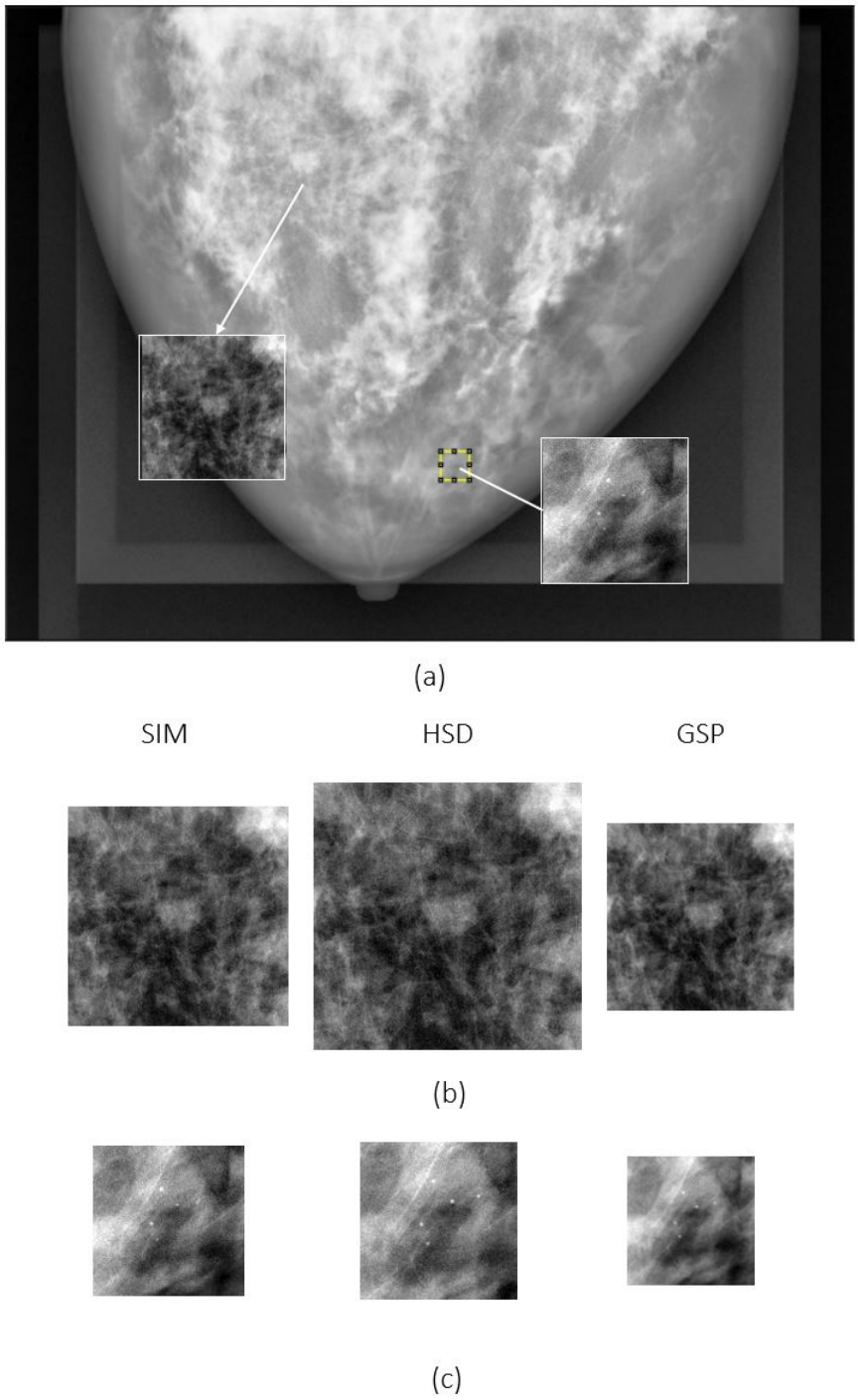

Figure 3.9: (a) A fatty breast model imaged using the SIM system. The inserts show ROIs with a mass and a calcification cluster. ROIs containing a (b) spiculated mass and (c) a microcalcification cluster were extracted from the DM images of the same breast model shown in (a), simulated using the three DM/DBT models: SIM, HSD and GSP.

additional signal spread, that we assume originates from crosstalk between pixels. The DQE data is also lower (0.67 for the SIM system at a spatial frequency of 0, compared to 0.45 for the HD system) and exhibits an unusual trend with respect to exposure levels. As seen from the data for the SIM system, as exposure increases the noise levels drop leading to increase in the DQE plots, which saturate at a certain exposure level. However, fig. 3.6 (c) for the HSD system shows that with increasing exposure, the DQE drops. This behavior is unusual and suggests that there are additional sources of noise that become significant at higher exposure levels. Since the exact source of the noise is unknown, it was not possible to include it in our model.

Other approaches that model detector performances such as cascaded systems modeling (*Sengupta et al.*, 2019; *Kim et al.*, 2008; *Zhao and Rowlands*, 1995; *Fang et al.*, 2012) (see appendix chapter on cascaded modeling) have been shown to achieve much better fits to measured MTF, NNPS as well as DQE data. However, cascaded systems modeling is a completely different approach that often relies on arbitrary fitting functions to match simulated resolution properties to the measured data (*Sengupta et al.*, 2019; *Zhao and Rowlands*, 1995) (see appendix chapter on cascaded modeling). These fitting functions are not derived from first principles and were not used in this work, except when proprietary information couldn't be obtained and released for systems such as HSD.

The simulated MTF plots, shown in Fig. 3.7(a), for the GSP system matches the measured data reasonably well. However, the model described in this chapter uses analytical functions described by Freed et al. (*Freed et al.*, 2010) to estimate the spread of the optical photons and doesn't explicitly model the columnar CsI structures or transport of each optical photon through the columns. Monte Carlo approaches such as MANTIS (*Badano and Sempau*, 2006; *Sharma and Badano*, 2013) and hybridMANTIS (*Sharma et al.*, 2012) have been developed in the past that model CsI based x ray detectors in detail. For each x ray photon that travels through

the columnar CsI structure, these approaches calculate the probability of it being absorbed in the bulk or at the top of the detector, getting reflected back from the bottom of the detector structure and being either transmitted or reflected at the columnar walls. Although these methods account for all the physical phenomena that contribute to the x-ray detection process in indirect detectors, they are very time consuming and thus not suited for use as part of in silico trials. Thus, our approach using analytical functions, which have been shown to reasonably match MANTIS results, offers a much faster and efficient alternative for modeling indirect detectors for in silico trials.

There are a few other limitations of the work presented in this chapter. We have implemented a simple model to replicate electronic noise in DM/DBT systems as the exact back-plane circuits are proprietary information and are unknown to us. The electronic noise for the ANRAD SMAM detector, which is used for the SIM system, has been reported to be 5200 electrons RMS. Since the GSP and HSD systems also use amorphous silicon TFT based passive pixel sensors as their readout electronics, it is reasonable to assume that the electronic noise level is similar in these systems. So for this work, we have assumed same value of 5200 electrons for the electronic noise across all systems. In this work, we have only investigated the systems in the DM mode and have not presented data at different angles or reconstructed volumes. We plan to include this data in a future chapter. It is also known that indirect detectors have a lower fill factor, due to presence of additional electronics such as photodiodes, which reduce the active photosensitive area of the pixels. However, we haven't studied the effects of the fill factor in our current model. We expect any fill factor less than unity will reduce the detected signal in the pixels. The effect will be similar to lowering the exposure at the detector entrance. In the direct detector model, we do not explicitly model trapping of electron hole pairs within the detector and assume that all generated electron hole pairs reach their respective electronics.

Since we do not model charge trapping, we can not model any temporal effects such as lag and ghosting. The detector models described in this work also do not account for any blurring due to patient motion during image acquisition.

3.6 Conclusions

We have presented computational models developed for simulating the imaging performance in the DM mode of three commercially available DM/DBT systems, which have received FDA approvals. These systems implement both types of detector technology - a-Se based direct as well as CsI indirect detectors. We compared the models' predictions for image quality metrics including MTF, NNPS and DQE against measured data. Our models show a reasonable match with measured data across all systems investigated in this work. The beta versions of the codes for modeling the various systems are available through GitHub as modules for the VICTRE simulation pipeline (*VICTRE Github Repository*, 2018).

CHAPTER IV

The First Freely Available Open Source Software Package for Performing 3D Image Reconstruction for Digital Breast Tomosynthesis.

4.1 Abstract

Digital Breast Tomosynthesis (DBT) improves the visibility of cancerous lesions as compared to 2D full-field digital mammography (FFDM) by removing the overlap in breast tissues. An integral and computationally demanding part of the DBT image acquisition process is the reconstruction of the volume from projections. To facilitate further research towards improving DBT technology, it is essential to have access to image reconstruction software that generates volumes within a reasonable amount of time. We have developed an open source version of the filtered back-projection (FBP) reconstruction algorithm for DBT using single-threaded C. This is an extention to the C codes developed by Leeser et al. for cone-beam computed tomography (CBCT) reconstruction. For each projection angle, the DBT projection view was interpolated to create an estimation of the corresponding CT projection view for that angle. The estimated CT projection views were then filtered and backprojected to generate the DBT volume. We tested our implementation using mathematical and anatomical phantom data and compared the results with a previously verified pure

MATLAB implementation. We observed negligible relative differences between the DBT reconstruction by both methods with a considerable increase (up to 9 times faster) in speed over the MATLAB code.

4.2 Introduction

One of the popular reconstruction techniques use by commercial DBT and CT scanners is the Filtered Back-Projection (FBP) method. FBP reconstruction, derived from the Fourier Slice theorem, first filters the projection views, obtained during the DBT/ CT image acquisition process, typically using a simple ramp function. However, due to presence of background noise in the clinically obtained projection views, it is often necessary to apply an additional filter function to suppress the high-frequency noise. These filtered projection views are then back-projected in accordance with the scanner geometry to form a reconstructed volume representing the object.

Previously, our group had developed FBP algorithms for DBT (*Zeng et al.*, 2015), written in MATLAB, using routines from Fessler's cone beam computed tomography (CBCT) reconstruction toolbox (*Fessler*, 2015). In this work, we have implemented a similar FBP reconstruction algorithm for DBT using single threaded C. We tested our implementation using one mathematical as well as an anatomical breast phantom data and compared the results with the previously verified MATLAB (*Zeng et al.*, 2015) version. We observed that while the relative differences between the DBT slices reconstructed by MATLAB and C were negligible, the C implementation offered a considerable increase in speed over MATLAB. (Note that the MATLAB version used for the comparison did not include any speedup of utilizing C source MEX file.) The FBP reconstruction software for DBT, described in this study, is freely available as open-source research on GitHub.

4.3 Methods

Our work is an extension of the single-threaded C code by (*Leeser et al.*, 2014), developed to perfrom FBP reconstruction of CBCT projections, for application in DBT reconstruction. To use the CBCT code for DBT reconstruction, we had to account for the differences in the image acquisition schemes between DBT and CT. First difference, in CT, the x-ray source and imager concentrically rotate around the object, thus acquiring the projection views in a way such that the x-ray source and imager are always normal to each other. On the other hand, in most DBT systems, the x-ray source moves in an arc about the object, while the imager remains stationary. So other than the 0 degree position, the x-ray source is not perpendicular to the imager. In addition, the z-axis of the object volume is normal to the detector plane in DBT whereas it is parallel to the detector's plane in CT.

To address these differences, as shown in Fig. 4.1, we have implemented the following methodology, based on the previously developed MATLAB version (*Zeng et al.*, 2015), for DBT reconstruction in C:

1. Use the DBT projections to estimate CBCT projection views at the corresponding projection angles
2. Reconstruct a volume from the estimated CBCT projections using FBP
3. Interchange the z and y axes to retrieve the DBT reconstructed volume

However, we discovered that the open source CT FBP algorithm developed by (*Leeser et al.*, 2014) could not be directly used due to errors in the implementation. Upon comparing the open source CT algorithm with Fessler's CT toolbox (*Fessler*, 2015), we corrected the errors, both semantic as well as logical. We tested and verified the performance of the modified CT code using a mathematical phantom from Fessler's image reconstruction toolbox (*Fessler*, 2015). This mathematical phantom is designed as a cylindrical object containing spherical inserts of different sizes at

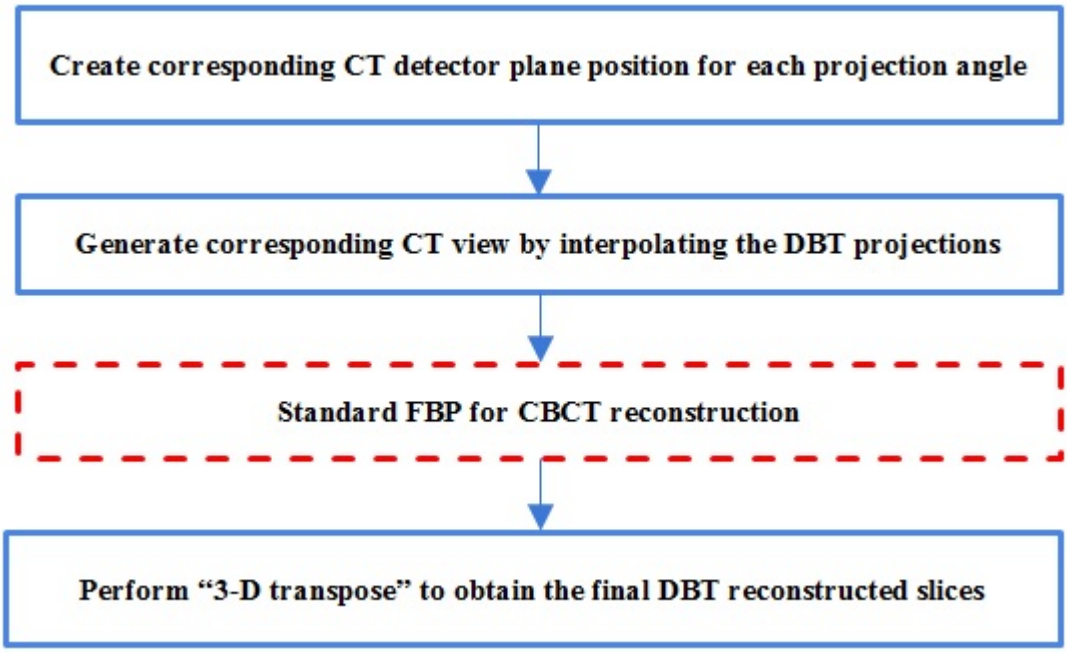

Figure 4.1: Methodology to perform DBT reconstruction using CBCT reconstruction algorithm. The block signified in dashed lines is a modified version of the C code developed by *Leeser et al.* (2014)

various locations.

Following verifying the correctness of the CBCT code, we extended it using the methodology shown in fig. 1, for DBT reconstruction. To test the performance of our DBT FBP code, we simulated DBT projection views of a virtual breast phantom using the VICTRE MC-GPU simulations (*Sharma et al.*, 2019; *Badano et al.*, 2018). The simulated DBT acquisition contained 25 projections with an angular range of 50 degrees. We then compared the reconstructed slices against the ones reconstructed using the MATLAB code, previously developed by (*Zeng et al.*, 2015). To compare the slices reconstructed using MATLAB and C, we computed the relative error as the difference between the MATLAB and C slices divided by the pixel values, reconstructed with the MATLAB code, in percentage.

4.4 Results

Our first aim was to verify the CBCT reconstruction code using a mathematical phantom and comparing the reconstruction to that from Fessler's matlab CBCT code. Fig. 4.2(a) shows the central slice of the mathematical phantom, 64 x 60 pixels, reconstructed using our C implementation of the CBCT FBP algorithm. To compare the C and MATLAB implementations, we plotted the pixel value of the central point through the 50 reconstructed slices. As shown in Fig. 4.2(b), the C and MATLAB profiles overlap and are in close agreement.

Upon verification of CBCT code, we modified it for DBT reconstruction of projection views for a VICTRE breast phantom. Fig. 4.3(a) and (b) illustrate one of the reconstructed DBT slices of the VICTRE breast phantom, 1136 x 483 pixels, using both C and MATLAB FBP codes. The differences between them are very small, with an absolute magnitude of the order of 10^{-6}, Fig. 4.3(c), and relative magnitude mostly in the level of 0.1%, as shown in the difference image in Fig. 4.4(b) and the histogram plot in Fig. 4.4(a). Therefore, the difference between the two implementations were negligible.

FBP reconstruction is computationally intensive, which becomes more challenging as the resolution of the projection views increases. One of the benefits of implementing FBP reconstruction in C, is the significant increase in FBP reconstruction speed over MATLAB - 3 times for the cylindrical and 9 times for the breast phantom. The speed-up of C over MATLAB is defined as the ratio of the FBP (or total) C run time to the corresponding MATLAB runtime. (Note that the MATLAB version used for the comparison did not include any speedup of utilizing c source MEX file.)

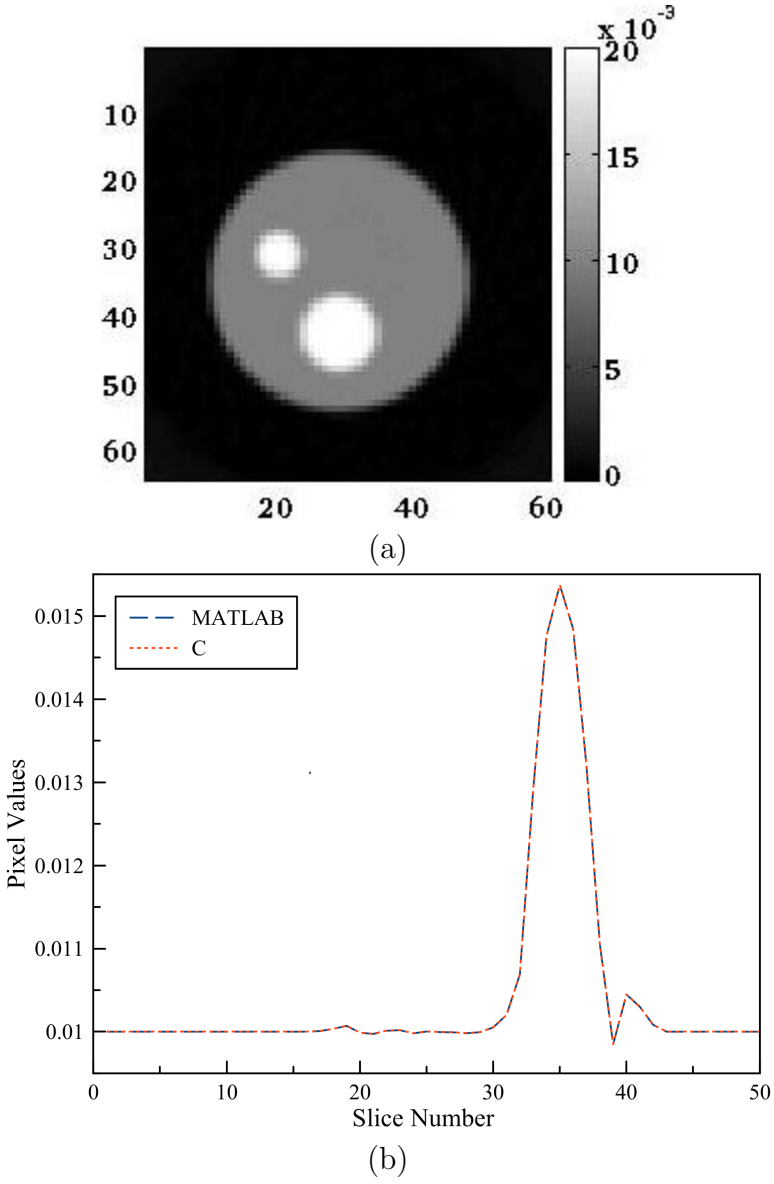

Figure 4.2: Central slice of reconstructed volume using single threaded C with pixel values ranging between -0.00029 and 0.0201 cm^{-1} and (b) Overlapping z-profiles from the MATLAB and C codes at coordinates: (31, 33) for all the reconstructed slices, indicating the similarity between the two versions.

4.5 Conclusion

We have presented our work on an open source DBT reconstruction software using single-threaded C that can considerably reduce reconstruction time compared to its MATLAB implementation.The reconstruction software for DBT and the cor-

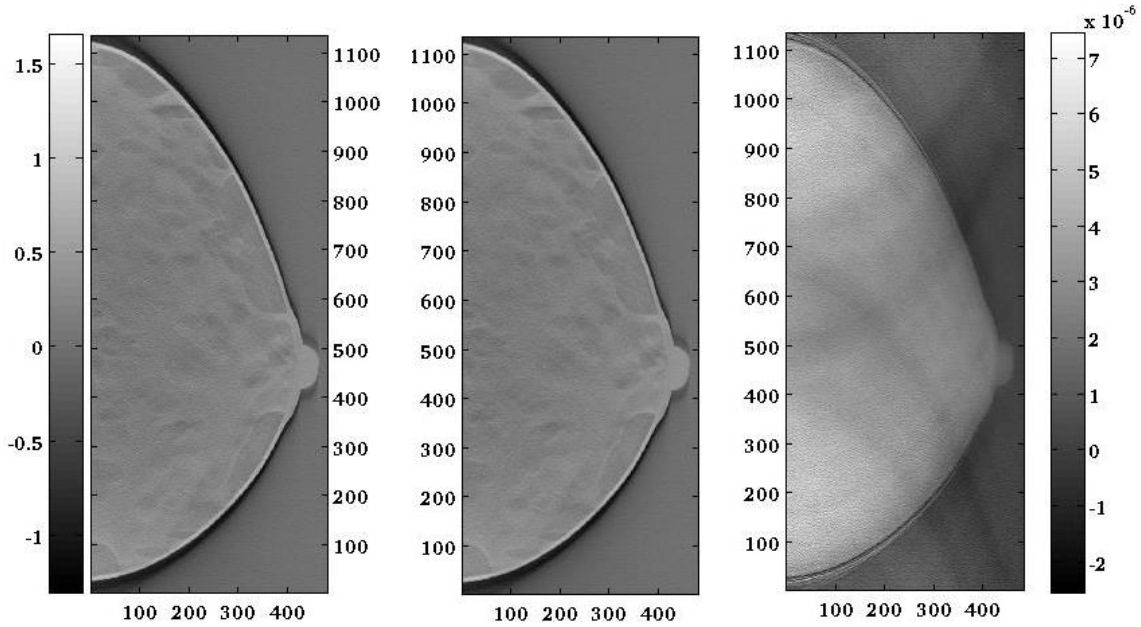

Figure 4.3: (a) Reconstructed using single threaded C with pixel values (attenuation density) ranging between -1.3 and 1.66 cm^{-1} (b) Reconstructed using MATLAB with pixel values ranging between -1.3 and 1.66 cm^{-1} and (c) Difference between MATLAB and C with pixel values ranging from -3×10^{-6} to 7×10^{-6} cm^{-1}.

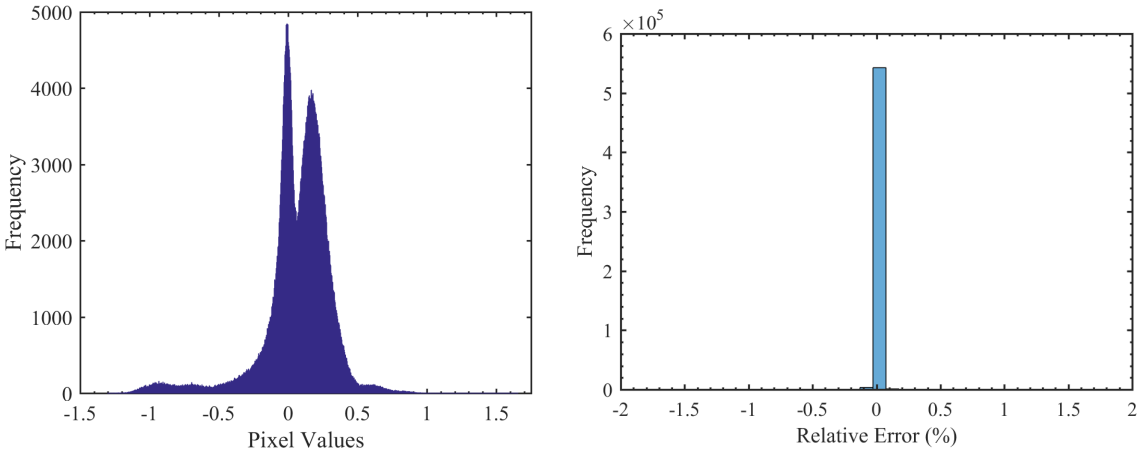

Figure 4.4: (a) Histogram of Pixel Values from C reconstruction and (b) Relative Error in percentage between MATLAB and C.

rected FBP reconstruction code for CBCT is available open source through GitHub (*VICTRE Github Repository*, 2018).

CHAPTER V

An in Silico Study to Evaluate the Effect of X Ray Detector Technology on Breast Cancer Detection

5.1 Abstract

The purpose of this work is to integrate computational models of different detector technologies with the VICTRE in silico pipeline for breast imaging to evaluate the effect of detector technology on breast cancer detection. This study would allow us to gain insight into the relationship between image quality metrics and the clinical performance that can be achieved with different detector technologies. We developed three detector models with varying image quality metrics. The DIR and DIR+ models replicate direct a-Se performance, while IND is based on indirect CsI technology. The same DM/DBT system geometry and x-ray acquisition parameters, modeled to mimic the Siemens Mammomat Inspiration system, were used to evaluate the three detectors. The VICTRE pipeline was used to simulate in silico patient with disease in form of spiculated masses or micro-calcifications, generate DM/DBT images of the patients with the three detector models and finally interpret them using 2D/3D reader models. We analyzed the area under the ROC curves (AUC) for both imaging modalities and manifestations of breast cancer to characterize the clinical performance of the detectors. We found that the detector technology did not affect the detection of

spiculated masses. On the other hand, for micro-calcifications, we noticed a significant increase in the AUC for DM for the IND detector: 0.95 versus 0.92 and 0.9 with the DIR and DIR+ detectors. For DBT, the DIR detector exhibited the best performance. Overall, the AUC differences revealed that while there were benefits of using DBT with the DIR detector, DM outperformed DBT for the DIR+ and IND detectors. The detector technologies for the studied system parameters significantly affect the detection of micro-calcifications and the benefits of using DBT.

5.2 Introduction

X-ray detectors are an integral part of digital mammography (DM) and breast tomosynthesis (DBT) systems. In general, the objective of DM/DBT systems is to generate high resolution and low noise images that enhance the visibility of finer details and low contrast masses for cancer detection. In terms of detector performance, this translates to a high modulation transfer function (MTF), low noise power spectrum (NPS) and consequently a high detective quantum efficiency (DQE). While these metrics can be used to predict DM clinical performance, compare imaging capabilities of different detector technologies, they are not complete indicators of 3D DBT image quality.

There are four commercially available DM/DBT systems including General Electric, Hologic, Siemens and Fujifilm that have received FDA clearance. While large clinical trials have attempted to provide insight on the clinical performance of the various systems, the main goal of these studies was to compare the imaging modalities (*Lee and McCaskill-Stevens*, 2020; *Keavey et al.*, 2012). Moreover, these studies compare system performance which is a combination of detector technology, system geometry, x-ray acquisition techniques and image processing algorithms. To study the effect of detector technology alone on cancer detection rates via clinical trials would require extensive device fabrication and integration with a commercial DM/DBT sys-

tem. Clinical trials are also expensive and time consuming and require institutional review board (IRB) approvals for handling patient data. A faster and cost-effective approach would be to conduct these studies in silico (*Badano et al.*, 2018; *Bakic et al.*, 2018; *Warren et al.*, 2012; *Mackenzie et al.*, 2015).

Hybrid studies, i.e., studies that rely on a combination of clinical and in silico data, have been developed that evaluate different detectors for detection of breast cancer, in the form of spiculated masses and calcifications (micro-calcifications) (*Mackenzie et al.*, 2015; *Warren et al.*, 2012) using DM. However, these studies used DM images from real patients, which were then post-processed to reflect the noise and resolution properties of the different detectors evaluated in the articles. In contrast to previous hybrid approaches, in this work, we propose a completely in silico approach for evaluating the clinical performances of x-ray detectors for DM and DBT modalities. We integrated computational models of different detector technologies with the VICTRE in silico pipeline (*Sharma et al.*, 2019) for breast imaging to evaluate the the effect of detector technology on breast cancer detection. A schematic representation of the modified VICTRE pipeline is depicted in Fig. 5.1.

We evaluated the performance of three x-ray detector models: DIR, DIR+ and IND. The DIR and DIR+ are based on amorphous selenium (a-Se) direct detector technology, while the IND replicates the performance of cesium iodide indirect detectors. The DIR system models an ideal a-Se detector, whereas the DIR+ system also includes inter-pixel crosstalk resulting in poorer resolution properties as compared to DIR. To focus on the effects of detector technology alone, we used the same DM/DBT system geometry, x-ray acquisition parameters and reconstruction algorithm determined by the Siemens Mammomat Inspiration system, to evaluate the three detector models.

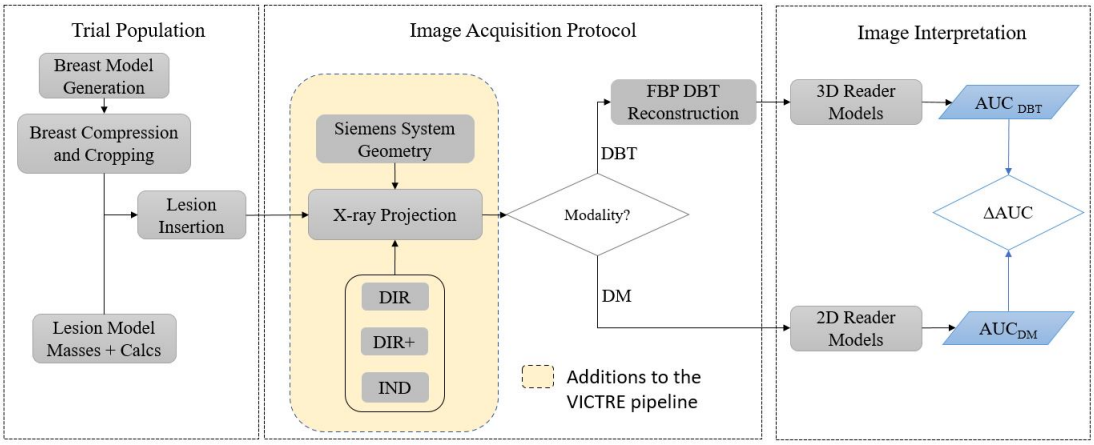

Figure 5.1: Schematic description of the modifications to the VICTRE pipeline to evaluate the effect of detector technology on breast cancer detection.

5.3 Methods

Many of the methods used in this work are from the VICTRE pipeline (*VICTRE Github Repository*, 2018). First, this study uses the same trial population used for the VICTRE trial (*Badano et al.*, 2018). The population consists of compressed breast models based on algorithms developed by Graff et al. (*Graff*, 2016), of varying breast densities. These models, generated at a resolution of 50 μm, include anatomical features such as vasculature, ductal network and a realistic breast shape in addition to adipose and glandular tissues. A total of 2986 breast models were created and categorized as extremely dense, heterogeneously dense, scattered fibroglandular densities and almost entirely fat. Disease was simulated either as a 5 mm spiculated mass (*de Sisternes et al.*, 2015) or a cluster of 5 microcalcifications.

The VICTRE study investigated the performance of one direct a-Se detector as part of the SIEMENS DBT system. In this work, we extend the analysis to three detector technologies. Three of the detectors are based on a 200 μm a-Se direct detector technology, while the fourth models a 250 μm indirect CsI detector.

Trial population	Dense	Hetero	Scattered	Fatty
DIR and DIR+ Detectors				
All Patients	286	1200	1200	300
Patients with disease	189	780	780	195
DM Cases with lesion	1499	6237	6232	1559
Normal DM Cases	1260	5035	5032	1248
DBT Cases with lesion	1499	6237	6232	1559
Normal DBT cases	1243	4968	5006	1235
IND Detector				
All patients	286	300	300	300
Patients with disease	189	195	195	195
DM Cases with lesion	1456	1557	1560	1559
Normal DM cases	1176	1264	1260	1236
DBT Cases with lesion	1451	1557	1560	1559
Normal DBT cases	1149	1275	1243	1234
Glandularity (volume fraction)	0.548	0.339	0.143	0.071
Volume (cm^3)	111.5	218.0	441.2	685.6
Compressed thickness (cm)	3.49	4.49	5.50	5.99

Table 5.1: Characteristics of the trial population used in this study. Please note: more cases for the IND will be included later due to the low computational efficiency of the model.

5.3.1 Detector models

All our models were developed using MCGPU codes (*Badal et al.*, 2020a). In each simulation, a large number of x-ray photons are generated and tracked in terms of energy and direction, from the source, through the breast model and into the detector. Inside the detector, x-ray photons are tracked till first photoelectric interaction. The model takes fluorescence effects into account by generating and tracking a secondary x-ray based on the fluorescence yield in a uniformly random direction. The simulation tallies the total energy deposited in each detector pixel and calculates the number of electron-hole pairs generated with an effective ionization energy of 50 eV. Finally, to add electronic noise with an RMS value of 5200 electrons added to the standard deviation of pixel level.

The DIR+ model is similar to DIR but includes additional blurring due to inter-

pixel crosstalk. We assume that when a single pixel is illuminated, the signal (76%) is mainly located in the incident pixel and the neighboring 8 pixels share a small fraction of the total signal. So, instead of tallying the entire x-ray photon energy in a single pixel, a small fraction of it is spread to its neighboring pixels to reproduce the detector crosstalk.

The IND x-ray detector model is based on a thallium-doped cesium iodide (CsI:Tl) scintillator that converts incident x-ray energy to charge in a two-step process. The CsI:Tl layer first absorbs the incident x-ray energy and converts it into optical photons. Depending on the depth at which the optical photons are generated, we introduce an additional spread of the signal approximated using a Lorentzian depth-dependent optical spread (O^z) function, as shown previously by Freed et al. (*Freed et al.*, 2010). The optical spread is implemented using a pre-computed set of the (O^z) functions at various detector depths. Based on the depth of interaction, the corresponding (O^z) function is selected and applied to determine the distribution of the x-ray energy in the neighboring detector pixels.

5.3.2 System parameters

The detector models were evaluated using the same system geometry and x-ray acquisition parameters modeled to replicate the Siemens Mammomat Inspiration DM and DBT system. We used a pixel pitch of 85 μm, an angular range of 50° with 25 projection views and electronic noise RMS of 5200 electrons. The dosimetric and x-ray acquisition parameters were selected based on publicly available device specifications and clinical recommendations for each compressed breast thickness and glandularity. The focal spot blurring in the source was modeled as 3D Gaussian probability distribution with a full-width-at-half-maximum of 300 μm. A tungsten anode filtered with 50-μm rhodium was used with a peak voltage of 28 kV for fatty and scattered breasts and 30 kV for dense and heterogeneously dense breasts. The

same analytical antiscatter grid was also included for generating the DM images. (5:1 ratio, 31 line pairs/mm) (*Badal et al.*, 2020a). Finally, a filtered backprojection algorithm (*Sengupta et al.*, 2018) was used to generate the DBT volumes (*Badano et al.*, 2018).

5.3.3 Statistical analysis and trial outcomes

ROIs (regions of interest) and VOIs (volumes of interest), extracted from the simulated DM/DBT images were interpreted with a computational reader model. These in silico readers perform a location-known-exactly detection task based on a channelized Hotelling observer. Thirty computational readers were used to interpret the ROIs/VOIs with or without a lesion(*Zeng et al.*, 2020). To characterize the imaging performance of the detectors, the area under the ROC curves (AUC) for both imaging modalities and manifestations of breast cancer were analyzed for each density class. The difference in AUCs between the DBT and DM modes were also calculated to ascertain any potential improvements in cancer detection that can be achieved using DBT.

5.4 Results

Fig. 5.2 (a) illustrates image quality metrics (MTF, NNPS and DQE) for three detectors evaluated in this study. As expected, the DIR and DIR+ models based on amorphous selenium technology exhibit better spatial resolution properties as compared to IND. Since all three detectors were modeled with the same pixel size of 85 μm, the variations in the MTF curves is a result of the detector properties and not due to pixel size. The NNPS and DQE curves for the direct and indirect systems were simulated at exposure levels of 188 μGy and 177 μGy respectively.

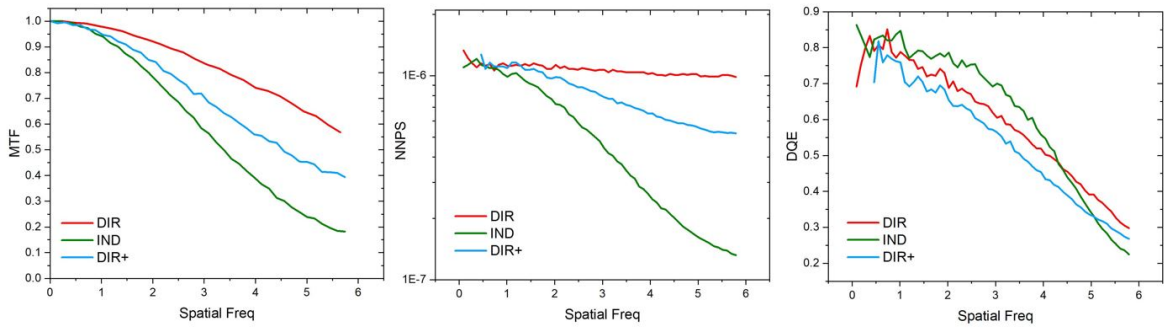

Figure 5.2: Image quality metrics (MTF, NNPS and DQE) for the three systems that were evaluated as part of this study.

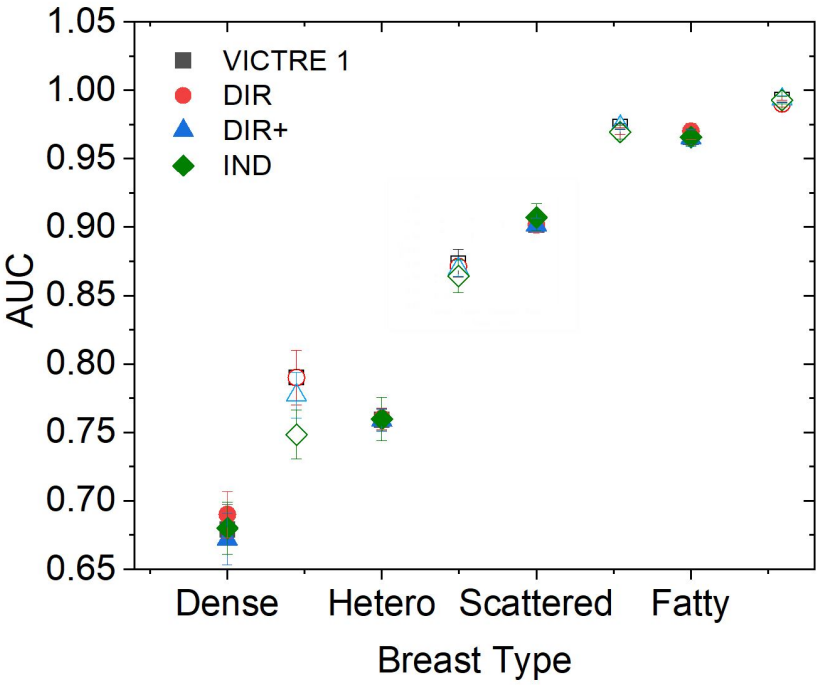

(a)

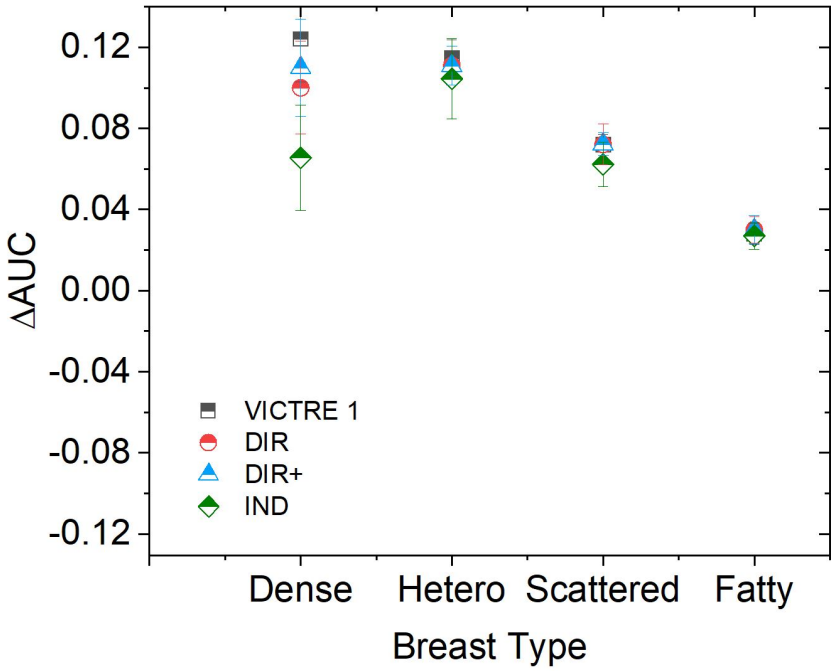

(b)

Figure 5.3: (a) AUC values, calculated using the imrmc software (*B. D. Gallas, IMRMC software*, 2013), evaluating the detection of masses, calculated for the DIR, DIR+ and IND systems. The solid symbols represent DM while the open ones represent DBT. The difference AUCs ($AUC_{DBT} - AUC_{DM}$) are plotted in (b). Please note that the reported values for errors are estimates and will be updated in the final version.

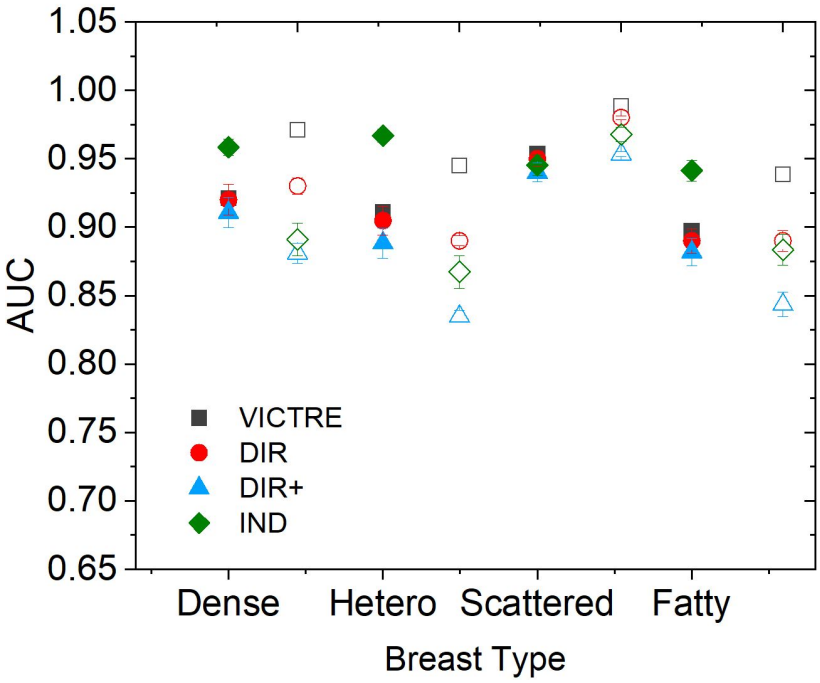

(a)

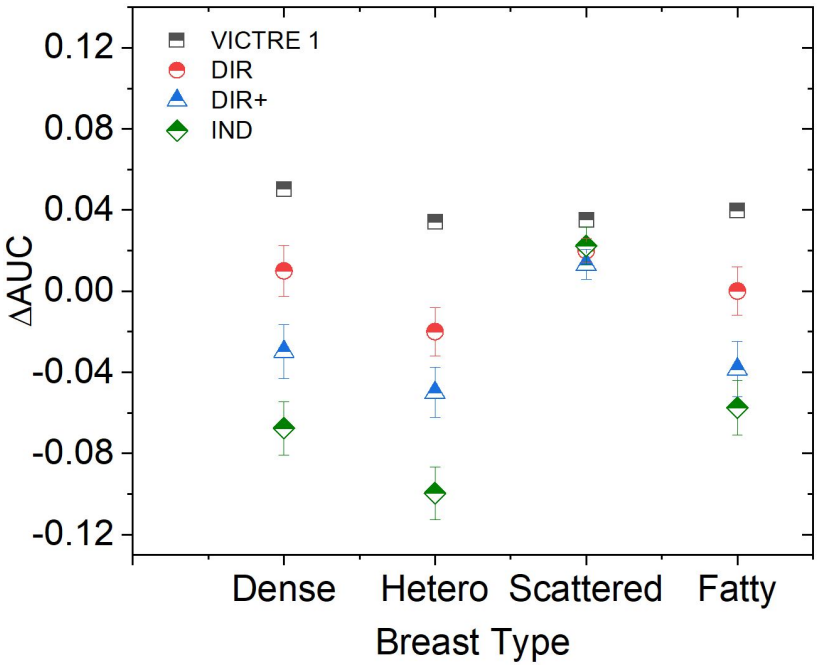

(b)

Figure 5.4: (a) AUC values, calculated using the imrmc software (*B. D. Gallas, IMRMC software*, 2013), evaluating the detection of micro-calcifications, calculated for the DIR, DIR+ and IND systems. The solid symbols represent DM while the open ones represent DBT. The difference AUCs ($AUC_{DBT} - AUC_{DM}$) are plotted in (b). Please note that the reported values for errors are estimates and will be updated in the final version.

Fig. 5.3(a) shows AUC values evaluating the detection of spiculated masses, calculated for the DIR, DIR+ and IND systems. For comparison, the AUC values calculated as part of the VICTRE trial have also been included. The mean AUC values shown in table 5.2 suggest that the detector technology has minimal effect on the detection of spiculated masses. The difference in the AUCs for the two modalities indicate that detection of masses favours DBT irrespective of detector technology.

Fig. 5.4 (a) shows AUC values evaluating the detection of micro-calcifications, calculated for the DIR, DIR+ and IND systems. For comparison, the AUC values calculated as part of the VICTRE trial have also been included. Please note that the AUC values reported for the VICTRE trial (*Badano et al.*, 2018) are slightly different from the ones plotted in figure 5.2 a result of larger ROI sizes that are being used for analyzing micro-calcifications as part of the reader algorithm. As shown in fig 5.4, the direct detector technology (DIR and DIR+) does not significantly affect the AUCs in DM, while a significant drop in AUCs is observed especially in the DBT mode: on average, across all classes, AUC reduced from 0.93 to 0.88 for the DIR and DIR+ systems, respectively (see table 5.2). For the DIR system, the DM and DBT modes perform equivalently for with an average AUC difference of 0.001. For the DIR+ system, the average AUC difference value of -0.02 marginally favors DM for the detection of micro-calcifications. On the other hand, a significant increase in AUCs in DM is observed for the IND detector compared to the direct detectors: 0.96 versus 0.92 and 0.91. On average, an AUC difference value of -0.05 is observed, favoring DM.

For the simulations with direct DIR/DIR+ detector models, generating a complete set of DM and 25 DBT projections took 11 and 64 min on average for the dense and fatty classes respectively. The IND model was slower as compared to the DIR and DIR+ models due to the additional steps to simulate the spread of optical photons in indirect CsI based detectors. For IND detector models, corresponding simulation

Type	DIR	DIR+	IND
	Spiculated masses		
AUC_{DM}	0.83 (0.01)	0.83 (0.01)	0.83 (0.01)
AUC_{DBT}	0.91 (0.005)	0.91 (0.01)	0.89 (0.01)
ΔAUC	0.08 (0.01)	0.09 (0.01)	0.07 (0.02)
	Micro-calcification clusters		
AUC_{DM}	0.92 (0.01)	0.91 (0.01)	0.96 (0.01)
AUC_{DBT}	0.93 (0.003)	0.88 (0.003)	0.90 (0.01)
ΔAUC	0.001 (0.01)	-0.02 (0.01)	-0.05 (0.01)

Table 5.2: Average AUCs(SE) for DM and DBT modes, calculated using the imrmc software (*B. D. Gallas, IMRMC software*, 2013), for detection of spiculated masses and micro calcifications. Please note that the reported values for errors are estimates and will be updated in the final version.

times increased to 247 and 669 min for the dense and fatty classes respectively. The projections were executed with on a system with 4996 CPU cores and 32 Tesla V100-PCIE GPU nodes with 32 GB RAM.

5.5 Discussion

In general, we found that detector technology has no significant impact on the detection of spiculated masses (see table 5.2). However, for micro-calcifications, the AUC differences (see table 5.2 and fig. 5.4) show significant variation indicating that the benefit of DBT depends on the detector technology. For detecting micro-calcifications, we observed that the DIR detector exhibits improved performance in DBT, with positive AUC differences for three of the four breast density classes. However, we found that DM outperformed DBT for the DIR+ and IND detectors. As compared to the DIR detector, the DIR+ detector suffered degradation in DM, but more significantly so in DBT, resulting in negative AUC differences. This could be a consequence of the lower DQE exhibited by the DIR+ system. On the other hand, a significant increase in the AUCs for DM was observed for the IND detector as compared to the DIR+ detector, most likely due to the higher DQE performance in spite

of the reduced spatial resolution. Overall, the IND detector performed better in DM.

5.6 Conclusion

Our findings provide insight into the effects of detector technology on breast cancer detection. By performing this study in silico, we were able to remove all other confounding and contributing factors including system geometry, x-ray acquisition parameters and image processing algorithms. We found that the detector technology has an effect on the detection for larger low-contrast targets like masses. On the other hand, for micro-calcifications, significant variations in detectability across detectors was observed. The IND and DIR detectors exhibited improved performance for DM and DBT respectively. While DBT may be the preferred modality for detecting spiculated masses, its benefits for micro-calcifications appear to depend on the detector technology.

CHAPTER VI

The First Longitudinal in Silico Imaging Trial for Early Detection of Breast Cancer

6.1 Abstract

Breast cancer screening programs aim at detecting cancer at earlier stages and have been instrumental in reducing mortality rates across North America. Digital breast tomosynthesis (DBT), an imaging technology that relies on the acquisition of several angular projections is being considered as a replacement for digital mammography (DM), the current gold standard for screening. Although the advantage of DBT for the detection of larger masses (nominal diameter > 1 cm) has been demonstrated through various studies, it remains to be seen if DBT offers similar benefits at earlier stages of cancer progression, when tumor sizes are smaller. The TMIST trial is currently seeking to address a similar question: can DBT outperform DM in reducing advanced breast cancer development? However, since this study involves enrolling hundreds of thousands of women across several sites all over the world, it is expected to be a slow and expensive process. We propose to conduct our experiments in silico as a faster and cost-effective alternative. We describe the first ever in silico longitudinal trial (L Trial) reported in literature. To mimic cancer progression, we developed a computational model for simulating the growth of breast cancer lesions

based on biological and physiological phenomena accounting for the stiffness of surrounding anatomical structures for realizing a range of lesion morphology. This model was integrated with the VICTRE pipeline to create a cohort of in silico patients each with an unique manifestation of cancer recorded at 5 stages of progression. Digital patients with varying breast densities, from dense to fatty were considered. The VICTRE pipeline was used to simulate DM and DBT imaging of the patients with an in silico version of the Siemens Mammomat Inspiration system with image interpretation relying on using 2D/3D algorithmic readers previously described. We analyzed the area under the ROC curve (AUC) for both imaging modalities at the 5 stages of cancer growth to evaluate the performance of DBT and DM along the life of the tumor. The findings suggest that that DBT outperforms DM for all lesion sizes, which is consistent with studies reported in literature. We observed the mean AUCs grow from 0.64 to 0.8 for DM and from 0.66 to 0.88 for DBT as the lesion sizes increased from 0.37 to 1.8 mm. These results demonstrate the benefits of DBT as compared to DM for detection of smaller masses at earlier stages of tumor development.

6.2 Introduction

Breast cancer remains to be the leading cause of cancer deaths amongst women worldwide. However, when breast cancer is detected and treated early, the chances of survival are very high. Two strategies identified by the world health organization (WHO)(*Ginsburg et al.*, 2020) to promote the early detection of cancer include early diagnosis, which is the recognition of symptomatic cancer at an early stage, and screening, which is the identification of asymptomatic disease in a target population of apparently healthy individuals. Two dimensional (2D) digital mammography (DM) is currently the gold standard for imaging techniques used in screening programs. However, since it is a 2D imaging modality, large amounts of overlapping fibroglandular tissues, especially in dense breasts can hide or mimic the presence of cancerous

lesions leading to false negatives and false positives. Digital breast tomosynthesis (DBT) generates three dimensional information of the breast by acquiring several projection images for a range of projection angles(*III*, 2009). Previous clinical studies have demonstrated the advantages of DBT as compared to DM for the detection of larger masses (*McDonald et al.*, 2016; *Asbeutah et al.*, 2019; *Iranmakani et al.*, 2020) and reduction of recall rates (*McDonald et al.*, 2016; *Iranmakani et al.*, 2020). For screening programs, it has been shown that although the overall rate of screening-detected cancers was similar with DM and DBT, a higher proportion of invasive versus in situ cancers was detected with DBT. In addition, it has also been hypothesized that DBT screening could result in earlier detection of cancer. However, it has not yet been established if the use of DBT in screening programs can lead to finding cancers in earlier stages.

The National Cancer Institute–funded Tomosynthesis Mammographic Imaging Screening Trial (TMIST) aims at addressing these concerns. The main outcome of the TMIST trial is to ascertain whether the use of DBT can enable radiologists to find aggressive cancers at earlier stages, as compared to DM. However, this study involves enrolling hundreds of thousands of women and is not expected to report its findings anytime in the near future. In this work, we study the benefits of DBT at earlier stages of tumor growth, a limited version of TMIST, but using a fast and cost-effective approach that does not involve radiating asymptomatic women, by conducting these experiments in silico.

In the past, in silico trial approaches have been used to evaluate the performance of DM for detection of breast cancer, in the form of spiculated masses and calcifications (calcs)(*Mackenzie et al.*, 2015; *Warren et al.*, 2012). However, these studies were not completely in silico as they used DM images from real patients, which were then post-processed to reflect the noise and resolution properties of the different detectors evaluated in the articles. Some simulation frameworks(*Badano et al.*, 2018; *Bakic*

et al., 2018) have also been extended to include DBT as well with the goal to compare the performance of DBT and DM in detecting masses and calcifications. However, to the best of our knowledge, there has been no report of an longitudinal in silico study that evaluates and tracks the performance of DM and DBT through the lifetime of a cancerous lesion for a cohort of diseased patients. The findings of such a trial might contribute to the demonstration of any benefits DBT might have over DM for earlier detection of lesions. In this work, we describe the first ever in silico longitudinal trial (L Trial) reported in literature. We modeled the progression of breast cancer using a previously developed computational model(*Sengupta et al.*, 2021; *Sengupta and Badano*, 2021) for simulating the growth of breast cancer lesions based on biological and physiological phenomena accounting for the stiffness of surrounding anatomical structure. We integrated this model with the VICTRE pipeline(*Sharma et al.*, 2019) to create and image a cohort of in silico patients with and without disease. The disease patients were imaged at 5 growth time points. The simulated DM/DBT images were interpreted using 2D/3D model observers described by our group previously. A schematic representation of the modified VICTRE pipeline is shown in Fig. 6.1.

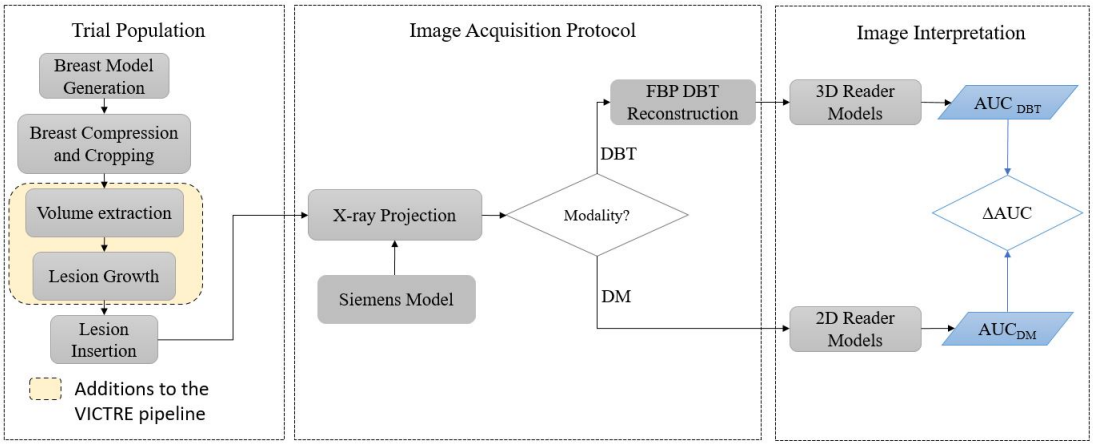

Figure 6.1: Schematic description of the modifications to the VICTRE pipeline to evaluate the effect of detector technology on breast cancer detection.

6.3 Methods

6.3.1 In silico patient population

The patient population used for the VICTRE trial (*Badano et al.*, 2018) was recycled for this study. The VICTRE population consisted of breast models developed by Graff et al. (*Graff*, 2016), of varying breast densities. These models, generated at a resolution of 50 μm include anatomical features such as vasculature, ductal network and a realistic breast shape in addition to the adipose and glandular tissues. A total of 1156 breast models were created, categorized as extremely dense (dense), heterogeneously dense (hetero), scattered fibroglandular densities (scattered) and almost entirely fat (fatty). A finite-element solid mechanics software(*Maas et al.*, 2012) was used to simulate breast compression in craniocaudal orientation. Table 6.1 shows characteristics of the virtual population used for this study.

Virtual Patients	**Dense**	**Hetero**	**Scattered**	**Fatty**
All Patients	289	969	969	289
Patients with Disease	189	189	189	189
DM Cases with lesion	747	635	699	728
Normal DM Cases	618	2497	2512	618
DBT Cases with lesion	747	635	702	728
Normal DBT Cases	618	2468	2496	617
Glandular Volume Fraction	0.548	0.339	0.143	0.071
Volume (cm^3)	111.5	218.0	441.2	685.6
Compressed Thickness	3.49	4.49	5.50	5.99

Table 6.1: Characteristics of the trial population used in the study.

Model of disease progression

To grow the lesions, 1cm x 1cm x 1cm volumes were first extracted from the breast models. The growth locations were randomly chosen from a list of possibilities governed by the position of the terminal duct lobular units, a common site for carcinogenesis. Care was taken to ensure that these volumes were located within the

breast boundary and had no overlap with air, muscle, nipple or skin.

A MATLAB based lesion growth algorithm(*Sengupta et al.*, 2021; *Sengupta and Badano*, 2021) was used to simulate tumor growth within each of the extracted volumes. The growth dynamics that govern this model take into account the interstitial tumor pressure, concentration of metabolites such as oxygen and carbon-dioxide as well as the stiffness of the of the local tissues. In the model, tumor cells are less likely to grow through stiffer structures like ligaments and instead preferentially proliferate in the more elastic regions of the breast. Depending on the breast local anatomical structures, a range of lesion morphology were achieved. This model was used to generate lesion morphology at 5 growth time points, with an average radius varying from 0.32 to 1.8 mm. Lesions at each stage of growth were then inserted into the corresponding breast locations. For computational efficiency, 4 lesions were grown and inserted in approximately half of the virtual patients.

6.3.2 Imaging protocol

Similar to the VICTRE study, an in silico version of the Siemens Mammomat Inspirations system was used to generate the DM/DBT images. The amorphous selenium (a-Se) based x-ray detector was modeled using MCGPU codes(*Badal et al.*, 2020a) based on Monte Carlo (MC) x-ray transport simulations, adapted from PENELOPE 2006(*Salvat et al.*, 2006). In each simulation, a large number of x-ray photons were generated and tracked in terms of energy and direction, from the source, through the breast model, and to the detector. Inside the detector, x-ray photons are tracked till first photoelectric interaction. The model takes fluorescence effects into account by generating and tracking a new x-ray depending on the fluorescence yield probability, in a uniformly random direction. The simulation tallies the total energy deposited in each detector pixel, which is used to sample the number of electron-hole pairs from a Gaussian distribution, with a mean value indicating the charge generated with an

effective ionization energy of 50 eV and standard deviation represented by the Swank factor. Finally, to replicate the presence of electronic noise, which is described as a RMS value, 5200 was added to the standard deviation of each pixel value.

The dosimetric and x-ray acquisition parameters were selected based on publicly available device specifications and clinical recommendations for each compressed breast thickness and glandularity. The focal spot blurring in the source was modeled as 3D Gaussian probability distribution with a full-width-at-half-maximum of 300 μm. A tungsten anode filtered with 50-μm rhodium was used with a peak voltage of 28 kV for fatty and scattered breasts and 30 kV for dense and hetero breasts. An analytical antiscatter grid was also included for generating the DM images. (5:1 ratio, 31 line pairs/mm)(*Badal et al.*, 2020a). Please see the original VICTRE publication(*Badano et al.*, 2018) for further details.

6.3.3 Image interpretation

ROIs (regions of interest) and VOIs (volumes of interest), extracted from the simulated DM/DBT images were interpreted with a computational reader model. These in silico readers were modeled to perform a location-known-exactly detection task based on a channelized Hotelling observer (cho). This observer used 5 Laguerre-Gauss channels with widths calibrated to lesion size (*Zeng et al.*, 2015). Since this study evaluated lesions at different growth time points, the channel sizes were varied in proportion to the average size of the lesions at each stage. In the VICTRE trial, channel widths of 30 and 25 pixels were used in the DM and DBT modes respectively to detect a lesion with a nominal radius of 2.5 mm. The channel widths varied from 4 to 22 pixels in proportion to the lesion radius, which increased from 0.32 to 1.8 mm. The same channel widths were used for both imaging modalities. Thirty computational readers were used to interpret the ROIs/VOIs with or without a lesion. For each density group, 30 computational readers were trained with different sets of

100 pairs of cases randomly sampled from a larger set of training pairs. For further details please refer to the original VICTRE publications(*Badano et al.*, 2018).

6.3.4 Trial outcomes and statistical analysis

To evaluate the performance of DBT and DM at earlier stages of tumor growth, the area under the ROC curves (AUC) for both imaging modalities at the 5 time points of cancer growth, were analyzed for each density class. The difference in AUCs between the DBT and DM modes were also calculated to ascertain any potential improvements in cancer detection that can be achieved using DBT.

6.4 Results

A total of 9121 DM and 9011 DBT cases, generated using 2516 in silico patients were interpreted by the model observers across the 4 density classes studied. As expected in a traditional clinical trial, each DM and DBT case with disease presented a lesion morphology unique to its anatomical background. Fig. 6.2 illustrates sets of ROIs from DM (left) and DBT (right) images for different masses at 4 growth time points. Each row in fig. 6.2 represents the progression of the lesion for a different density class. We found that for the dense and hetero classes, the growth was more likely to be anisotropic due to larger variation in the tissue types. The growth was a lot more isotropic for the fatty and scattered fibroglandular classes due to the large pockets of adipose tissue.

Fig. 6.3 illustrate the variations in the DM and DBT AUCs as well as their differences across the four breast density classes. The L trial curves represent the results from the experiments performed as part of this study. For comparison, we have included data from the VICTRE trial (*Badano et al.*, 2018), which included a single 2.5 mm radius mass for all DM and DBT cases with disease. Overall, for the largest mass (radius 1.8 mm) we observed a mean AUC of 0.8 for DM and 0.88 for DBT.

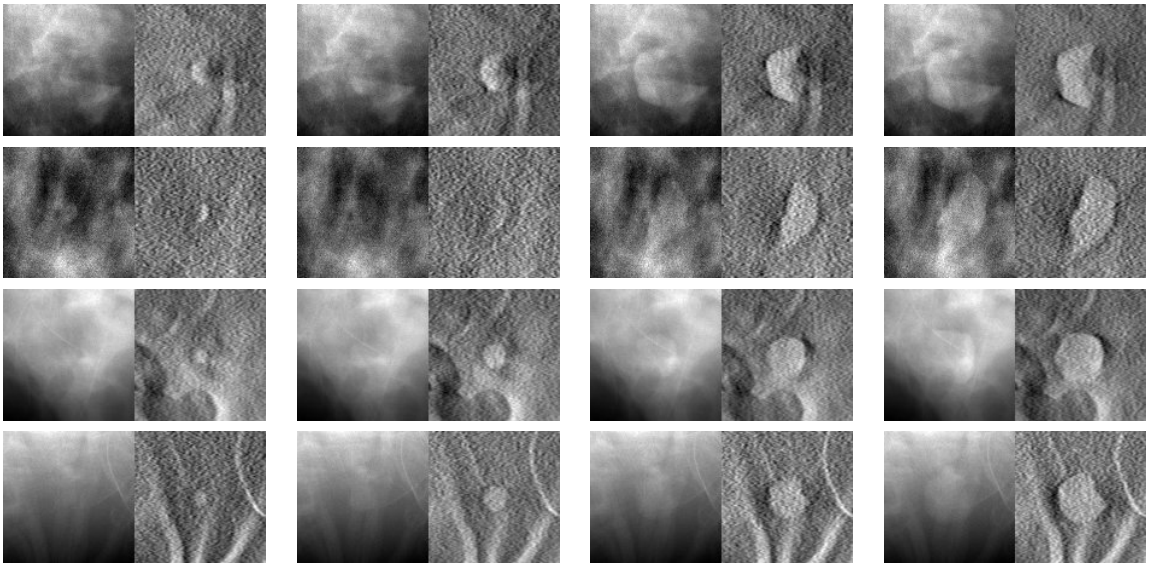

(a) (b) (c) (d)

Figure 6.2: Sets of DM (left) and (DBT) ROIs showing lesions at four growth time points with average radii of (a) 0.57 (b) 0.95, (c) 1.5 and (d) 1.8 mm. Each row corresponds to masses grown in breast models from different density classes. The density varies from dense (top row) to fatty (bottom row). Note that these ROIs were generated by simulating the lesions to be 1.5 times denser than glandular tissues for better visualization.

For the 0.95 mm and 0.32 mm masses, the mean AUCs for DM dropped to 0.76 and 0.64, while for DBT, the mean AUCs were 0.84 and 0.64 respectively. The AUC difference plots (see fig. 6.4) for the dense and hetero classes show a monotonic rise with lesion size, but a similar trend is not observed for the two other classes. This could be a result of the higher AUCs observed in general for the dense and hetero classes, which leave little room for the mean AUC for DBT to grow. However, in general we observe that masses greater than those with a radius of 0.57 mm favor DBT, while DM and DBT perform equivalently for the smallest mass of radius 0.32 mm. The smallest mass in the fatty class (see fig. 6.4) is the only category where DM marginally outperforms DBT.

We observe that the AUCs approach the numbers reported for the VICTRE trial for a 2.5 mm mass. The slightly lower numbers that we observe for largest mass (1.8

Lesion Size(mm)	**Dense**	**Hetero**	**Scattered**	**Fatty**	**Total**
			AUC_{DM}(SE)		
0.32	0.53(0.02)	0.59(0.01)	0.68(0.01)	0.75(0.02)	0.64 (0.02)
0.95	0.61(0.02)	0.7(0.01)	0.81(0.01)	0.91(0.01)	0.76 (0.01)
1.8	0.63(0.02)	0.74(0.01)	0.85(0.01)	0.93(0.01)	0.8 (0.01)
			AUC_{DBT}(SE)		
0.32	0.54(0.01)	0.61(0.01)	0.67(0.01)	0.75(0.02)	0.64 (0.01)
0.95	0.68(0.02)	0.79(0.01)	0.92(0.01)	0.97(0.01)	0.84 (0.01)
1.8	0.75(0.02)	0.84(0.01)	0.94(0.01)	0.99(0.003)	0.88 (0.01)
			ΔAUC (SE)		
0.32	0.01(0.02)	0.02(0.02)	-0.01(0.02)	0(0.02)	0.01 (0.02)
0.95	0.07(0.02)	0.09(0.01)	0.1(0.01)	0.06(0.01)	0.08 (0.02)
1.8	0.11(0.02)	0.09(0.01)	0.09(0.01)	0.05(0.01)	0.09 (0.01)

Table 6.2: Mean AUCs (SE), calculated using the imrmc software (*B. D. Gallas, IMRMC software*, 2013), for the DM and DBT modes observed across the four density classes.

mm radius) studied in this work could be due to a combined effect of the smaller size and varying lesion morphology, that results in the formation of a less defined mean signal, used to train the model observers.

The average processing times for each step and density class are shown in Table 6.3. Please note that the time required for the lesion growth step includes saving the lesion morphology at five growth time points. On the other hand, the timings for the projection and reconstruction steps have been recorded for a single breast model which contains four lesions at different locations at the same stage of growth. In other words, for each case, the projection and reconstruction steps were executed five times to account for the various stages of growth. As shown in Table 6.3, the time required to project and reconstruct increases as we move towards the almost entire fat class, consists of the largest breast models. The time required to grow the lesions, however, does not exhibit much variation across the density classes.

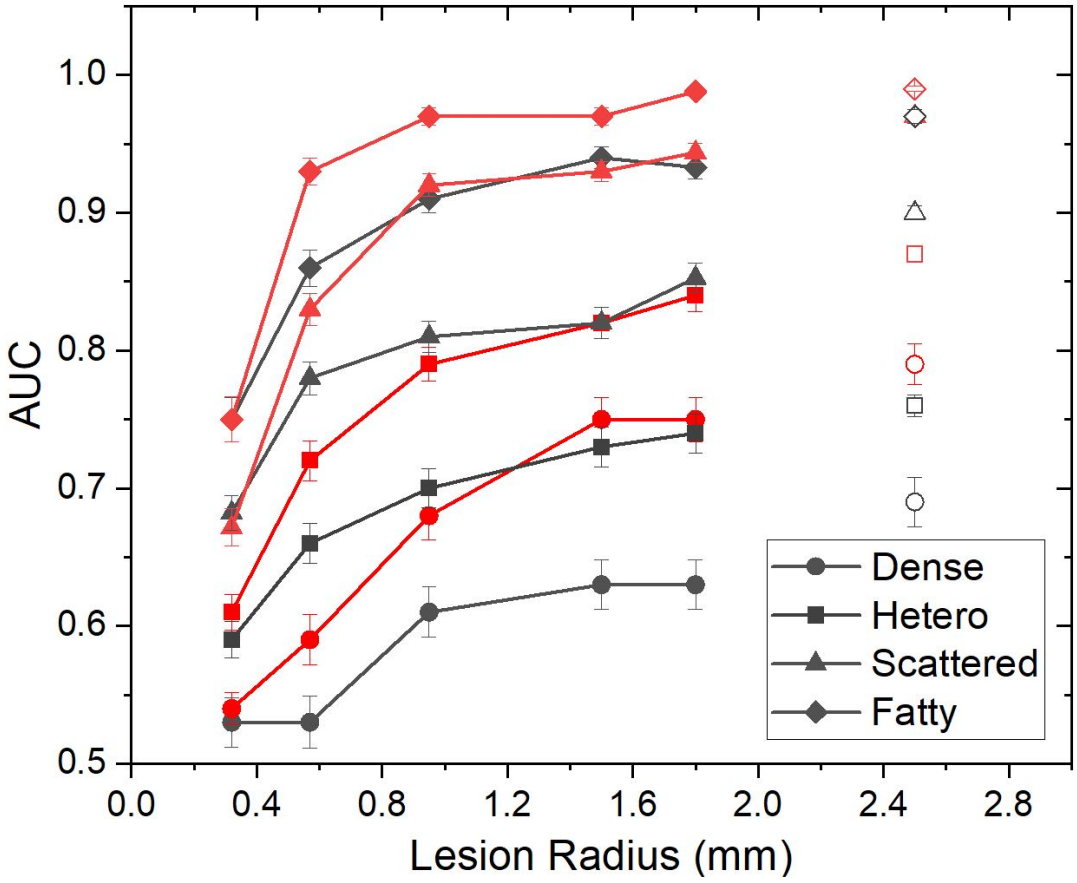

Figure 6.3: Variations in AUCs, calculated using the imrmc software (*B. D. Gallas, IMRMC software*, 2013), for DM (black) and DBT (red) across the four density classes: dense (circle), hetero (square), scattered (triangle) and fatty (diamond). The data from the VICTRE trial are also included for the four classes. The VICTRE data are the open symbols, while the solid symbols represent the L trial data.

Processing Step	**Dense**	**Hetero**	**Scattered**	**Fatty**
Lesion Growth	98	87	97	83
Projection	8	14	18	22
Reconstruction	13	19	28	37

Table 6.3: Average timings (in minutes) for the different processing steps for running a single case from each density category. The various steps were executed with on a system with 4996 CPU cores and 32 Tesla V100-PCIE GPU nodes with 32 GB RAM.

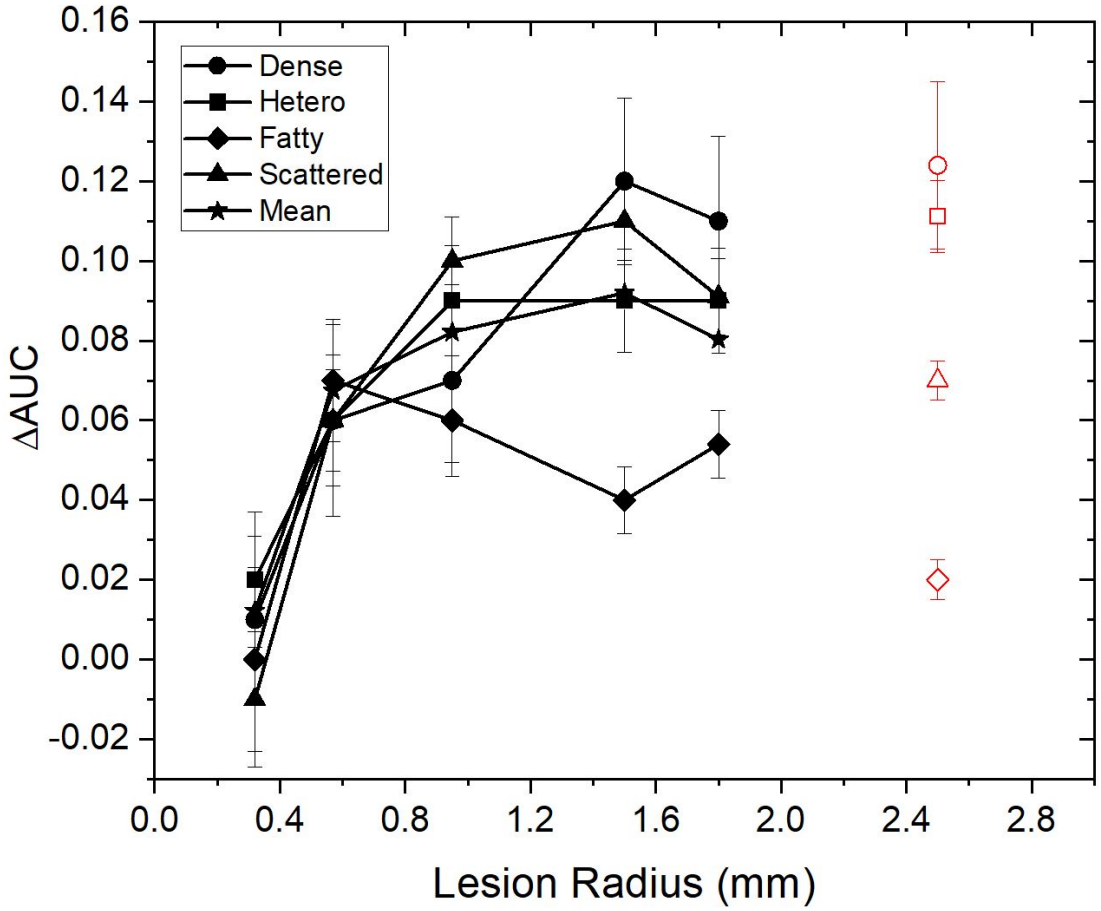

Figure 6.4: Variations in AUC differences (DBT-DM), calculated using the imrmc software (*B. D. Gallas, IMRMC software*, 2013), across the four density classes: dense (circle), hetero (square), scattered (triangle) and fatty (diamond). The data from the VICTRE trial are also included for the four classes. The VICTRE data are the red open symbols, while the black solid symbols represent the L trial data.

6.5 Discussion

To our knowledge, this is the first report of a longitudinal in silico trial following the progression of cancer in literature. On one hand, in clinical practice, if a suspicious mass is detected, it is immediately removed and the appropriate treatment is initiated to stunt its growth and spread. So this kind of trial that evaluates the performances of different imaging modalities through the lifetime of cancerous lesions can only be performed in silico. However, further developments are needed to capture the

variability in patient and disease manifestation, seen in clinical environments.

In general the mean AUC and difference results indicate that DBT outperforms DM as the lesion size increases, consistent with studies reported in literature. In fact, for masses with radius up to 1 mm can be detected using DBT with a 16% higher AUC as compared to DM, for the dense class, which presents the most challenges due to presence of large amounts of overlapping fibroglandular tissues. Since the TMIST trial classifies masses with radii larger than 5 mm to be advanced cases of cancer, our results clearly demonstrate the benefits of DBT for earlier detection of cancers, before they can progress and potentially spread to other parts of the body.

While this study demonstrates the power of conducting such experiments in silico, it suffers from a number of limitations. All masses simulated as part of the L trial were non spiculated and did not include any characteristics to distinguish between benign and aggressive malignant tumors. The masses were inserted using simple voxel replacement, which does not create the tissue distortions around the site of the tumor, a common indicator used by radiologists for diagnosis of cancer. L trial only studies the Siemens DM/DBT system, with wide angle geometry known to favor the detection of masses. This study needs to be replicated for all acquisition geometries, detector technologies and reconstruction algorithms used by other commercially available DM/DBT systems.

6.6 Conclusion

The L trial is the first ever in silico longitudinal trial reported that evaluates the performance of imaging modalities such as DM and DBT throughout the lifetime of cancerous lesions. The findings of the L trial suggest that DBT offers clear benefits over DM for the early detection of cancer with masses of radii as small as 1 mm. For smaller masses, DM may present an advantage as is often the case for microcalcification detection tasks. In the future, we plan to include larger variability in the

trial population, a more sophisticated tumor growth model as well as in silico replicas of other commercially available DM/DBT systems.

CHAPTER VII

Conclusions and Future Work

7.1 Summary of findings

Digital mammography (DM) based breast cancer screening has proven effective in reducing mortality rates across North America and Europe. Advanced imaging techniques like digital breast tomosynthesis (DBT) is being considered as a replacement for DM in screening programs, to address concerns of missed or falsely detected cancers in DM. While DBT has been shown to increase cancer detection rates and reduce recalls, its benefits over DM for earlier detection of cancer, across all commercially available systems have yet to be established to justify its use in screening programs. The goal of this thesis was to investigate a limited version of TMIST using in silico imaging methods: (i) the effect of imaging modalities on the early detection of cancer and (ii) the effect of detector technology on cancer detection. To do so, we needed to develop computational models to replicate lesion growth and performance of x-ray detectors used in commercially available DM/DBT systems.

Chapter 2 introduced the first computational model to simulate growth of breast lesions. Its unique feature was the correlation between the lesion morphology and the mechanical properties of its local anatomical structures, that resulted in a great variety of lesion shapes. While this concept was used specifically for breast lesions in this thesis, it can be applied to simulate tumor growth in any other part of the body such

as the lungs and brain. The model also has the provision to simulate angiogenesis, which involves the effect of peripheral blood vessels. This creates opportunities to investigate other imaging techniques that involve the use of contrast agents. Overall, the best feature of this lesion growth model is its versatility.

In Chapter 3, computational models were developed to replicate the DM performance of commercially used x-ray detectors. We demonstrated via typically used image quality metrics that these models were comparable to three popularly used DM/DBT systems: GE Senographe Pristina, Hologic Selenia Dimensions and Siemens Mammomat Inspiration. While this is a major scientific contribution, the biggest takeaway is the hybrid approach for modeling indirect CsI based x-ray detectors. Other approaches reported in literature are either based on cascaded modeling, which often involve the use of arbitrary fitting functions or detailed Monte Carlo methods, which are extremely time consuming. Neither of these approaches were fit for use as part of in silico trials. The hybrid approach described in chapter 3 harnesses the accuracy of Monte Carlo methods, without compromising on the computational efficiency by using analytical functions to model the optical spread in the detector. Unlike previous Monte Carlo efforts, this model could generate a set of DM/DBT projection views within a reasonable time frame (4-12 hours depending on the size of the breast model), that allowed us to incorporate for the first time, an indirect CsI detector as part of an in silico trial.

Chapters 5 and 6 were aimed at developing in silico trials to study the effects of detector technology and cancer progression on cancer detection for both imaging modalities, using the computational models developed as part of Chapters 2 and 3. Both these trials are great examples that demonstrate the power of conducting experiments in silico. Both Chapters investigate topics that would have been otherwise impossible or unreasonable to undertake in the physical world. The goal of Chapter 5 was to establish a link between the x-ray detectors' image quality metrics and their

clinical performance for DM and DBT. Since we used in silico approaches, we were able to remove all other contributing and confounding factors of the imaging system that could affect the cancer detection rates. It would be unreasonable to do the same with real systems, as it would involve extensive device fabrication and integration with existing DM/DBT system, which is a complex and time consuming process. On the other hand, the longitudinal trial described in chapter 6 could never be replicated in a clinical setting. If a suspicious mass is detected in a patient using DBT or DM, doctors would never recommend a wait-and-watch approach and would immediately start the appropriate treatment to curb its growth. Finally, both studies arrived at important conclusions that could impact decisions regarding the choice of imaging modalities for breast cancer screening: (i) DBT shows clear advantages over DM for earlier detection of cancer and (ii) while DBT outperforms DM for detection of masses, its benefits for micro-calcifications are dependent on detector technology.

7.2 Regulatory Impact

All the computational models developed as part of this thesis will be made open source via Github. They will be made available freely and in open source form for manufacturers to create opportunities for additional sources of regulatory evidence. This could help speed up the regulatory process and allow improvements in technology to be made available to the public sooner.

7.3 Limitations

While through this thesis the benefit of conducting such studies in silico have been clearly demonstrated, they are currently not a replacement for clinical trials and should be used as a supplementary source of evidence to inform their clinical counterparts. In general, in silico trials lack the variability in patient population and

cancer manifestations typically observed in a clinical setting. Validating and assessing realism of each aspect of the in silico framework is also often a challenge.

While the lesion growth model, described in chapter 2, is a great first step that allows us to investigate the impact of imaging technologies through the lifetime of a lesion, it currently does not have any provisions for distinguishing between malignant and benign tumors. A major goal of the TMIST trial is to ascertain if aggressive cancers can be detected earlier with the help of DBT, which can thereby reduce the number of advanced cancers in the population. While our studies showed that DBT, in general, can detect masses at their earlier stages, no conclusions be currently made about the benefits of DBT for the earlier detection of aggressive masses, which affect the long-term health of patients.

Additionally, both trials described in chapter 5 and 6, use the wide-angle geometry from the Siemens DM/DBT system, which is known to favor detection of larger targets. To develop a complete understanding, the same experiments should be repeated with a narrow-angle system geometry to ascertain if the outcomes vary.

7.4 Future Work

While this thesis allows the reader to gain insight into the effects of cancer progression and detector technology on the DM and DBT performance, there are many other clinical and system parameters that need to be investigated. We are currently running in silico trials to investigate the effect of electronic noise on the cancer detection rate. We will also be extending the longitudinal study in chapter 6 to include the other detector technologies currently used in commercial systems.

An interesting future research direction is to improve on the lesion model to accommodate the growth of spiculations, which are one of the common indicators of aggressive breast cancer and demonstrate the realism of the lesion models. We will also be working on developing a model to replicate hexagonal detector pixels, which

are used in the Fujifilm system.

APPENDIX

APPENDIX A

Cascaded Systems Analysis of a-Se/a-Si and a-InGaZnO TFT Passive and Active Pixel Sensors for Tomosynthesis

A.1 Abstract

Medical imaging systems like full field digital mammography (FFDM) and digital breast tomosynthesis (DBT) commonly use amorphous selenium (a-Se) based passive pixel sensor (PPS) direct conversion x-ray detectors. On one hand, direct conversion detectors inherently offer better resolution characteristics in terms of a higher modulation transfer function (MTF), in comparison to the indirect CsI:Tl PPS x-ray imager. On the other hand, especially at lower doses, this superior performance of the direct imager is seldom retained in its detective quantum efficiency (DQE) curves. It is well known that a-Se PPS x-ray imagers suffer from high additive electronic noise originating from the from the amorphous silicon (a-Si) thin film transistor (TFT) array that is being used in the current back-plane technology. This degrades the noise power spectrum (NPS) and subsequently the overall DQE. To address this

deficiency, we propose to replace the PPS back-plane by active pixel sensor (APS) back-plane technology, which has the potential to reduce the back-plane electronic noise by amplifying the input signal, especially at low doses. The proposed APS is based on amorphous In-Ga-Zn-O (a-IGZO) TFT technology, which can offer high mobility (5-20 cm^2/V-s), low leakage current (¡ 10^{-13} A) and low flicker noise (Hooge's parameter α_H 1.5×10^{-3}), leading to better imager noise performance. To test our hypothesis, we used linear cascaded systems analysis to model the imaging performance (MTF, NPS and DQE) of the PPS and APS a-Se direct imagers. This model was first validated using experimentally measured data obtained for a 85 μm pixel pitch a-Se/a-Si TFT PPS imager. Using this model, we analyzed the noise performance of the direct a-Se and indirect CsI:Tl x-ray a-IGZO APS imagers at different dose and electronic noise levels. Obtained results clearly showed that lowering back-plane electronic noise can significantly improve the performance of the a-Se/a-IGZO TFT APS imager. Our simulated results showed that a higher DQE at lower radiation doses (maximum DQE of 0.6 can be achieved at an exposure level of 1 μGy) can be achieved with the a-Se detector, thereby making this combination a promising candidate for low dose applications like DBT.

A.2 Introduction

Today the most commonly used imager (The term 'imager' is used to describe the entire x-ray detection system including the x-ray detector and back-plane electronics.) technology in Digital Breast Tomosynthesis (DBT) systems is based on direct x-ray detectors. Direct conversion detectors (The term 'detector' in this work pertains to the x-ray converting material like a-Se or CsI:Tl.) using x-ray absorbing materials like amorphous selenium (a-Se), convert the incident x-ray photons into electron charges which are collected by a combination of thin-film transistors (TFTs) array (so call back-plane array) and back-end electronics (*Samei and Flynn*, 2003b). The a-Se

is a popular choice for detector material, used by commercial DBT scanners like Hologic Selenia Dimensions, Siemens MAMOMAT Inspiration and Fujifilm Innovality (*Mackenzie et al.*, 2017). For breast cancer detection, the objective of DBT is to acquire a high resolution and a low noise image, at low doses, enabling radiologists to distinguish finer details and low contrast masses, that can be associated with breast cancer. In terms of imager performance, this translates to imager having a high Modulation Transfer Function (MTF), a low Noise Power Spectrum (NPS) and consequently a high Detective Quantum Efficiency (DQE).

Previously, there have been experimental studies on direct a-Se imagers and their performances were compared against that of indirect detectors (*Samei and Flynn*, 2003b; *Monnin et al.*, 2007; *Bisogni et al.*, 2005), which first convert the x-ray photons absorbed by scintillators, such as CsI:Tl, into light emitting photons that are subsequently detected by amorphous silicon (a-Si) pixel photodiodes(*Samei and Flynn*, 2003b). A general consensus amongst all these studies is that the direct x-ray conversion using a-Se has the potential to achieve a higher MTF even at high spatial frequencies (for example, an a-Se detector with comparable pixel pitch can achieve a MTF of 0.55 as compared to 0.21 for an indirect CsI:Tl detector at the same spatial frequency of 3.5 lp/mm)(*Samei and Flynn*, 2003b). However, it has also been found that especially at lower radiation doses, the superior performance of the direct imager is seldom retained in its DQE curves. For example, an a-Se detector irradiated with comparable exposure of 2.6 μGy can achieve a DQE of 0.23 as compared to 0.3 for an indirect CsI:Tl detector at the same spatial frequency of 2 lp/mm(*Samei and Flynn*, 2003b). Hence, it is established that a-Se imagers suffer from a high additive electronic noise(*Zhao*, 2007) originating from the back-end electronics, which degrades the NPS performance and subsequently the overall DQE. This might suggest that we may have hit a roadblock. It is important to note that the imagers investigated in these experimental studies, include not only the direct/indirect x-ray converting

material (or detector) but also different back-end electronics comprising of readout TFTs, analog to digital converters (ADC), charge amplifiers etc. Therefore, if the electronic noise originating from the imager's back-plane (e.g. active-matrix arrays) were to be reduced, the performance of a-Se direct imager could be improved. Currently, the back-plane technology used in commercial DBT systems is based on single a-Si TFT passive pixel sensors (PPS). While a compact structure can be achieved with PPS arrays, they are also a source of high additive electronic noise5, subsequently degrading the overall DQE. Moreover, to acquire DBT slices with a higher resolution, it is necessary to further reduce pixel pitch of the imager. It is difficult to do so using PPS imagers as the smaller aperture size leads to a weaker signal at low doses, thus resulting in a low signal-to-noise ratio in the obtained DBT slices(*Zhao and Kanicki*, 2014). One way to circumvent this issue is by replacing the PPS back-plane by active pixel sensor (APS) technology. In contrast to PPS arrays, APS arrays can reduce the electronic noise contribution by amplifying the input signal(*Zhao and Kanicki*, 2014; *Karim et al.*, 2002). In the recent years, numerous APSs based on CMOS technology have been developed(*Esposito et al.*, 2014; *Konstantinidis et al.*, 2012; *Farrier et al.*, 2009; *RadIcon 2013 RadEye1*, 2013). But CMOS is limited to smaller area imagers. Alternatively, metal-oxide TFTs array technology can be fabricated over a large areas, as has already been shown in flat panel displays (*Metal Oxide TFT Backplanes for Displays 2014-2024: Technologies, Forecasts, Players: IDTechX*, 2014; *Jeong et al.*, 2008). The metal oxide TFTs offer a high field effect mobility (5-20 cm^2/V-s), a low leakage current (¡ 10^{-13} A), low flicker noise (Hooge's parameter α_H 1.5×10^{-3}) and thermal and electrical stability6. It has also been shown that amorphous In-Ga-Zn-O (a-IGZO) TFT APS can be realized(*Zhao and Kanicki*, 2014). Hence, we propose in this paper, for the first time, to integrate the a-Se detector with an a-IGZO TFT APS array, that could result in an improved imager noise performance. This study can be extended to amorphous InSnZnO (a-ITZO) TFTs (*Cheng et al.*, 2017). Since, as the

mode of operation, and material and device properties for CMOS APS and a-IGZO TFT APS are different, the circuitry, the modelling and device parameters for them are also different and must be determined separately through experiments. Details about a-IGZO APS modelling have been discussed previously (*Zhao and Kanicki*, 2014). As experimental studies of imagers can be expensive and time-consuming, we propose to use cascaded system analysis (*Rabbani et al.*, 1987; *Rabbani and Metter*, 1989; *Cunningham et al.*, 1994; *Konstantinidis*, 2011) as proof of concept, to model the imaging performance in terms of MTF, NPS and DQE for the a-Se imager based on PPS and APS technologies. We validated our model by comparing our simulated results against the measured MTF, NPS and DQE obtained for the 85 μm SMAM imager18 from Anrad Corporation. Using this a-Se model and a previously developed analysis for the CsI:Tl indirect detector (*Zhao et al.*, 2015c,a) we analyzed the two imagers for various levels of back-end electronic noise and dose levels. Our analysis showed that if the a-Se imager performed close to its quantum limited behavior, then indeed it has the potential to show a superior DQE performance, as compared to current x-ray imaging technology, especially at lower x-ray exposure levels. To further consolidate our analysis, we used this model to demonstrate that the improved performance can be achieved for the proposed combination of the a-Se detector with a low noise a-IGZO TFT APS back-plane.

A.3 Methods

A.3.1 Novel a-Se/a-IGZO TFT APS imager

Ideally, to achieve the best imaging performance in terms of higher DQE, the imaging system should be quantum limited, which means that the only source of noise is the x-ray quantum noise. This can be achieved if either the detector Air Kerma (DAK) levels are considerably high or the electronic noise component originating

from the PPS or APS back-plane is low. For intermediate dose applications like mammography, where only the normal projection view of the breast is obtained, a higher electronic noise component may be tolerated. Digital breast tomosynthesis (DBT) delivers a similar mean glandular dose (MGD) to the breast as mammography, but over several projections. So, to achieve sufficient signal-to-noise ratio (SNR) and to improve the performance of the current a-Se / a-Si TFT PPS imager in terms of NNPS, DQE and spatial resolution especially at lower DAK levels, we need to realize an imager with reduced electronic noise.

One approach to improve the noise performance (NPS) of the a-Se imager is by employing an APS (*Karim et al.*, 2002) instead of the currently used PPS back-plane (*Konstantinidis*, 2011). While we can achieve a compact structure with PPS arrays, APS arrays can reduce the electronic noise contribution by amplifying the input signal(*Karim et al.*, 2002; *Zhao and Rowlands*, 1995). Previously, our group investigated different APS pixel circuits to enhance the imager performance such as current-mode (*Cheng et al.*, 2017), voltage-mode (*Cheng et al.*, 2016) and trans-impedance amplifier (TIA) (*Kim*, 2017). For this work, we propose to integrate the a-Se detector with current-mode APS (C-APS).

The equivalent circuit for the a-Se detector layer, as shown in fig. A.1 (a) consists of a current source (I_{Se}), capacitance (C_{Se}) and reverse biased diode (D_{Se}). As shown in fig. A.1 (b), in PPS imagers, the pixel circuit consists of only one TFT and a storage capacitor (C_s). When the TFT is switched on by the gate lines, it transfers the charge on the storage capacitor to the readout circuit. A schematic of an equivalent circuit for the novel a-Se a-IGZO 3-T C-APS imager is shown in fig. A.1 (c). The C-APS circuit consists of three TFTs – reset, amplifying and read (T_{RST}, T_{AMP} and T_{READ}). In the reset mode, only T_{RST} is switched on (by V_{RST}), which sets the voltage V_{IN} to V_{REF} (chosen to be greater than the threshold voltage of T_{AMP}) Next, in the integration mode, the charge generated due to the incident x-rays accumulates on the

storage capacitor (C_s), which changes the voltage V_{IN}. After the integration stage, T_{READ} is switched on (by V_{READ}), which transfers an amplified signal (through T_{AMP}) to the data-line (consisting of a parasitic resistance R_{DATA} and capacitance C_{DATA}) and external readout circuit (a switched-capacitor amplifier where SW acts as the switch). The final output charge is thus stored on the feedback capacitor, C_F. Thus, the APS circuit provides a charge gain. The APS circuit cannot reduce the effect of any pre-amplifying noise (originating from T_{RST} leakage current, shot noise and reset noise), but can eliminate the influence of the post-amplifying noise (thermal and flicker noise from T_{AMP} and T_{READ} and external readout circuit noise). Moreover, if the currently used a-Si TFT technology is replaced by a-IGZO TFT technology, the noise performance of the imager can be further improved.

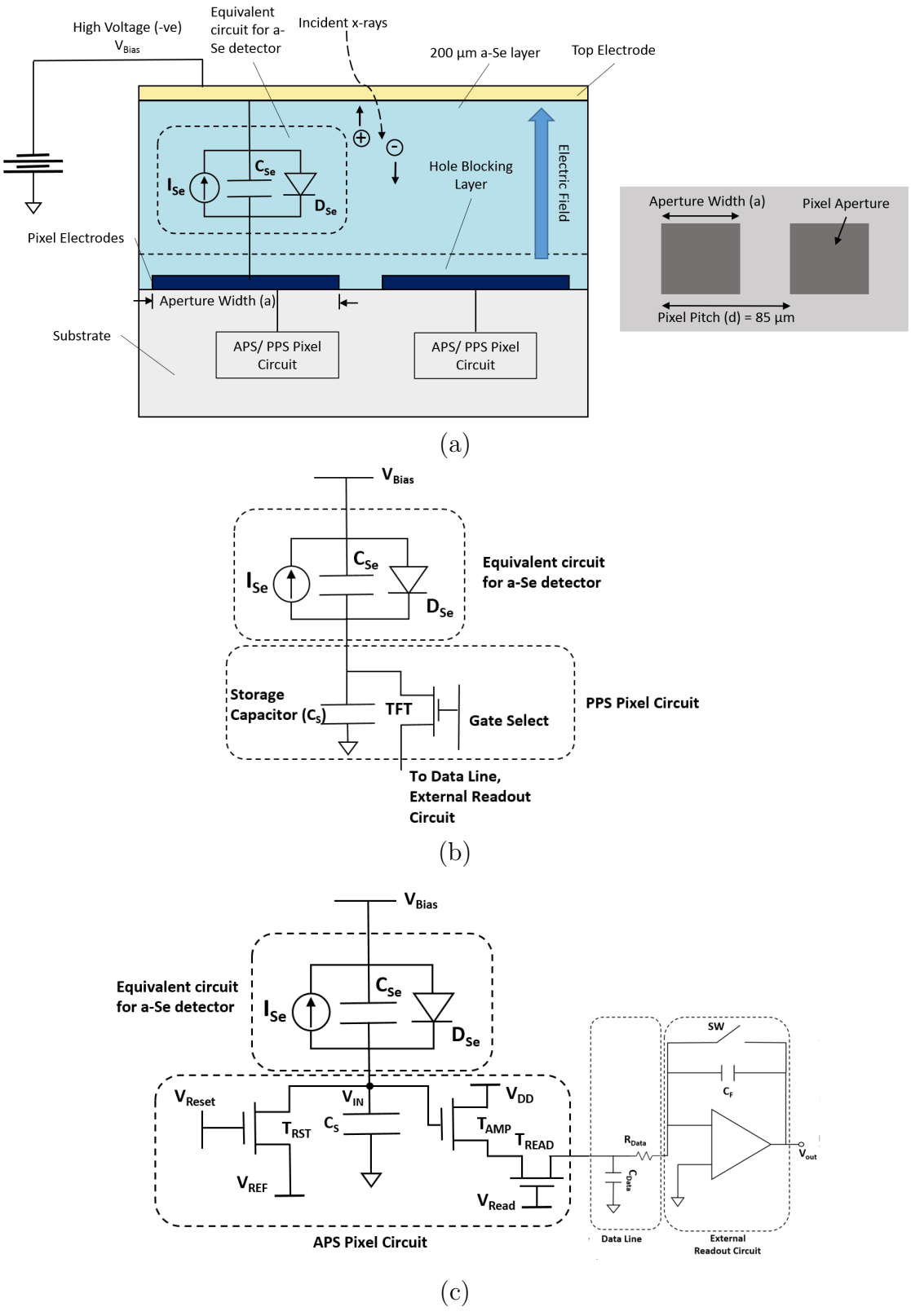

Figure A.1: (a) Cross-sectional and top view schematic of a-Se imager (b) Circuit diagram for a-Se/a-Si TFT PPS and (c) Circuit diagram for a-Se/a-IGZO TFT APS.

To analyze the performance of the novel a-Se/a-IGZO TFT C-APS imager, we have to model it's signal and noise characteristics at each stage of the detection process in x-ray imagers. Cascaded linear systems analysis is a useful tool developed by Rabbani et. al.(*Rabbani et al.*, 1987; *Rabbani and Metter*, 1989) and Cunningham et. al.(*Cunningham et al.*, 1994) to study the propagation of the signal and noise through x-ray detectors as series of blurring and gain stages. Previously, we already had performed such a cascaded analysis for an indirect 50 μm pixel pitch CsI:Tl CMOS APS imager (*Zhao et al.*, 2015c,a). Cascaded modelling for a-Se a-Si TFT PPS imagers has also been studied in the past (*Zhao and Rowlands*, 1997; *Kabir et al.*, 2011; *Zhao et al.*, 2003). We will be following a similar, but simplified, approach to first develop a linear cascaded system model for a direct a-Se a-Si TFT PPS imager and use it to demonstrate the advantages of the proposed novel a-Se/ a-IGZO TFT APS imager.

A.3.2 Linear Cascaded Modelling of a-Se X-ray Imagers (PPS and APS)

The schematic of an equivalent circuit of an a-Se x-ray imager with an a-Si TFT PPS back-plane is shown in fig. A.1 (b). A fraction of the incident x-rays, determined by the thickness and attenuation coefficient of Se, is absorbed in the a-Se detector layer. Each absorbed x-ray photon creates a primary photo-electron, through the photo-electric effect (photons having energy greater than the K-edge of Se, 12.66 keV, can eject a primary photo-electron form the K-shell) or through Compton scattering (*Que and Rowlands*, 1995b). This primary electron carries a large amount of kinetic energy and as it travels through the Se layer, it collides randomly with Se atoms and creates thousands of secondary electron-hole pairs, until all its kinetic energy is lost. The high electric field (up to 10 V/μm across the Se layer) developed between the top electrode (that could be negatively and positively biased, in fig. A.1 negative voltage is applied) and the ground plane of the TFT array causes the electrons and holes

(positive charges) separation that will drift along the filed lines to be collected by the pixel and top electrodes, respectively (*Konstantinidis*, 2011). The pixel electrode is connected to a storage capacitor electrode which is in series with the a-Se layer capacitance. The electronic charges are collected and accumulate on combination of these two capacitors (bias voltage applied to the circuit is divided according to the capacitance ratios) and, thereby, provides a charge signal that can be read during self-scanning by back-end electronics. Since a-Se is a photoconductor, each pixel electrode carries an amount of charge that is proportional to the amount of incident x-ray radiation. The simplest a-Si TFT PPS technology has only one a-Si TFT per pixel circuit. When the TFT is switched on for a given period of time, by the gate line, it transfers the charge stored, across combination of the a-Se and storage capacitor, to the readout columns, where the charge is amplified and digitized. The entire array is read in a row-by-row manner (*Konstantinidis*, 2011).

As shown in fig. A.2, similar to the previously developed cascaded models(*Zhao and Rowlands*, 1997; *Kabir et al.*, 2011; *Zhao et al.*, 2003), the x-ray detection mechanism in the a-Se / a-Si TFT imager, as described above, can be divided into the following 8 stages: (i) absorption of x-ray energy in a-Se (ii) inherent stochastic blurring in a-Se (iii) conversion of x-ray photons into electron-hole pairs (iv) collection of the electron-hole pairs at the respective electrodes (v) blurring due to hole blocking layer (vi) aperture blurring (vii) noise aliasing and (viii) addition of electronic noise from the a-Si PPS back-plane. The purpose of this study is to build a simplified model, taking into consideration the most important x-ray detection mechanisms, which can be used to reasonably estimate and predict the performance of current and novel x-ray imager technologies. Thus, the spreading of the electronic signal due to re-absorption of K-fluorescent x-rays (*Que and Rowlands*, 1995b) have been ignored in this model. Although we recognize that the K-fluorescence should not be ignored in a-Se imagers (*Que and Rowlands*, 1995b). All the parameter values used for this

cascaded analysis model are given in Table. A.1.

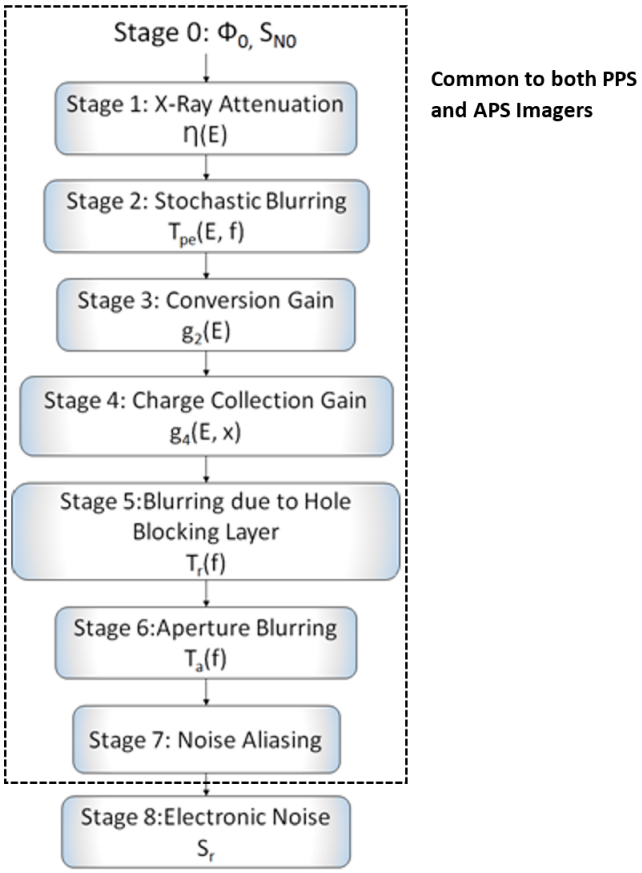

Figure A.2: Linear Cascaded Modelling of a-Se imager. Stages 0-7 are common for PPS and APS imagers. Stage 8 is related to only PPS imagers.

Parameter	Value	Description
$\overline{\varphi}_0$	6552 photons/mm^2/μGy	Mean x-ray photon fluence per unit DAK
g_1	0.68	Energy quantum efficiency
g_3	505.17	Conversion gain
g_4	0.89	Charge collection efficiency
dSe	200 μm	Thickness of a-Se
FF	0.89	Fill factor
a	80 μm	Aperture width
d	85 μm	Pixel pitch
F	10 V/μm	Electric field
μ_e	0.003 cm^2/V.sec	Electron mobility
μ_h	0.12 cm^2/V.sec	Hole mobility
τ'_e	100 μs	Electron lifetime
τ'_h	20 μs	Hole lifetime

Table A.1: Parameters used in cascaded analysis of Anrad SMAM a-Se detector

A.3.2.1 Stage 0: Incident x-ray photon fluence

A polychromatic x-ray spectrum using Tungsten (W) anode with a peak voltage of 28 kV$_\mathrm{p}$, total of 2.5 mm Aluminum (Al) filtration was simulated in this study to achieve a mean photon energy of 22.3 keV, and HVL of 0.83 mm Al, which is considered standard for mammography (IEC 62220-1-2 2007). The Air Kerma at the surface of the detector (DAK) was set to be 1 μGy. Using this simulated spectrum, the mean x-ray photon fluence per unit DAK ($\overline{\varphi}_0$) is calculated as:

$$\overline{\varphi}_0 = \sum_{E=0}^{E_{\max}} \varphi_0(E)\,\Delta E \tag{A.1}$$

Here, $\overline{\varphi}_0$ has the units of photons/mm^2/μGy, $E$is the x-ray photon energy in keV and $\varphi_0(E)$is the x-ray spectrum incident on the detector. So the fluence at a DAK value of K_a μGy would be $Ka \times \overline{\varphi}_0$ photons/mm^2.

Since x-ray quantum noise follows Poisson distribution (*Kabir et al.*, 2011), the noise for this stage, S_{N0}, can be expressed as:

$$S_{N0} = \overline{\varphi}_0 \tag{A.2}$$

Here, S_{N0} is spatially white noise, which means that it is independent of the spatial frequency. Once the spatial frequency component is included in the later stages, the noise power spectrum (NPS) will be calculated.

A.3.2.2 Stage 1: Absorption of X-ray Energy in a-Se

This stage describes what fraction of the incident x-ray energy is absorbed (and could be utilized) by the a-Se detector. Since a-Se detectors are energy integrators[2], the gain for this stage (g_1) is called the energy absorption efficiency (EAE), which is the ratio of the total energy absorbed per unit incident energy. So g_1 is calculated as:

$$g_1 = \frac{\sum_{E=0}^{E_{\max}} \varphi_0(E) \times \left(1 - e^{-\mu(E) dSe}\right) \times E \times \left(\frac{\mu_{en}(E)}{\mu(E)}\right) \times \Delta E}{\sum_{E=0}^{E_{\max}} \varphi_0(E) \times E \times \Delta E} \tag{A.3}$$

Here, dSe is the a-Se detector thickness in cm, μ and μ_{en} are the linear and energy attenuation coefficients for a-Se. μ_{en} describes the fraction of the incident x-ray energy which can be transferred to the charged particles as kinetic energy, including all the radiative losses and $\mu$is the linear attenuation coefficient. So the term: $E \times \left(\frac{\mu_{en}(E)}{\mu(E)}\right)$ describes the amount of energy absorbed in a-Se per attenuated x-ray photon (*Boone*, 2000).

Thus the signal and noise of the a-Se imager at this gain stage is given by equations 4 and 5 respectively:

$$\overline{\varphi}_1 = g_1 \times \overline{\varphi}_0 \tag{A.4}$$

$$S_{N1} = g_1 \times \overline{\varphi}_0 \tag{A.5}$$

A.3.2.3 Stage 2: Stochastic Blurring by Photo-conductor

The two dominant sources of 3-D spreading of the electronic signal in a-Se are the photoelectric effect and re-absorption of the K-fluorescent x-rays (*Que and Rowlands*, 1995b).

Photoelectric Effect: In the photo-electric effect, the incident x-ray photon gets completely absorbed and releases a primary electron from a bound state of the Se atom. This primary electron (also called photo-electron) carries a large amount of kinetic energy, which is the difference between the incident x-ray photon energy and the electron's binding energy. As the photo-electron travels through the selenium layer, it collides randomly with Se atoms and creates several secondary electrons, until all its kinetic energy is lost. The size of this electron cloud, which is a function of how far the photo-electron can travel (range), determines the spreading of charge and blurring associated with this process.

Previously, Que and Rowlands modelled the blur due to the range of the primary photoelectron as (*Que and Rowlands*, 1995b):

$$T_{pe}\left(E,f\right)=\exp(-\pi^2\delta^2f^2) \tag{A.6}$$

where,

$$\delta=\frac{R_{\max}}{2.5} \tag{A.7}$$

and

$$R_{\max}=\frac{2.761\times10^{-5}\times M_{at}\times(E-Kedge)^{\frac{5}{3}}}{\rho\times Z^{\frac{8}{9}}} \tag{A.8}$$

Here, M_{at} is the atomic mass in g.mol^{-1}, ρ is the density in g/cm^3, Z is the atomic number of a-Se, f is the spatial frequency in lp/mm and $Kedge$ is the K-edge of a-Se

in keV (12.66 keV). $R_{\max}$ (in mm) can be thought of as a measure of the average distance between where the primary photo-electron was created and where it stops. Here the $R_{\max}$ is about 2.1 μm when $E = 28keV$.

To express $T_{pe}(E, f)$, only as a function of frequency, $T_{pe}(f)$ is calculated as the weighted average of all the absorbed photons:

$$T_{pe}(f) = \frac{\sum_{E=0}^{E_{\max}} \varphi_0(E)\, T_{pe}(E, f)\, \Delta E}{\sum_{E=0}^{E_{\max}} \varphi_0(E)\, \Delta E} \tag{A.9}$$

So the signal and NPS after this stochastic blurring stage is given by equation 10 and 11:

$$\overline{\varphi}_2(f) = \overline{\varphi}_1 . T_{pe}(f) \tag{A.10}$$

$$S_{N2}(f) = T_{pe}^2(f)\, S_{N1} + (1 - T_{pe}^2(f))\overline{\varphi}_1 \tag{A.11}$$

Note that this is the first stage where the spatial frequency is also included in the calculations. So NPS is calculated instead of noise.

A.3.2.4 Effect of Re-absorption of K-fluorescence:

If during the photoelectric process, the primary electron is ejected from an inner atomic shell, it can result in a cascade of electrons from the outer shells, which can consequently result in the emission of characteristic x-ray photons. (*Que and Rowlands*, 1995b) These characteristic x-rays are called K-fluorescent x-rays when the primary electron is ejected from the K-shell of the Se atom. These K-rays when absorbed at a different location in the detector volume, may result in additional spread of the signal. From previous studies (*Que and Rowlands*, 1995b),it was found that for lower energy applications (mean energy of 20 keV), the effect of reabsorption of K-fluorescence can create up to a 28% change (reduction) in the total MTF for a

1000 μm thick imager (*Que and Rowlands*, 1995b). For higher energy spectra (peak voltage of 75 kVp), the effect of K-fluorescence is negligible (*Kabir et al.*, 2011). So it is recognized and accepted that for DBT, the effect of K-fluorescence ideally should not be ignored. However, our analysis showed that the effect of reabsorption of K-fluorescent rays accounts for about 10% variation in the imager's MTF which is tolerable for our study. Hence, to simplify our cascaded systems model, we ignored the effect of reabsorption of K-fluorescent rays in this work and only considered the contribution from the photoelectric effect. This assumption can be revisited when additional analysis of the a-IGZO TFT imager are needed for designing the actual products.

A.3.2.5 Stage 3: Conversion Gain

The conversion gain $g_3'(E)$ represents the mean number of free electron hole pairs generated in a-Se by the photo-electric effect following the absorption of an x-ray photon of energy E. $g_3'(E)$ is calculated as:

$$g_3'(E) = \frac{E}{W_\pm} \tag{A.12}$$

$W_\pm$ is called the activation energy or the energy required to create a single electron hole pair (EHP) in a-Se. For most crystalline semiconductors (like HgI_2) $W_\pm$ can be calculated using the Klein rule: $W_\pm \approx 3E_g$(*Kasap et al.*, 2011). However, for low mobility solids, like a-Se, it has been found that $W_\pm$ has a strong dependence on the applied electric field (F), which can be described by:

$$W_\pm = W_\pm^0 + B/F \tag{A.13}$$

where, $W_\pm^0$ is the intrinsic EHP creation energy at an infinite electric field and B is a constant. For an electric field of 10V/μm, $W_\pm$ is calculated to be 50 eV (*Kasap et al.*,

2011). This value has been verified experimentally by Rowlands et. al. (*Rowlands et al.*, 1992).

The overall gain for this stage is given as:

$$g_3 = \frac{\sum_{E=0}^{E_{\max}} \varphi_0(E) \times \eta(E) \times g_3'(E) \times E \times \Delta E}{\sum_{E=0}^{E_{\max}} \varphi_0(E) \times \eta(E) \times E \times \Delta E} \tag{A.14}$$

$$\eta(E) = 1 - e^{-\mu(E) dSe} \tag{A.15}$$

Where, dSe is the a-Se detector thickness in cm, μ and μ_{en} are the linear and energy attenuation coefficients for a-Se. $\eta(E)$ is also known as the monochromatic photon energy quantum detection efficiency (QDE).

The variance in gain is:

$$\sigma_{g3}^2 = ffactor \times g_3(E) \tag{A.16}$$

Where, $ffactor$ is the Fano factor (*Darbandi et al.*, 2012).It has been shown by Darbandi et. al. (*Darbandi et al.*, 2012), that the intrinsic value of the Fano factor in a-Se is within 0.03-0.06. However, due to recombination of charges in a-Se these values are seldom achieved. In fact for an electric field of 10V/μm, the Fano factor approaches 0.9-1 (*Darbandi et al.*, 2012). Moreover, assuming that mean number of electron hole pairs released per x-ray photon obey a Poisson process (*Kabir et al.*, 2011), the Fano factor is determined to be 1 and the variance to be:

$$\sigma_{g3}^2 = g_3(E) \tag{A.17}$$

So the signal and the NPS from this gain stage are calculated using equations 14 and 16b as:

$$\overline{\varphi}_3(f) = g_3 \times \overline{\varphi}_2(f) \tag{A.18}$$

$$S_{N3} = g_3^2 S_{N2}(f) + \sigma_{g3}^2 \overline{\varphi}_2(f) \tag{A.19}$$

A.3.2.6 Stage 4: Charge Collection

The average charge collection efficiency, $\overline{g}_4$, at the pixel electrodes when electron-hole pairs are created at a distance x from the top electrode, under negative bias, is given by (*Kabir et al.*, 2011):

$$g_4 = \left[\tau_h \int_0^1 (1 - e^{-(\frac{x}{\tau_h})}) dx + \tau_e \int_0^1 (1 - e^{-(\frac{1-x}{\tau_e})}) dx \right] \tag{A.20}$$

The variance in the gain is given by[25]:

$$\sigma_{g4a}^2 = [\int_0^1 \tau_h^2 dx + \int_0^1 \tau_e^2 dx - \tau_h^2 \int_0^1 e^{-\frac{2x}{\tau_h}} dx -] \tag{A.21}$$

$$\sigma_{g4}^2 = [\sigma_{g4a}^2 - \tau_e^2 \int_0^1 e^{-2(\frac{1-x}{\tau_e})} dx - 2\tau_h \int_0^1 x e^{-(\frac{x}{\tau_h})} dx - 2\tau_e \int_0^1 (1-x)(e^{-(\frac{1-x}{\tau_e})}) dx] \tag{A.22}$$

Where,

$$\tau_e = \frac{\mu_e \tau_e' F}{dSe} \tag{A.23}$$

and

$$\tau_h = \frac{\mu_h \tau_h' F}{dSe} \tag{A.24}$$

Where, μ_e (or μ_h) is the mobility, τ_e' (or τ_h') is the deep trapping time (lifetime) of electrons (or holes) in seconds and F is the electric field in V/cm. So τ_e (or τ_h)

is related to the average distance travelled by the electron (or hole) before they are trapped. The values for μ_e, μ_h, τ_e' and τ_h' are provided in Table 1.

So the gain and variance equations (19 and 20) are used to calculate the signal and NPS at this stage is given by equations 23 and 24 respectively:

$$\overline{\varphi}_4(f) = g_4\overline{\varphi}_3(f) \tag{A.25}$$

$$S_{N4}(f) = g_4^2 S_{N3}(f) + \sigma_{g4}^2\overline{\varphi}_3(f) \tag{A.26}$$

A.3.2.7 Stage 5: Blurring due to Hole Blocking Layer

The stochastic blurring stage is due to a hole blocking layer located at the bottom of the detector; its purpose is to limit the dark leakage current, fig. 1. The interface between hole blocking layer and the a-Se detection layer traps the drifting electrons before they can reach the pixel electrodes (*Hunter et al.*, 2007). The trapped electrons can induce a negative charge, located at a distance l causing a spreading of the signal. This signal spreading can be expressed as (*Hunter et al.*, 2007) (*Zhao et al.*, 2003):

$$T_r(f) = \frac{dSe \times sinh(2\pi f(dSe - l))}{(dSe - l) \times sinh(2\pi f dSe)} \tag{A.27}$$

For the cascaded modelling, l can be thought of as a fitting parameter. In this study, the best value for l was determined to be 10 μm to achieve a good theoretical fit to the experimental data. While the true value for the hole blocking layer thickness in this imager is unknown, previous studies (*Zhao et al.*, 2003) (*Hunter et al.*, 2012)have shown that the thickness of the hole blocking layer is typically $\sim$ 3-4% of the total a-Se thickness. So the 10 μm value of$l$ is reasonable for a 200 μm thick a-Se layer.

It is important to note that the above equation describes the charge trapping at a single location e.g. at the a-Se/hole blocking layer interface. Of course, it is possible

that the charge trapping can occur throughout the a-Se thickness as described by Kabir et. al. (*Kabir et al.*, 2011). In this case, the trapped bulk charges can induce additional charge that can give rise to additional signal blurring and reduction in the overall MTF of the imager (*Kabir and Kasap*, 2003). However, it has been suggested that for the low exposure rates used in diagnostic applications, the impact of bulk trapping on signal blurring can be neglected (*Hunter et al.*, 2007).

Since this a stochastic blurring stage, the signal spectrum and NPS can be written as:

$$\overline{\varphi}_5(f) = \overline{\varphi}_4 . T_r(f) \tag{A.28}$$

$$S_{N5}(f) = T_r^2(f) S_{N4} + (1 - T_r^2(f)) \overline{\varphi}_4 \tag{A.29}$$

A.3.2.8 Stage 6: Aperture Blurring

In a-Se detectors, the top electrode is continuous, but the bottom electrode is divided into pixels as shown in fig. 1(a). So, as the a-Se layer is continuous, the signal spreading within the a-Se layer, before the charge carriers reach the pixel electrodes, is not affected by the pixel size. On the other hand, the overall MTF of the imager also includes the MTF due to pixel aperture, which changes with the pixel size. The deterministic signal spreading associated with the square shape of pixel electrodes is expressed as

$$T_a(f) = |sinc(a.f)| \tag{A.30}$$

Here, a is the pixel electrode width in mm. a is related to the pixel pitch d (in mm), by the relation:

$$a^2 = FF \times d^2 \tag{A.31}$$

Here, FF is the pixel fill factor, which defines the x-ray sensitive area ($a^{\,2}$) to the total pixel area (d^2).

The signal spectrum and NPS at this stage are given by the following equations:

$$\overline{\varphi}_6(f) = a^2 \overline{\varphi}_5(f) .T_a(f) \tag{A.32}$$

$$S_{N6}(f) = a^4 T_a^2(f) S_{N5} \tag{A.33}$$

A.3.2.9 Stage 7: Noise Aliasing

The detector Nyquist frequency (also called cut-off frequency) define the maximum spatial resolution that can be visualized in an image. The objects or details of objects with a spatial frequency higher than f_{Nyq} are visualized in the form of artifacts superimposed on lower frequency objects, which is called aliasing. The aliasing represents additional source of noise in the image that effects the signal-to-noise ratio, hence the image detection process. The noise aliasing is calculated using a comb function as:

$$S_{N7}(f) = \sum_{m=-\infty}^{\infty} S_{N6}\left(f - \frac{m}{d}\right) \tag{A.34}$$

The signal spectrum and MTF remain unchanged.

The 85 μm pixel pitch of the imager results in aliasing of the NPS at frequencies above the Nyquist frequency, $f_{Nyq} = \frac{1}{(2\times d)} = 5.88 \approx 5.5$ line pairs (lp)/mm.

As compared to indirect detectors, the direct detectors having the same pixel size offer a much higher MTF even at high spatial frequencies[2]. However this also results in a much stronger aliasing effect in the NPS. To eliminate aliasing, the MTF of the

ideal detector should be equal to zero beyond its f_{Nyq}, which is not possible. This means that the practical detector with a high MTF should have highest possible spatial resolution (e.g. smallest pixel size) to limit the aliasing and to detect the smallest possible feature sizes.

A.3.2.10 Stage 8: Read noise

The imager electronics, consisting of back-plane array of TFTs, charge amplifiers and ADCs, which are used to convert the electronic charge collected at the pixel electrodes into the final digital number, contribute a spatially white noise component, N_e (5200 e^- rms for a-Si PPS) (*Konstantinidis*, 2011), to the NPS. So, the final NPS is given by:

$$NPS(f) = S_{N7}(f) + S_r \tag{A.35}$$

where,

$$S_r = N_e^2 \times d^2 \tag{A.36}$$

The N_e value related to PPS imagers is an experimentally determined number (*Konstantinidis*, 2011).

A.3.2.11 Final MTF, DQE and NNPS calculation (for PPS imagers):

Thus the final MTF, signal spectrum, NNPS and DQE used to characterize the a-Se imager are calculated using the following equations (*Siewerdsen et al.*, 1997):

$$MTF(f) = T_a(f) \times T_{pe}(f) \times T_r(f) \tag{A.37}$$

$$\overline{\varphi} = a^2 \times g_1 \times g_3 \times g_4 \times \overline{\varphi}_0 \tag{A.38}$$

$$NNPS\,(f) = \frac{NPS\,(f)}{\overline{\varphi}^2} \tag{A.39}$$

$$DQE\,(f) = \frac{MTF\,(f)^2}{\overline{\varphi}_0 \times NNPS(f)} \tag{A.40}$$

The NNPS and DQE curves are simulated using equations 37 and 38 and analyzed for DAK levels ranging from 3 – 53 μGy, which is considered appropriate from low dose DBT applications (*Zhao and Zhao*, 2008). Higher DAK values (up to 160 μGy) are also used, but only to validate the cascaded analysis model against experimental data.

DQE is influenced by the noise generated by the detector and by its spatial resolution. Hence, its reflects degradation of the signa-to-noise ratio (SNR) occurring between detector input and output.

A.3.2.12 Stage 8 Modifications needed for a-IGZO TFT APS modeling:

To simulate the performance of the a-Se imager in combination with the a-IGZO TFT APS arrays back-plane, we modify the cascaded analysis model as shown in Fig. A.3. Replacing the PPS back-plane with an APS does not affect any of stages in the cascaded model (conversion gain, charge collection etc.) before Stage 8 (Read Noise). Stage 8 (read noise) is the only stage in the cascaded model shown in fig. 2 which is associated with the PPS back-plane. For simulating an imager with an APS back-plane, Stage 8 will be replaced by a signal amplification (Stage 8) and a post-amplification electronic noise (Stage 9) step. Previously, we already had modelled the noise performance of an a-IGZO TFT APS array that was integrated with a CsI:Tl scintillator[6]. In this analysis, we will follow a similar approach to include the signal amplification and electronic noise component originating from an a-IGZO TFT APS. Thus, the final NPS and signal spectrum are calculated with the following equations:

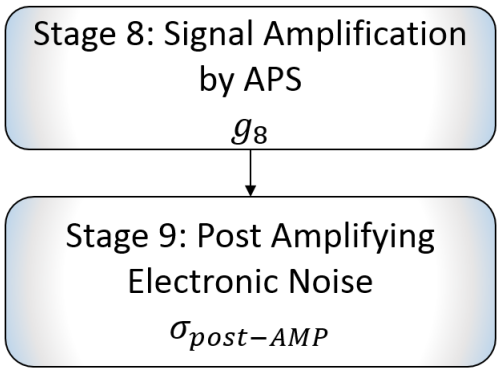

Figure A.3: Linear Cascaded Modelling of a-Se/a-IGZO TFT APS imager.

$$NPS\,(f) = S_8\,(f) = \left(S_7\,(f) + \sigma^2_{pre-AMP} * d^2\right) * g_8^2 + \sigma^2_{post-AMP} * d^2 \tag{A.41}$$

$$\overline{\varphi} = a^2 \times g_1 \times g_3 \times g_4 \times g_8 \times \overline{\varphi}_0 \tag{A.42}$$

Where, $\sigma_{pre-AMP}$ is the input referred pre-amplifying noise (609 e$^-$), g_9 is the APS gain (69) and $\sigma_{post-AMP}$ is the output referred post-amplifying noise (137 e$^-$)[6]. These values for $\sigma_{pre-AMP}$, g_9 and $\sigma_{post-AMP}$ have been calculated using the approach described by Zhao et. al.[6]. $\sigma_{pre-AMP}$ also includes the shot noise originating from leakage current in a-Se given by[6]:

$$\sigma_d = \sqrt{\frac{J_{dark} \times a^2 \times t_{frame}}{q}} \tag{A.43}$$

where, J_{dark} is the leakage current, t_{frame} is the frame time, a is the aperture width and q is the electronic charge. Assuming J_{dark} = 1 pA/mm^2, a = 80 μm and t_{frame}= 145 ms, σ_d = 76 e$^-$. For the PPS imager, σ_d is a negligible as compared to the electronic noise of 5200 e$^-$.The total electronic noise of a-Se/ a-IGZO TFT APS detector is 625 e$^-$.

The NNPS and DQE for the a-Se a-IGZO TFT APS imager are calculated using equations 37, 38, 39 and 40. The MTF remains the same for both the PPS and APS back-planes.

A.3.3 Analysis of CsI:Tl indirect and a-Se direct x-ray imagers

Previously, there have been experimental studies to compare the performance of the CsI:Tl indirect and a-Se direct detectors (*Samei and Flynn*, 2003b; *Monnin et al.*, 2007; *Bisogni et al.*, 2005), which showed that while the a-Se x-ray imagers have better MTF properties, a similar superiority in terms of DQE curves in comparison to CsI:Tl

x-ray imagers have not been observed. However, these experimental studies include not only the direct/indirect x-ray converting material (or detector) but also different back-end and readout electronics. A major component of the measured NPS is the additive electronic noise originating from the a-Si TFT PPS array that is being used in the current back-plane technology.

An advantage of using cascaded analysis to compare direct and indirect imagers is that we can predict their performance at various electronic noise originating from a PPS back-plane and different DAK levels, without time consuming and expensive experiments. To perform such an analysis, it is important to pick the right metric to compare the two imager technologies. One such metric could be the DQE value at the Nyquist frequency (DQE (f_{nyq})), which indicates the smallest feature size that can be resolved. For a 85μm pixel pitch the Nyquist frequency is $f_{Nyq} = 5.88 lp/mm$.

However, while DQE (f_{nyq}) is an important metric, it does not include all the points in the frequency spectrum. So it is important to define a metric that can incorporate the advantages and disadvantages of both imager technologies for a given frequency spectrum. Direct detectors boast a higher MTF as compared to indirect ones. But at the same time direct detectors suffer from a higher aliasing noise as result of their higher MTF. So if only one point in the frequency spectrum is used to compare the two detector technologies, the results may be biased – the lower frequencies may favor direct detector and vice-versa. So it is necessary to use a metric that spans the entire frequency spectrum to have a complete understanding of the two detectors. Hence, in this work we are introducing a new figure of merit (FOM) to facilitate such comparison as:

$$FOM\left(\frac{1}{mm^3}\right) = \frac{\gamma^2}{\beta^2_{FOM}} \tag{A.44}$$

$$\beta^2_{FOM} = \sum_{f=-f_{Nyq}}^{f_{Nyq}} NPS\,(f) \times df \tag{A.45}$$

$$\gamma^2 = \left(\overline{\varphi}(k) \times \sum_{f=-f_{Nyq}}^{f_{Nyq}} MTF\,(f) \times df \right)^2 \tag{A.46}$$

where, df is the spatial frequency step size of 0.5 lp/mm.

In our previous work, we have described a novel indirect imager composed of a CsI:Tl scintillator, organic photodiode (OPD) and a-IGZO TFT APS backplane[6]. This indirect imager showed significant improvements as compared to the currently used CsI:Tl/ a-Si photodiode/ a-Si TFT PPS imager. As compared to the a-Si technology that achieved a maximum DQE (0) of ∼0.4, our proposed indirect imager was able to attain up to DQE (0) of ∼ 0.8, for an exposure level at the detector surface of about 1 mR (*Zhao and Kanicki*, 2014). One of the goals of this work is to compare the previously proposed indirect CsI:Tl/ OPD/ a-IGZO TFT APS imager to the novel a-Se/a-IGZO TFT APS direct imager described in this work. Since, the direct imager is expected to simplify the x-ray imagers' fabrication steps and could more easily transition to flexible / conformable x-ray imaging technology, it is important to evaluate its feasibility. The parameters used for the cascaded analysis model for the indirect CsI:Tl/ OPD/ a-IGZO TFT APS imager are shown in Table A.2, while those used for the direct imager analysis is provided in Table A.1.

Parameter	**Value**	**Description**
g_1	0.55	Energy quantum efficiency
g_2	580	Scintillator mean quantum gain
g_4	0.44	FOP∗ optical coupling efficiency
g_6	0.64	OPD EQE
FF	0.87	Fill factor

Table A.2: Parameters used in cascaded analysis of CsI : Tl/ OPD/ a-IGZO TFT APS imager

The FOM be calculated for the CsI:Tl imager with a 85 μm pixel pitch, previously

described by Zhao et al (*Zhao and Kanicki*, 2014; *Zhao et al.*, 2015c).

A.4 Results

A.4.1 Imaging performance of 85 μm a-Se/a-Si TFT PPS imager

Using our a-Se cascaded systems model, we first characterized the performance of the 85 μm a-Se/a-Si TFT PPS (Anrad SMAM) imager, which has been experimentally evaluated by Konstantinidis *Konstantinidis* (2011). To validate our model, we compared the simulated curves (using equation 35) for MTF, NNPS and DQE with the measured data. Fig. 4 (a) illustrates the measured and simulated MTF curves up to the Nyquist frequency, $f_{Nyq} = 5.88 \approx 5.5 lp/mm$. As expected, in Fig. 4 (b), the Anrad SMAM detector exhibits superior resolution characteristics, well beyond f_{Nyq} with a limiting frequency (at which the MTF drops to 0.1) of 10.5 lp/mm. The absolute relative errors between the simulated and measured data ($abs(\frac{(x_{sim}-x_{meas})}{x_{meas}})$) were calculated at spatial frequencies between 0.5 and 5.5 lp/mm. On average the relative error between the measured and simulated MTF is 0.3%. The MTF decreases as spatial frequencies in the image increase. This decrease is independent of the pixel size. Fig. 4(b) also shows the various components that constitute the overall MTF: $T_{pe}(f)$, $T_r(f)$ and $T_a(f)$ calculated using equations 9, 25 and 28 respectively. As shown in the figure, $T_{pe}(f)$ is almost always 1 for the entire range of spatial frequencies. This means that it has very negligible influence on the overall MTF of the imager.

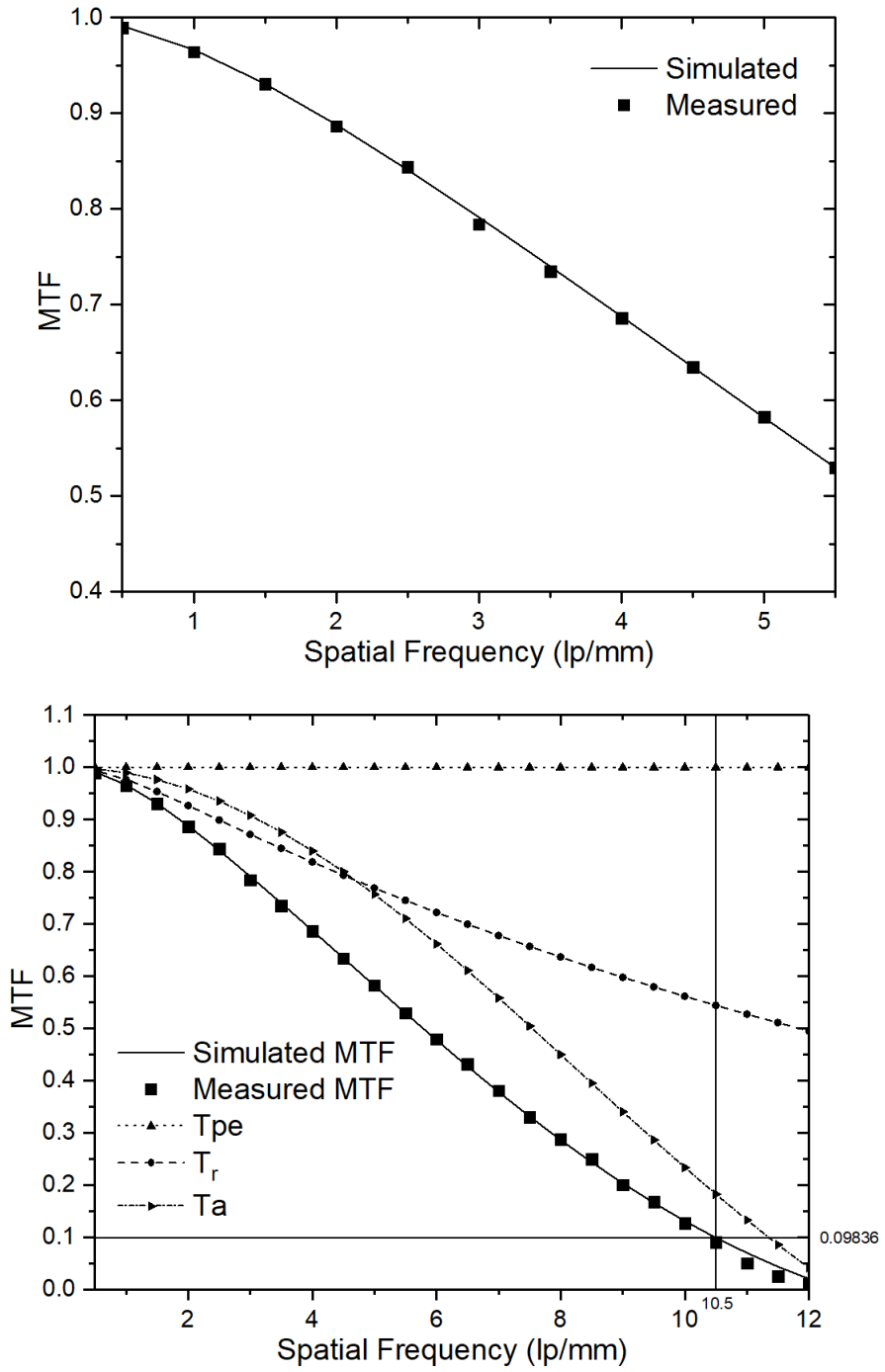

Figure A.4: Measured (symbols) and simulated (solid line) MTF curves for 85 μm a-Se/a-Si TFT PPS (Anrad SMAM) imager, obtained for a W/Al spectrum at 28 kV.

In fig. 5, the measured and simulated NNPS and DQE curves for the Anrad SMAM detector for Ka values ranging between 38 – 162 μGy are shown. It is observed that the simulated results are in close agreement with the measured NNPS and DQE. Similar to the analysis for the MTF curves, the absolute relative errors between the simulated and measured data for DQE and NNPS for different exposure levels were calculated at spatial frequencies between 0.5 and 5.5 lp/mm. On average the relative errors between the measured and simulated NNPS and DQE are 4.4% and 3.1% respectively. According to the IEC standard (IEC 62220-1-2 2007), the errors between the measured and simulated DQE curves are within acceptable limits (10%). We can observe that the NNPS does not change significantly with the spatial frequency. But DQE decreases with the increase of spatial frequency. This decrease is mainly associated with the decrease of MTF at higher frequencies, since the NNPS curves does show much dependence on change in spatial frequency.

A.4.2 Study of FOM for a-Se direct and CsI:Tl indirect a-Si TFT PPS x-ray imagers

Using equations 35-38, we calculated the DQE (f_{nyq}) for both the passive pixel sensor direct a-Se a-Si TFT PPS imagers for varying levels of electronic noise resulting from a PPS backplane and DAK. Our results, plotted in fig. 6, show that for direct a-Se imagers, at exposure levels higher than 100 μGy, the imager performance is independent of the electronic noise originating the PPS backplane. This is because as the DAK level increases, the number of incident x-ray photons increases and while the absolute noise increases, the relative noise or NNPS reduces. In fact, beyond 10 μGy, DQE (f_{nyq}) shows very little sensitivity to the electronic noise, indicating that quantum noise is the dominant source of noise making the system quantum limited. However, at lower exposures, the electronic noise originating from the PPS back-plane is more dominant since the quantum noise is low and the DQE (f_{nyq}) shows significant

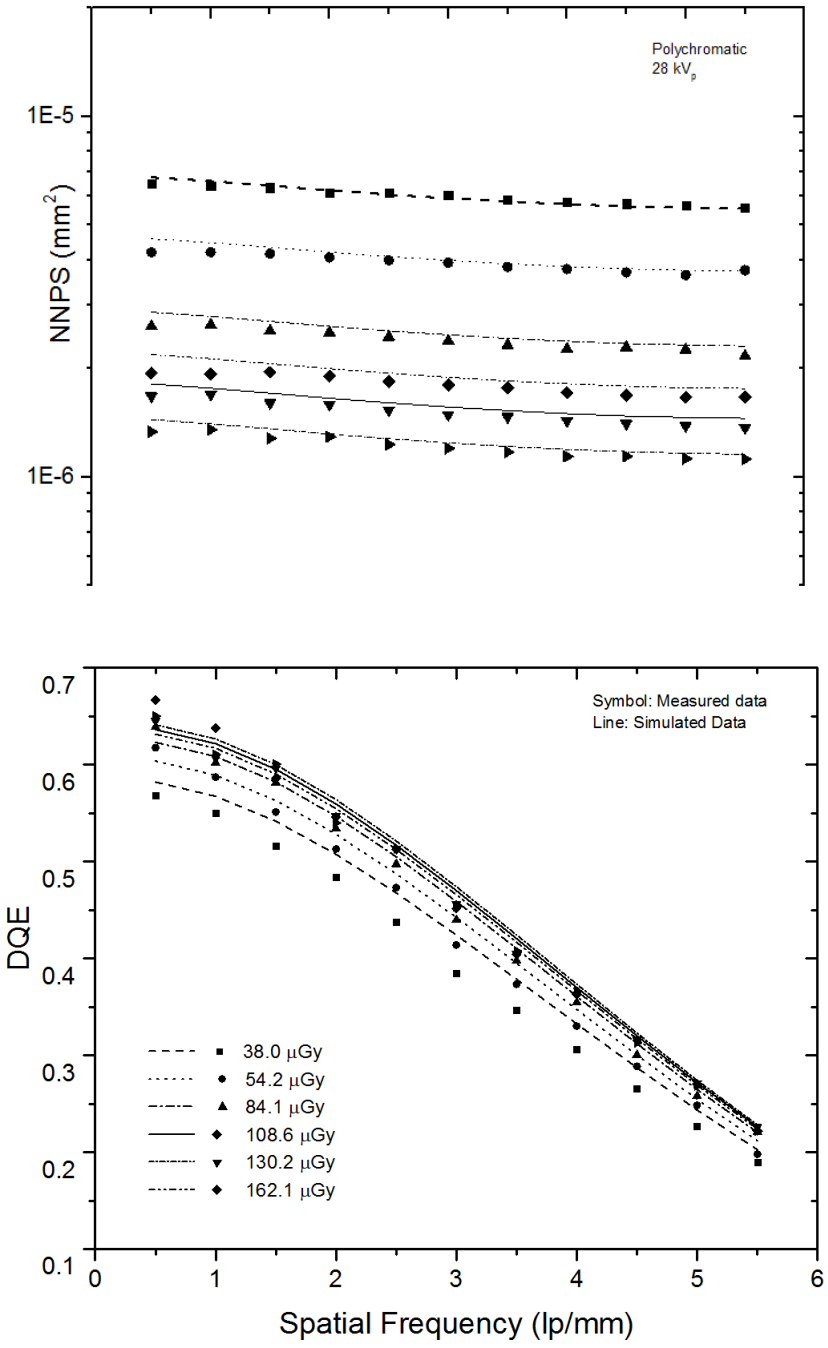

Figure A.5: Measured (symbols) and simulated (lines) NNPS (a) and DQE (b) curves for a-Se/a-Si TFT PPS (Anrad SMAM) imager at 38.0 μGy, 54.2 μGy, 84.1 μGy, 108.6 μGy , 130.2 μGy and 162.1 μGy.

deterioration as expected when the noise is increased. So there is indeed potential, in principle, to improve the DQE ($f_{nyq} = 5.5$ lp/mm) by lowering the back-plane electronic noise component.

Indeed, as shown in fig. 7, at low DAK levels (¡ 10 μGy), the direct imager displays a better performance than the indirect one for realistically achievable noise levels (¿ 1000 e^-) using a PPS backplane. This is a result of the high resolution properties (high MTF) and high gain of the direct a-Se imager. At the same time, the high MTF of the a-Se imager results in high aliasing noise which can reduce the DQE. This is observed at the low DAK levels for low electronic noise levels (¡ 400 e^-) and at higher DAK levels ($\sim$ 100 μGy), where the indirect imager seems to be superior. Additional details regarding Fig. 7 are provided in Appendix B. Hence, using DQE (f_{nyq}) as the metric for comparison, it is difficult to conclude if either the direct or indirect imager is better than the other for a wide range of electronic noise and DAK levels. This clearly establishes a need for a better metric to perform such comparison.

So, in this work, we introduced FOM as a new parameter to be used for comparison of different x-ray imaging technologies. A higher $FOM\,(1/mm^3)$ would indicate a better cumulative performance, taking into consideration all points in the frequency spectrum.We are applying this FOM parameter to compare a-Se and CsI:Tl based x-ray imagers evaluated in this work. In fig. 8, we have compared the $FOM\,(1/mm^3)$ curves for the direct and indirect imagers at varying levels of electronic noise and DAK. The linear cancaded model For all exposure levels between 0.001 and 100 μGy, the $FOM\,(1/mm^3)$ for the direct imager is consistantly higher (by at least 1.5 times) than that of the indirect imager. This can be due to higher MTF for direct imagers as compared to indirect ones, which has a direct impact on F.O.M from equation 42.

To appreciate the significance of the high electronic noise issue, it is important to study the performance of x-ray imagers at lower DAK levels. Since the signal and

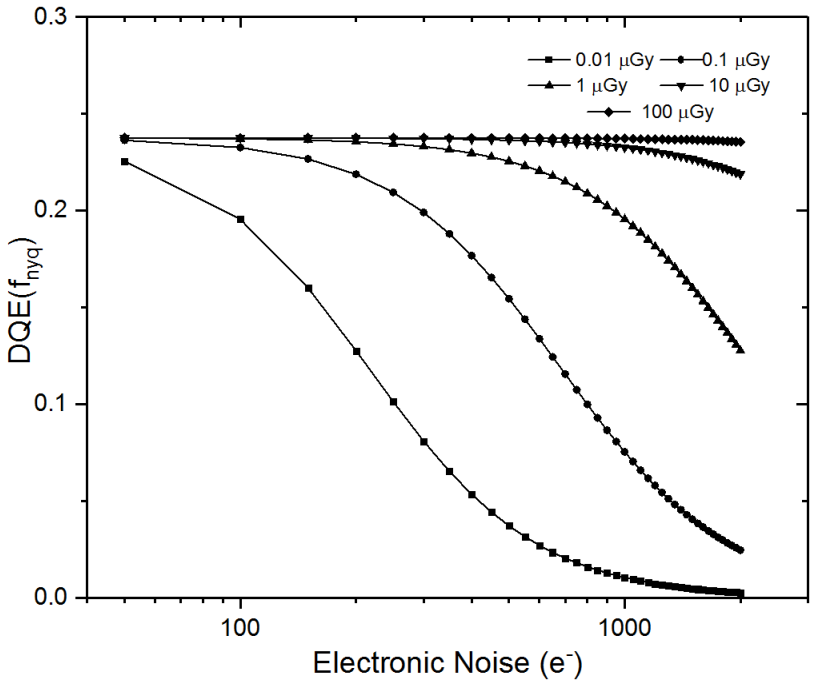

Figure A.6: Calculated variation of DQE (fnyq) versus electronic noise for a-Se a-Si TFT PPS direct x-ray imagers at various levels of electronic noise originating from a PPS back-plane and exposure.

noise response in PPS imagers is linear with respect to DAK variations *Samei and Flynn* (2003a) *El-Mohri et al.* (2007), we have used the linear cascaded systems model to simulate DQE curves for the a-Se/a-Si TFT PPS imager at DAK levels ranging from 1 to 25 μGy, which are plotted in fig. 9(a). The equations and noise levels used to obtain these plots are described in equations 34-38. From this plot, we can see that as the exposure level is reduced, the DQE decreases. For exposures below 10 μGy the DQE drops very rapidly since the noise is dominated by the PPS back-plane array electronics. For the higher exposure range the behavior is closer to be quantum limited. To ensure a quantum limited behavior even for low exposures, we propose a combination of the a-Se detector with the low noise (625 e^-) a-IGZO TFT APS back-plane array.

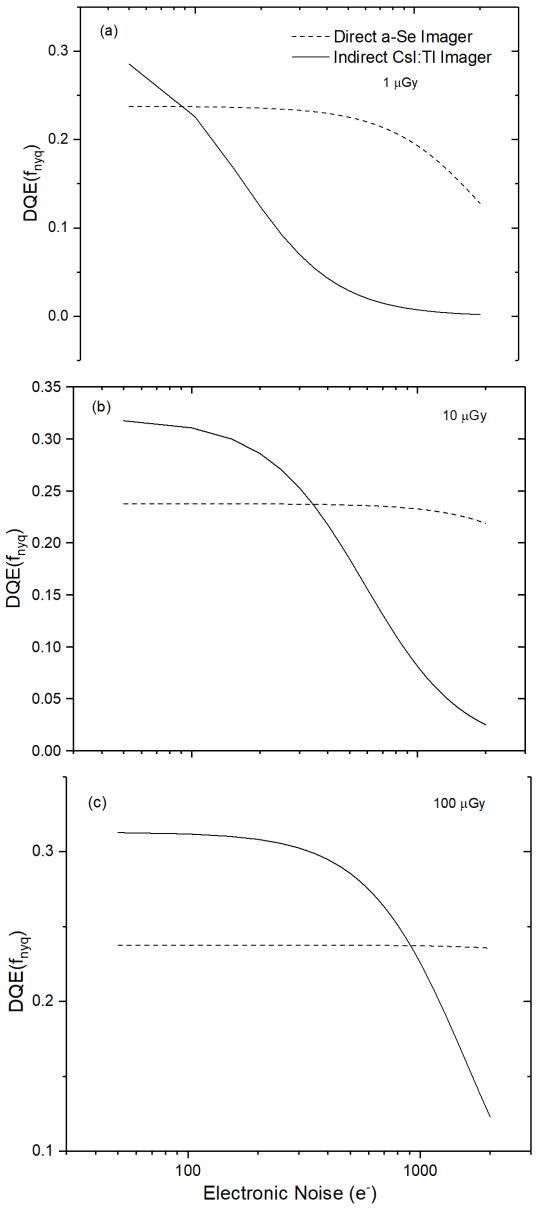

Figure A.7: Comparison of DQE (fnyq=5.5 lp/mm) from direct and indirect a-Si TFT PPS imagers at different DAK levels.

A.4.3 Study of the proposed novel x-ray imager based on a-Se detector with a-IGZO TFT APS for back-plane array

To improve the noise performance of the a-Se/ a-Si TFT PPS imager, we propose to combine the a-Se detector layer, with a low noise a-IGZO TFT APS array. The DQE of the proposed imager is calculated using equations 37, 42 and 43. As shown in

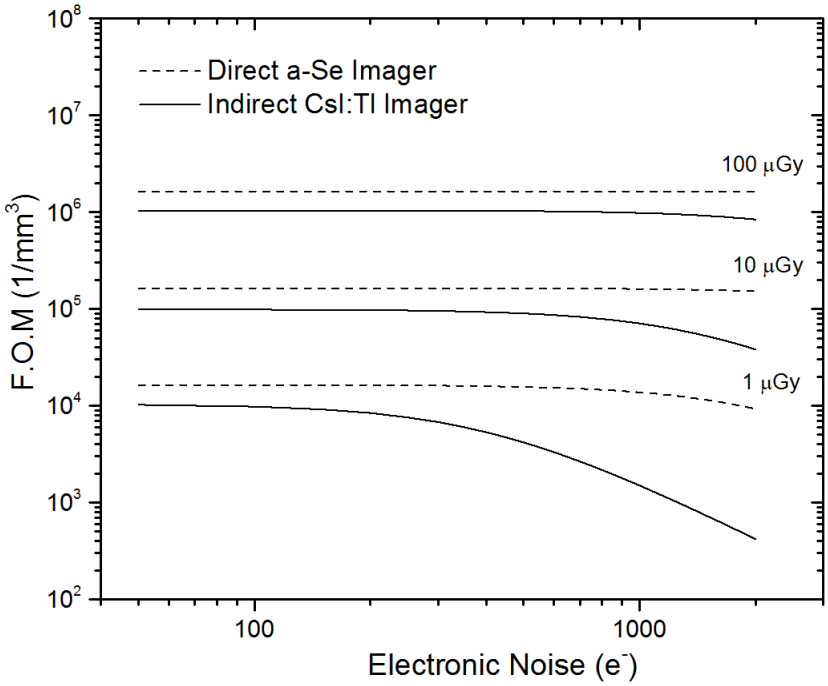

Figure A.8: Comparison of calculated FOM from direct and indirect a-Si TFT PPS detectors at different DAK levels.

fig. 9, even at the lowest exposure level of 1 μGy, the a-IGZO TFT APS back-plane array, has a higher DQE (DQE(0) increases by 0.48) as compared to the a-Si TFT PPS DQE. An improvement in a-IGZO TFT APS imager performance compared to the a-Si PPS imager can be seen by looking at the FOM values. Higher FOM values (up to 50%), at lower exposures (¡ 2 μGy) is clearly seen in fig. 10(b). To facilitate better comparisons between the indirect and direct imagers, we have plotted the DQE curves for the two imagers, at different locations in the frequency spectrum and exposure levels, as shown in the Fig. 10 (a). These curves were calculated using equations 38-40 and parameters in table 1 (direct a-Se imager) and table 2 (indirect CsI:Tl imager). From this figure, we can see that the direct imager has a higher DQE at lower frequencies, especially at higher exposures (¿ 3 μGy). The DQE at 0 lp/mm is regulated by x-ray absorption gain (Stage 1 or g_1), which is higher for the direct a-Se imager. This forces the DQE(0) for the indirect CsI:Tl imager to

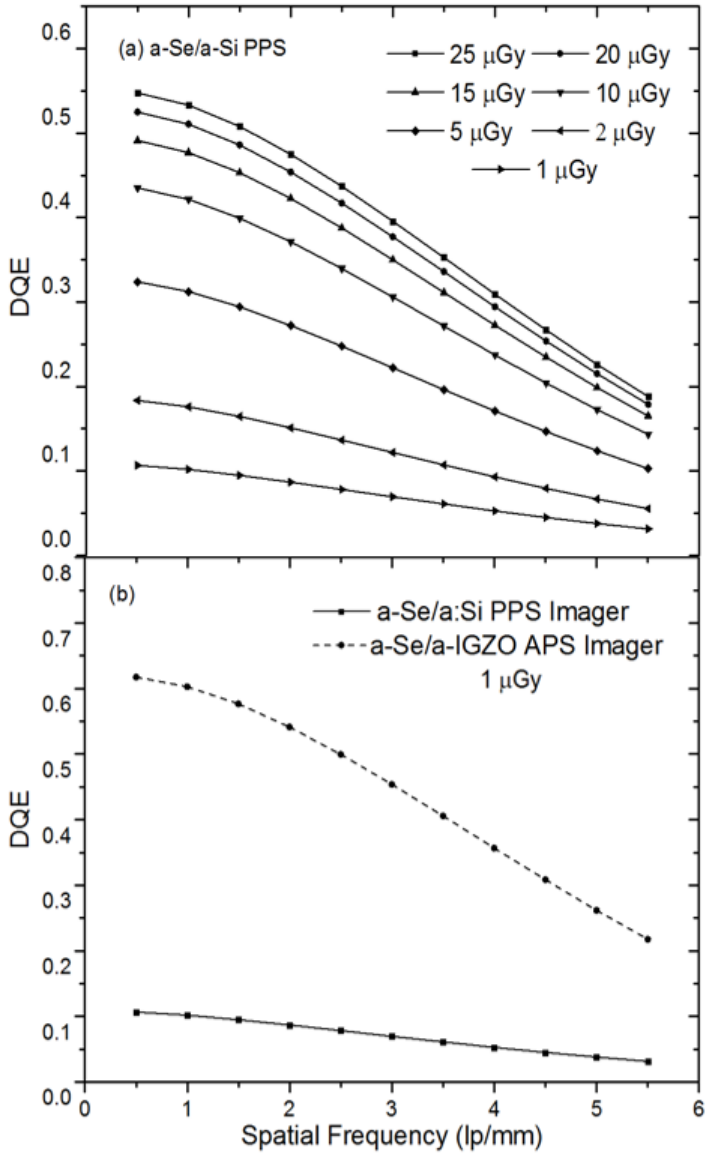

Figure A.9: (a) Calculated variation in DQE for a-Se/a-Si TFT PPS imager with decrease in exposure level and (b) DQE versus spatial frequency at 1 μGy, for a low noise a-IGZO TFT APS (625 e) and a-Si TFT PPS backplanes.

saturate faster as the DAK levels are increased. Perhaps if the x-ray spectrum is changed to maximize the x-ray absorption gain in the indirect CsI:Tl scintillator, then DQE(0) can increase beyond its current value ($\sim$ 0.47). However for higher spatial frequencies, closer to the Nyquist frequency of 5.88 lp/mm, the indirect APS

imager shows a better performance for DAK levels higher than 30 μGy. This is mainly due to strong aliasing in the direct a-Se imager, which increases the apparent noise and thus reduces the DQE. Additional details are provided in Appendix B. It should be noticed that theFOM metric is dependent on the MTF of the imager and takes into account the variation in the MTF curve at every point in the frequency spectrum. Since the MTF of the a-Se imager is higher than that of the CsI:Tl indirect imager, the overall FOM for the direct PPS imager is slightly higher than that of the indirect APS imager. Independent of the exposure level, the a-Se/a-IGZO TFT imager always has a higher FOM values as compared to the indirect CsI:Tl/a-IGZO TFT imager, shown in fig. 10(b). For low dose DBT applications, DAK levels ranging from 3 – 53 μGy are considered appropriate for obtaining each projection view (*Zhao and Zhao*, 2008). For better visualization, we have zoomed in to this exposure range in Fig. 10 (b) (inset). As shown in the figure, a-Se/a-IGZO TFT imager has the best performance in terms of FOM (it is higher by ∼10 times that the a-Se/ a-Si TFT PPS imager). In fact the a-Se/ a-Si TFT PPS imager also exhibits a better performance than the CsI:Tl/a-IGZO TFT imager. This is perhaps because FOM metric is dependent on the MTF of the imager, which is higher for the a-Se direct imager. This is mainly because for the direct imager, there is very little or almost no blurring from the photoelectric effect (fig. 4b), but the lateral scattering of optical photons in the CsI:Tl scintillator results in significant degradation of the indirect detector's MTF (*Zhao et al.*, 2015b). The obtained results support the idea that the proposed a-Se/a-IGZO TFT APS imager is a promising candidate for low dose x-ray medical imaging applications like DBT.

A.5 Discussion

In this study, we developed a linear cascaded systems model to characterize direct a-Se x-ray imagers. We found that our simulated results were within the 10% range of

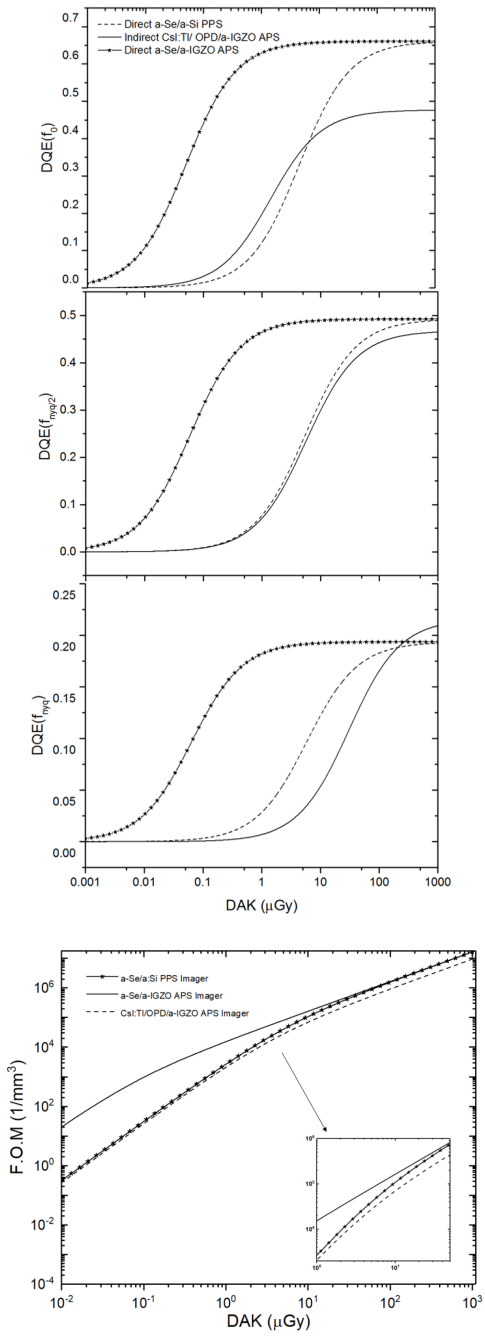

Figure A.10: (a) Comparison of DQE at various frequency positions such as 0 (f_0), 3 ($f_{nyq/2}$) and 5.5 (f_{nyq}) lp/ mm for a range of exposure levels (10^{-3} – 10^3 μGy) and (b) Comparison of FOM ($1/mm^3$) for a-Se/a-Si TFT PPS, a-Se and CsI:Tl TFT APS imagers with increasing exposure levels.

the data measured for the 85 μm a-Se/a-Si TFT PPS (Anrad SMAM) imager. For the NNPS and DQE data, the relative errors varied between 1.8% – 6.6% and 1.6%-6.6%

respectively. In general, it was observed that the relative errors in DQE was higher for lower exposure levels (38.0 μGy). We believe that the origin of the higher errors at the lower DAK levels, is the 5% mismatch in the measured and simulated values of mean x-ray photon fluence per unit DAK (6950 and 6552 photons/mm^2/μGy respectively). This deviation in the measured and simulated values of mean x-ray photon fluence per unit DAK becomes more prominent as the DAK levels are reduced, leading to the higher relative errors. It is also important to note that while our model may be a reasonable estimate of the physical imager, it is a linear model, which does not account for any non-linearity in the imaging process. However, even for non-linear systems, our model can be used to predict their behavior in response to small amplitude signals (or lower DAK levels) *Cunningham* (2000).

We used the cascaded systems model, quantified against experimental data, to study and compare the performance of direct (a-Se) and indirect (CsI:Tl) x-ray imagers at various electronic noise and DAK levels. In the previous studies *Samei and Flynn* (2003a), where physical direct and indirect imagers were compared using measured data, the additive electronic noise was unknown (or not reported) and different for the two imagers *Samei and Flynn* (2003a). Hence, it was difficult to draw a clear conclusion regarding their relative performance, as the measured data included the effect of the back-plane and/ or readout electronics. This problem was addressed through our simulations, by setting the same range of additive electronic noise (50 - 2000 e$^-$) for both x-ray imagers. When only the performance at the Nyquist frequency is considered, fig. 7 shows that the direct imager performs better than the indirect one in the following two scenarios: (a) low exposures (¡10 μGy) and (b) high exposures (¿ 100μGy) and high electronic noise (¿ 1000 e$^-$). So, it is difficult to conclude whether one imager is better than the other using DQE (f_{nyq}) as the comparison metric. It was also observed that this trend was not replicated throughout the frequency spectrum, especially at lower frequencies. In fact, when the contribution from the

entire frequency spectrum is considered (through FOM), fig. 10 shows that the direct imager consistently performs better than the indirect one for a wide range of additive electronic noise as well as DAK levels. It is possible that a lower DQE of a-Se imagers at higher frequencies is due to a high aliasing noise observed in a-Se imagers, which results in higher NNPS curves especially at higher frequencies *Ji et al.* (1998).

From fig. 8, we can see that by reducing the electronic noise (¡1000 e^-), the direct detector has the potential to perform much better especially at lower DAK levels. However, as it is difficult to achieve such low electronic noise levels with a a-Si TFT PPS back-plane, we introduced, for the first time, a low noise a-Se / a-IGZO TFT APS -imager. As shown in fig. 10 (b), the proposed imager can significantly improve the DQE at low DAK levels. This can consequently reduce the breast entrance dose levels, which becomes important for imaging applications such as DBT and computed tomography (CT) where multiple projection views are required. For the higher DAK levels, all the imagers exhibit their quantum limited behavior.

A.6 Conclusions and Future Work

In this study, the imaging performance of a-Se x-ray imagers have been analyzed through cascaded analysis. It has been shown that reducing back-plane electronic noise is critical factor to achieve improved imager performance. As a possible solution, a novel low-noise a-Se / a-IGZO TFT APS imager has been proposed and described, as the next generation x-ray imaging technology. The proposed novel imager, that can also be based on a-ITZO TFT APS technology, has the potential to significantly improve the DQE, making it an ideal candidate for low dose applications such DBT and CT. In the future, it is necessary to fabricate a small prototype based on the proposed x-ray imaging technology to demonstrate the feasibility and practicality of the proposed idea.

BIBLIOGRAPHY

BIBLIOGRAPHY

Adnani, S., A. Pil-Ali, C. C. Scott, and K. S. Karim (2021), Monte Carlo simulation of an amorphous selenium-based multi-layer photon-counting detector for spect applications., *Medical Imaging 2021: Physics of Medical Imaging*, *11595*.

Allemani, C., T. Matsuda, V. Carlo, and R. H. et al (2018), Global surveillance of trends in cancer survival 2000-14 (concord-3): analysis of individual records for 37 513 025 patients diagnosed with one of 18 cancers from 322 population-based registries in 71 countries, *Lancet 2018*, *391(10125)*, 1023–1075.

Andrey, M., L. Ikejimba, and S. J. Glick (2018), Comparison of direct-conversion a-se and csi scintillator-based cmos ffdm/dbt flat-panel detectors using an anthropomorphic breast phantom with embedded microcalcification signals., *Medical Imaging 2018: Physics of Medical Imaging.*, *10573*.

Arora, T. K., K. P. Terracina, J. Soong, M. O. Idowu, and K. Takabe (2014), Primary and secondary angiosarcoma of the breast, *Gland Surg*, *3(1)*, 28–34.

Asbeutah, A., N. Karmani, A. Asbeutah, Y. Echreshzadeh, A. A. AlMajran, and K. A.-K. KH. (2019), Comparison of digital breast tomosynthesis and digital mammography for detection of breast cancer in Kuwaiti women., *Medical Principles and Practice.*, *28(1)*, 10–5.

B. D. Gallas, IMRMC software (2013), https://github.com/DIDSR/iMRMC/releases.

Badal, A., D. Sharma, C. G. Graff, R. Zeng, and A. Badano. (2020a), Mammography and breast tomosynthesis simulator for virtual clinical trials, *Computer Physics Communications*, *264(4)*, 107,779.

Badal, A., D. Sharma, C. G. Graff, R. Zeng, and A. Badano. (2020b), Mammography and breast tomosynthesis simulator for virtual clinical trials, *Computer Physics Communications*, *264(4)*, 107,779.

Badano, A., and J. Sempau (2006), MANTIS: combined x-ray, electron and optical monte carlo simulations of indirect radiation imaging systems., *Phys Med Biol.*, *51(6)*, 1545–61.

Badano, A., M. Freed, and Y. Fang (2011), Oblique incidence effects in direct x-ray detectors: A first-order approximation using a physics-based analytical model., *Med. Phys.*, *38.4*, 2095–2098.

Badano, A., C. Graff, A. Badal, D. Sharma, R. Zeng, F. Samuelson, S. Glick, and K. J. Myers (2018), Evaluation of digital breast tomosynthesis as replacement of full-field digital mammography using an in-silico imaging trial., *JAMA network open*, *1.7*, 185,474–185,474.

Bakic, P., M. Albert, D. Brzakovic, and A. Maidment (2001), Mammogram synthesis using a 3d simulation. I. breast tissue model and image acquisition simulation, *Med Phys*, *29(9)*, 2131–2139.

Bakic, P., M. Albert, D. Brzakovic, and A. Maidment (2002), Mammogram synthesis using a 3d simulation. II. evaluation of synthetic mammogram texture, *Med Phys*, *29(9)*, 2140–2151.

Bakic, P., M. Albert, D. Brzakovic, and A. Maidment (2003), Mammogram synthesis using a three-dimensional simulation. III. modeling and evaluation of the breast ductal network, *Med Phys*, *30(7)*, 1914–1925.

Bakic, P., B. Barufaldi, and S. W. et al. (2018), Virtual clinical trial of lesion detection in digital mammography and digital breast tomosynthesis, *Proc. SPIE 10573, Medical Imaging 2018: Physics of Medical Imaging*, p. 11057306.

Bakker, M., S. de Lange, and R. P. et al. (2019), Supplemental mri screening for women with extremely dense breast tissue., *N Engl J Med*, *381(22)*, 2091–2102.

Bell, R. (2020), Mammographic density and breast cancer screening, *Climacteric*, *23(5)*, 460–465.

Bisogni, M. G., D. Bulajic, P. Delogu, M. Fantacci, M. Novelli, M. Quattrocchi, V. Rosso, and A. Stefanini (2005), Performances of different digital mammography imaging systems: Evaluation and comparison, *Nuclear Instruments and Methods in Physics Research Section A: Accelerators, Spectrometers, Detectors and Associated Equipment*, *546 (1)*, 14–18.

Bliznakova, K. (2016), Development of breast software phantom dedicated for research and educational purposes., *Radiat. Appl. Phys. Chem. Biol. Med. Sci. Eng. Environ. Sci*, *2*, 14–19.

Bliznakova, K., Z. Bliznakov, V. Bravou, Z. Kolitsi, and N. Pallikarakis (2003), A three-dimensional breast software phantom for mammography simulation., *Physics in Medicine and Biology*, *48.22*, 3699.

Bliznakova, K., et al. (2019), Development of breast lesions models database, *Physica Medica*, *64*, 293–303.

Boone, J. (2000), X-ray production, interaction, and detection in diagnostic imaging, *Handbook of medical imaging*.

Boone, J., T. Fewell, and R. Jennings (1997), Molybdenum, rhodium, and tungsten

anode spectral models using interpolating polynomials with application to mammography, *Med. Phys.*, *24(12)*, 1863–1873.

Bray, F., J. Ferlay, I. Soerjomataram, R. Siegel, L. Torre, and A. Jemal (2018), Global cancer statistics 2018: Globocan estimates of incidence and mortality worldwide for 36 cancers in 185 countries, *CA: Cancer J Clin.*, *68*, 394–424.

Bray, F., M. Laversanne, E. Weiderpass, and I. Soerjomataram (2021), The ever-increasing importance of cancer as a leading cause of premature death worldwide., *Cancer*, *127(16)*, 3029–30.

Bushberg, Siebert, Leiholdt, and Boone (2012), *The essential physics of medical imaging*, 239 pp., Lippincott Williams & Wilkins, Philadelphia, USA.

Carney, P., et al. (2003), Individual and combined effects of age, breast density, and hormone replacement therapy use on the accuracy of screening mammography, *Ann Intern Med*, *138*, 168–175.

Chaplain, M. A. J. (1996), Avascular growth, angiogenesis and vascular growth in solid tumours: The mathematical modelling of the stages of tumour development, *Mathematical Computer Modelling*, *23(6)*, 47–87.

Cheng, M., C. Zhao, C. Huang, H. Kim, M. Nakata, and J. Kanicki (2016), Amorphous InSnZno thin-film transistor voltage-mode active pixel sensor circuits for indirect x-ray imagers, *IEEE Transactions on Electron Devices*, *63*, 4802–4810.

Cheng, M. H., C. Zhao, and J. Kanicki (2017), Study of current-mode active pixel sensor circuits using amorphous InSnZno thin-film transistor for 50-μm pixel-pitch indirect x-ray imagers, *Solid-State Electronics*, *131*, 53–64.

Ciatto, S., N. Houssami, and D. B. et al (2013), Integration of 3d digital mam-

mography with tomosynthesis for population breast-cancer screening (storm): a prospective comparison study, *Lancet Oncol*, *14(7)*, 583–589.

Coleman, W. (2019), Breast ductal carcinoma in situ: Precursor to invasive breast cancer., *The American journal of pathology*, *189(5)*, 942–945.

Cunningham, I. (2000), Applied linear-systems theory, *Handbook of medical imaging*, *1*, 79–159.

Cunningham, I. A., M. Westmore, and A. Fenster (1994), A spatial-frequency dependent quantum accounting diagram and detective quantum efficiency model of signal and noise propagation in cascaded imaging systems, *Med. Phys.*, *21(3)*, 417–427.

Darbandi, A., E. Devoie, D. Matteo, and O. Rubel (2012), Modeling the radiation ionization energy and energy resolution of trigonal and amorphous selenium from first principles, *Journal of Physics: Condensed Matter*, *19*, 455,502.

de Sisternes, L., J. Brankov, and A. Zysk (2015), A computational model to generate simulated three-dimensional breast masses, *Medical Physics*, *42.2*, 1098–1118.

Donini, B., S. Rivetti, N. Lanconelli, and M. Bertolini (2014), Free software for performing physical analysis of systems for digital radiography and mammography., *Med. Phys.*, *41(5)*, 051,903.

Duffy, S., L. Tabar, and H. C. et al (2002), The impact of organized mammography service screening on breast carcinoma mortality in seven swedish counties, *Cancer 2002*, *95*, 458–469.

Dukov, N., K. Bliznakova, F. Feradov, I. Buliev, H. Bosmans, G. Mettivier, P. Russo, L. Cockmartin, and Z. Bliznakov (2019), Models of breast lesions based on three-dimensional x-ray breast images, *Physica Medica*, *57*, 80–87.

El-Mohri, Y., L. Antonuk, Q. Zhao, Y. Wang, Y. Li, H. Du, and A. Sawant (2007), Performance of a high fill factor, indirect detection prototype flat-panel imager for mammography, *Med. Phys*, *34*, 315–327.

Elangovan, P., F. Alrehily, R. F. Pinto, A. Rashidnasab, D. R. Dance, K. C. Young, and K. Wells (2016a), Simulation of spiculated breast lesions, *Medical Imaging 2016: Physics of Medical Imaging*, *9783*, 97,832.

Elangovan, P., A. Hadjipanteli, A. Mackenzie, D. Dance, K. Young, and K. Wells (2016b), Optimam image simulation toolbox - recent developments and ongoing studies, *International Workshop on Breast Imaging*, pp. 668–675.

Erbas, B., E. Provenzano, J. Armes, and D. Gertig (2006), The natural history of ductal carcinoma in situ of the breast: a review., *Breast cancer research and treatment.*, *97(2)*, 135–44.

Esposito, M., T. Anaxagora, A. Konstantinidis, , N. Allinson, and K. Wells (2014), Performance of a novel wafer scale cmos active pixel sensor for bio-medical imaging, *Phys. Med. Biol.*, *59(13)*, 3533.

Fang, Y., A. Badal, N. Allec, K. Karim, and A. Badano (2012), Spatiotemporal Monte Carlo transport methods in x-ray semiconductor detectors: Application to pulse-height spectroscopy in a-se., *Medical physics*, *39(1)*, 308–19.

Farrier, M., T. G. Achterkirchen, G. Weckler, and A. M. A. (2009), Very large area CMOS active-pixel sensor for digital radiography, *IEEE Trans. Electron. Devices*, *56*, 2623–31.

Fessler, J. (2015), Image reconstruction toolbox, https://web.eecs.umich.edu/ fessler/code/index.html.

Freed, M., S. Park, A. Badano, and J. Sempau (2010), A fast, angle-dependent, analytical model of CsI detector response for optimization of 3D x-ray breast imaging systems., *Med. Phys.*, *37(6)*, 2593–2605.

Frieboes, H., F. Jin, Y.-L. Chuang, S. Wise, J. Lowengrub, and V. Cristini (2010), Three-dimensional multispecies nonlinear tumor growth–ii: Tumor invasion and angiogenesis, *J Theor Biol.*, *264(4)*, 1254–1278.

Garg, I., and M. Miga (2008), Preliminary investigation of the inhibitory effects of mechanical stress in tumor growth, *Medical Imaging 2008: Visualization, Image-Guided Procedures, and Modeling.*, *6918*.

Gavaghan, G., J. Brady, C. Behrenbruch, R. Highnam, and P. Maini (2002), Breast cancer: Modelling and detection, *Journal of Theoretical Medicine*, *4(1)*, 3–20.

Gefen, A., and B. Dilmoney (2007), Mechanics of the normal woman's breast, *Technol Health Care*, *15(4)*, 259–271.

Gilbert, F., L. Tucker, M. Gillan, P. Willsher, and J. C. et al (2015), Accuracy of digital breast tomosynthesis for depicting breast cancer subgroups in a uk retrospective reading study (tommy trial), *Breast Imaging*, *277*, 697–706.

Ginsburg, O., et al. (2020), Breast cancer early detection: A phased approach to implementation., *Cancer*, *126*, 2379–2393.

Graff, C. (2016), A new open-source multi-modality digital breast phantom, *Proc. SPIE. Medical Imaging 2016: Physics of Medical Imaging.*, *9783*, 978,309–978,310.

Griff, S. K., and D. D. Dershaw (2002), *Oncology Imaging (Second Edition)*, Springer Science and Business Media.

Hamamatsu C9732DK CMOS PPS Detector (2015), https://www.hamamatsu.com/us/en/product/type/C9732DK-11/index.html.

Helmlinger, G., P. Netti, H. Lichtenbeld, R. Melder, and R. Jain (1997), Solid stress inhibits the growth of multicellular tumor spheroids., *Nat Biotechnol.*, *58(17)*, 778–83.

Hintsala, H., K. Bliznakova, N. Pallikarakis, and T. Jamsa (2009), Modelling of irregular breast lesions., *World Congress on Medical Physics and Biomedical Engineering*, pp. 2024–2027.

Howansky, A., B. Peng, A. R. Lubinsky, and W. Zhao (2017), Deriving depth-dependent light escape efficiency and optical swank factor from measured pulse height spectra of scintillators, *Med. Phys.*, *44(3)*, 847–860.

Hunter, D., et al. (2007), The dependence of the modulation transfer function on the blocking layer thickness in amorphous selenium x-ray detectors, *Med. Phys*, *34*, 3358–3373.

Hunter, M., G. Belev, S. Kasap, and J. Yaffe (2012), Measured and calculated K-fluorescence effects on the mtf of an amorphous-selenium based CCD x-ray detector, *Med. Phys*, *39*, 608–622.

III, J. T. D. (2009), Tomosynthesis imaging: At a translational crossroads, *Med. Phys.*, *36*, 1956–1967.

Iranmakani, S., T. Mortezazadeh, F. Sajadian, M. Ghaziani, A. Ghafari, D. Khezerloo, and A. Musa (2020), A review of various modalities in breast imaging: technical aspects and clinical outcomes, *Egyptian Journal of Radiology and Nuclear Medicine*, *51*.

Jacobsen, K., E. O'Meara, D. Key, D. Buist, K. Kerlikowske, I. V. aand B Sprague, E. Lynge, and M. Euler-Chelpin (2015), Comparing sensitivity and specificity of screening mammography in the united states and denmark, *Int. J. Cancer*, *137*, 2198–2207.

Jain, R. K. (1987), Transport of molecules in the tumor interstitium: a review, *Cancer research*, *47(12)*, 3039–3051.

Jatoi, I., and P. Pinsky (2020), Breast cancer screening trials: Endpoints and overdiagnosis., *JNCI: Journal of the National Cancer Institute*.

Jemal, A., F. Bray, M. Center, J. Ferlay, E. Ward, and D. Forman (2011), Global cancer statistics., *CA Cancer J Clin*, *61(2)*, 69–90.

Jeong, J., et al. (2008), 1-Inch WXGA AMOLED display driven by indium-gallium-zinc oxide TFTs array., *SID Symposium Digest of Technical Papers*, *39(1)*, 1–4.

Ji, W., W. Zhao, and J. Rowlands (1998), Digital x-ray imaging using amorphous selenium: Reduction of aliasing, *Med. Phys*, *25*, 2148–2162.

Kabir, M., and S. Kasap (2003), Modulation transfer function of photoconductive x-ray image detectors: effects of charge carrier trapping, *J. Phys. D, Appl. Phys*, *36*, 2352–2358.

Kabir, M., W. Mahmudur, and W. Shen (2011), Modelling of detective quantum efficiency of direct conversion x-ray imaging detectors incorporating charge carrier trapping and K-fluorescence, *IET circuits, devices and systems*, *5*, 222–231.

Karim, S. K., A. Nathan, and J. A. Rowlands (2002), Active pixel sensor architectures in a-sih for medical imaging, *Journal of Vacuum Science and Technology A: Vacuum, Surfaces, and Films*, *20(3)*, 1095–1099.

Kasap, S., et al. (2011), Amorphous and polycrystalline photoconductors for direct conversion flat panel x-ray image sensors, *Sensors*, *11*, 5112–5157.

Keavey, E., N. Phelan, A. O'Connell, F. Flanagan, A. O'Doherty, A. Larke, and A. Connors (2012), Comparison of the clinical performance of three digital mam-

mography systems in a breast cancer screening programme., *Br J Radiol.*, *85(1016)*, 1123–1127.

Kim, H. (2017), *Organic Photodiodes and Their Optoelectronic Application*, Doctoral dissertation, University of Michigan.

Kim, H., S. Yun, J. Ko, and G. Cho (2008), Cascade modeling of pixelated scintillator detectors for x-ray imaging, *IEEE Transactions on Nuclear Science*, *55(3)*, 1357–1366.

Kondo, S., and R. Asal (1995), A reaction-diffusion wave on the skin of the marine angelfish pomacanthus, *Nature*, *376(6543)*, 765–8.

Konstantinidis, A. (2011), *Evaluation of digital X-ray detectors for medical imaging applications*, Doctoral dissertation, UCL (University College London).

Konstantinidis, A., M. Szafraniec, R. Speller, and A. Olivo (2012), The dexela 2923 cmos x-ray detector: a flat panel detector based on cmos active pixel sensors for medical imaging applications, *Nucl. Instrum. Methods A*, *689*, 12–21.

Langendijk, J. A., N. K. Aaronson, J. M. A. D. Jong, G. P. M. T. Velde, M. J. Muller, R. J. Lamers, B. J. Slotman, and E. F. M. Wouters (2001), Phase ii study of vinorelbine in patients with malignant pleural mesothelioma., *Journal of Clinical Oncology*, *19(8)*, 2123–2133.

Lee, C., and W. McCaskill-Stevens (2020), Tomosynthesis mammographic imaging screening trial (tmist): An invitation and opportunity for the national medical association community to shape the future of precision screening for breast cancer, *Journal of the national medical association*.

Lee, C., D. Dershaw, D. Kopans, and et el (2010), Breast cancer screening with imaging: Recommendations from the society of breast imaging and the acr on the

use of mammography, breast mri, breast ultrasound, and other technologies for the detection of clinically occult breast cancer, *J Am Coll Radiol*, *7*, 18–27.

Leeser, M., S. Mukherjee, and J. Brock (2014), Fast reconstruction of 3d volumes from 2d ct projection data with gpus., *BMC Res Notes*, *7*, 582.

Li, S., J. Zhang, H. Yang, C. Wu, X. Dang, and Y. Liu (2015), Copper depletion inhibits $cocl_2$-induced aggressive phenotype of mcf_7 cells via down regulation of hif_1 and inhibition of snail/twist-mediated epithelial-mesenchymal transition, *Scientific Reports*, *5*, 12,410.

Lujan, E., M. S. Rosito, A. Soba, and C. Suarez (2019), Libregrowth: A tumor growth code based on reaction–diffusion equations using shared memory, *Computer Physics Communications*, *243*, 97–105.

Maas, S., B. Ellis, G. Ateshian, and J. Weiss (2012), Febio: finite elements for biomechanics., *J Biomech Eng.*, *134(1)*, 011,005.

Mackenzie, A., N. Marshall, A. Hadjipanteli, D. Dance, H. Bosmans, and K. Young (2017), Characterisation of noise and sharpness of images from four digital breast tomosynthesis systems for simulation of images for virtual clinical trials, *Phys. Med. Biol.*, *62*, 2376–2397.

Mackenzie, A., et al. (2015), Breast cancer detection rates using four different types of mammography detectors, *Eur Radiol.*, *26(3)*, 874–883.

Madhav, M., S. Nayagam, K. Biyani, and et al (2018), Epidemiologic analysis of breast cancer incidence, prevalence, and mortality in india. protocol for a systematic review and meta-analyses, *Medicine (Baltimore)*, *97(52).*, 13,680.

Mahato, S., J. D. Ridder, G. Meynants, G. Raskin, and H. V. Winckel (2018), Kernel-

based crosstalk quantification and analysis of a CMOS image sensor., *In Optical Sensing and Detection V*, *10680*, 1068,004.

Marconi, V., F. Pipan, L. Tomkova, A. Nitti, R. Girometti, and C. Zuiani (2019), Comparison of synthetic mammography and digital mammography, in association with digital breast tomosynthesis in the attribution of bi-rads categories, *European Congress of Radiology*.

MATLAB Codes Repository (2022), https://github.com/DIDSR/Lesion-Growth-Prerelease.

MATLAB Documentation (2006), https://www.mathworks.com/help/.

McDonald, E., A. Oustimov, S. Weinstein, M. Synnestvedt, M. Schnall, and E. Conant (2016), Effectiveness of digital breast tomosynthesis compared with digital mammography: outcomes analysis from 3 years of breast cancer screening., *JAMA oncology.*, *2(6)*, 737–43.

Metal Oxide TFT Backplanes for Displays 2014-2024: Technologies, Forecasts, Players: IDTechX (2014), https://www.idtechex.com/research/reports/metal-oxide-tft-backplanes-for-displays-2014-2024-technologies-forecasts-players-000405.asp.

Monnin, P., D. Gutierrez, S. Bulling, D. Guntern, and F. R. Verdun (2007), A comparison of the performance of digital mammography systems, *Med. Phys.*, *34(3)*, 906–914.

Moss, S., M. Summerley, B. Thomas, R. Ellman, and J. Chamberlain (1992), A case-control evaluation of the effect of breast cancer screening in the united kingdom trial of early detection of breast cancer., *J Epidemiol Commun Health*, *46*, 362–364.

Nystrom, L., L. Rutqvist, and S. W. et al. (1993), Breast cancer screening with mammography: overview of swedish randomized trials., *Lancet*, *341*, 973–8.

Oduko, J., and A. Mackenzie. (2019), Technical evaluation of GE healthcare senographe pristina digital mammography system in 2d mode (nhsbsp equipment report)., *Public Health England, London*.

Osoba, D., M. Brada, W. K. A. Yung, and M. Prados (2000), Health-related quality of life in patients treated with temozolomide versus procarbazine for recurrent glioblastoma multiforme, *Journal of Clinical Oncology*, *18(7)*, 1481–1491.

Pisano, E. (2018), Is tomosynthesis the future of breast cancer screening?, *Radiology*, *278*, 147–48.

Que, W., and J. Rowlands (1995a), X-ray imaging using amorphous selenium: Inherent spatial resolution, *Med. Phys.*, *22(4)*, 365–374.

Que, W., and J. Rowlands (1995b), X-ray imaging using amorphous selenium: Inherent spatial resolution, *Med. Phys*, *22*, 365–374.

Rabbani, M., and R. Metter (1989), Analysis of signal and noise propagation for several imaging mechanisms, *JOSA A*, *6 (8)*, 1156–1164.

Rabbani, M., R. Metter, and R. Shaw (1987), Detective quantum efficiency of imaging systems with amplifying and scattering mechanisms, *JOSA A*, *4 (5)*, 895–901.

RadIcon 2013 RadEye1 (2013), www.rad-icon.com/products-radeye.php/.

Rafferty, E., J. Park, L. Philpotts, S. Poplack, J. Sumkin, E. Halpern, and L. Niklason (2018), Assessing radiologist performance using combined digital mammography and breast tomosynthesis compared with digital mammography alone: Results of a multicenter, multireader trial, *Radiology*, *266(1)*, 104–113.

Rashidnasab, A., P. Elangovan, M. Yip, O. Diaz, D. R. Dance, K. C. Young, and K. Wells (2013), Simulation and assessment of realistic breast lesions using fractal growth models., *Physics in Medicine and Biology*, *58*, 5613–5627.

Risom, T., et al. (2021), Transition to invasive breast cancer is associated with progressive changes in the structure and composition of tumor stroma., *bioRxiv*.

Rowlands, J., G. Decrescenzo, and Araj (1992), X-ray imaging using amorphous selenium: Determination of x-ray sensitivity by pulse height spectroscopy, *Med. Phys*, *19*, 1065–1069.

Sakorafas, G., and A. Tsiotou (2000), Ductal carcinoma in situ (dcis) of the breast: evolving perspectives., *Cancer treatment reviews.*, *26(2)*, 103–125.

Salvat, F., J. M. Fernandez-Varea, and J. Sempau (2006), Penelope - a code system for monte carlo simulation of electron and photon transport, *Nuclear Energy Agency (OECD) Issy-les-Moulineaux*.

Samei, E., and Flynn (2003a), An experimental comparison of detector performance for direct and indirect digital radiography systems, *Med. Phys*, *30*, 608–622.

Samei, E., and M. Flynn (2003b), An experimental comparison of detector performance for direct and indirect digital radiography systems, *Med. Phys.*, *30(4)*, 608–622.

Sauer, T., E. Samei, and A. Bejan (2020), Cell and extracellular matrix growth theory and its implications for tumorigenesis., *Biosystems*, *201*, 104,331.

Sechopoulos, I. (2013), A review of breast tomosynthesis. part i. the image acquisition process, *Med. Phys.*, *40(1)*, 014,301–12.

Sechopoulos, I., and A. Athanasiou (2020), Digital breast tomosynthesis screening: Better but still not good enough for all women, *Radiology*, p. 203494.

Sengupta, A., and A. Badano (2021), In situ tumor model for longitudinal in silico imaging trials, *IEEE Transactions on Biomedical Engineering*.

Sengupta, A., R. Zeng, D. Sharma, and A. Badano (2018), The first freely available open source software package for performing 3d image reconstruction for digital breast tomosynthesis., *Proc SPIE.*, p. 10573.

Sengupta, A., C. Zhao, A. Konstantinidis, and J. Kanicki (2019), Cascaded systems analysis of a-Se/a-Si and a-InGaZnO TFT passive and active pixel sensors for tomosynthesis, *Phys Med Biol.*, *64(2)*, 025,012.

Sengupta, A., D. Sharma, and A. Badano (2021), Computational model of tumor growth for in silico trials, *Medical Imaging 2021: Physics of Medical Imaging 2021*.

Sengupta, A., A. Badal, and A. Badano (2022), Computational models of digital mammography and breast tomosynthesis systems for in silico imaging trials, *Medical Imaging 2018: Physics of Medical Imaging*, *12345*.

Seto, A. A., and L. Mardiyana (2019), Intrinsic subtypes of breast cancer in malignant speculating mass on mammography., *Int J Radiol Radiat Ther.*, *6(4)*, 144–148.

Shapiro, S., W. Venet, P. Strax, and L. Venet (1988), Periodic screening for breast cancer: the health insurance plan project and its sequelae, 1963-1986., *Baltimore, Md: Johns Hopkins University Press*.

Sharma, D., and A. Badano (2013), Validation of columnar CsI x-ray detector responses obtained with hybridMANTIS, a CPU-GPU Monte Carlo code for coupled x-ray, electron, and optical transport., *Medical physics*, *40.3*, 031,907.

Sharma, D., A. Badal, and A. Badano (2012), hybridMANTIS: a CPU-GPU Monte Carlo method for modeling indirect x-ray detectors with columnar scintillators., *Phys Med Biol.*, *57(8)*, 2357–72.

Sharma, D., C. Graff, A. Badal, R. Zeng, P. Sawant, A. Sengupta, E. Dahal, and

A. Badano (2019), In silico imaging tools from the victre clinical trial., *Medical Physics*, *46.9*, 3924–3928.

Siewerdsen, J., L. Antonuk, Y. El-Mohri, J. Yorkston, W. Huang, J. Boudry, and I. Cunningham (1997), Empirical and theoretical investigation of the noise performance of indirect detection, active matrix flat-panel imagers (AMFPIs) for diagnostic radiology, *Med. Phys*, *24*, 71–89.

Skaane, P., A. Bandos, R. Gullien, E. Ebben, and U. E. et al (2013), Prospective trial comparing full-field digital mammography (ffdm) versus combined ffdm and tomosynthesis in a population-based screening programme using independent double reading with arbitration, *European Radiology*, *23*, 2061–2071.

Stafford, R., and G. Whitman (2011), Ultrasound physics and technology in breast imaging, *Ultrasound Clinics*, *6(3)*, 299–312.

Steele, J. P., J. Shamash, M. T. Evans, N. H. Gower, M. D. Tischkowitza, and R. M. Rudd (2000), Phase ii study of vinorelbine in patients with malignant pleural mesothelioma., *Journal of Clinical Oncology*, *18(23)*, 3912–7.

Stein, A., T. Demuth, D. Mobley, M. Berens, and L. Sander (2007), A mathematical model of glioblastoma tumor spheroid invasion in a three-dimensional in vitro experiment., *Biophys J.*, *92(1)*, 356–365.

Su, X., C. Cui, W. Xu, Z. Wei, J. Fei, and L. Li (2017), Non-calcified ductal carcinoma in situ of the breast: comparison of diagnostic accuracy of digital breast tomosynthesis, digital mammography, and ultrasonography, *Breast Cancer*, *24*, 562–570.

Sung, H., J. Ferlay, R. Siegel, M. Laversanne, I. Soerjomataram, A. Jemal, and F. Bray (2020), Global cancer statistics 2020: Globocan estimates of incidence and mortality worldwide for 36 cancers in 185 countries, *CA: Cancer J Clin.*, *71(3)*, 209–249.

Tang, L., A. Ven, D. Guo, V. Andasari, V. Cristini, K. C. Li, and X. Zhou (2014), Computational Modeling of 3D Tumor Growth and Angiogenesis for Chemotherapy Evaluation, *PLOS ONE*, *9*, 83,962–83,974.

Turing, A. (1952), The chemical basis of morphogenesis, *Phil. Trans. R. Soc. Lond. B*, *237*, 37–72.

Vancoillie, L., N. Marshall, n. J. V. L Cockmartin L, G. Zhang, and H. Bosmans (2020), Verification of the accuracy of a hybrid breast imaging simulation framework for virtual clinical trial applications., *Journal of Medical Imaging*, *7(4)*, 042,804.

VICTRE Github Repository (2018), https://github.com/DIDSR/VICTRE.

Warren, L., A. Mackenzie, J. Cooke, R. Given-Wilson, M. Wallis, D. Chakraborty, D. R. Dance, H. Bosmans, and K. Young (2012), Effect of image quality on calcification detection in digital mammography., *Med. Phys.*, *39(6)*, 3202–3213.

Wei, W., Y. Zhang, and Q. X. et al. (2017), Monolithic integration of hybrid perovskite single crystals with heterogenous substrate for highly sensitive x-ray imaging., *Nature Photon*, *11*.

Weis, J., M. Miga, L. Arlinghaus, X. Li, A. Chakravarthy, V. Abramson, J. Farley, and T. Yankeelov (2013a), A mechanically coupled reaction–diffusion model for predicting the response of breast tumors to neoadjuvant chemotherapy., *Phys. Med. Biol.*, *58(17)*, 5851.

Weis, J., M. Miga, L. Arlinghaus, X. Li, A. Chakravarthy, V. Abramson, J. Farley, and T. Yankeelov (2013b), A mechanically coupled reaction–diffusion model for predicting the response of breast tumors to neoadjuvant chemotherapy., *Physics in Medicine and Biology.*, *58(17)*, 5851.

Yaffe, M. J., and J. A. Rowlands (1997), X-ray detectors for digital radiography, *Phys. Med. Biol.*, *42(1)*, 1–39.

Yan, H., M. Romero-Lopez, L. I. Benitez, K. Di, H. B. Frieboes, C. C. W. Hughes, D. A. Bota, and J. S. Lowengrub (2017), 3d mathematical modeling of glioblastoma suggests that transdifferentiated vascular endothelial cells mediate resistance to current standard-of-care therapy, *Integrated Systems and Technologies: Mathematical Oncology*, *77(15)*, 4171–4184.

Zeng, R., S. Park, P. Bakic, and K. Myers (2015), Evaluating the sensitivity of the optimization of acquisition geometry to the choice of reconstruction algorithm in digital breast tomosynthesis through a simulation study, *Phys. Med. Biol.*, *60*, 1259 – 1288.

Zeng, R., F. Samuelson, D. Sharma, A. Badal, C. Graff, S. Glick, K. Myers, and A. Badano (2020), Computational reader design and statistical performance evaluation of an in-silico imaging clinical trial comparing digital breast tomosynthesis with full-field digital mammography., *Journal of Medical Imaging*, *7(4)*, 042,802.

Zhao, B. (2007), *Breast tomosynthesis with amorphous selenium digital flat panel detector*, Doctoral dissertation.

Zhao, B., and W. Zhao (2008), Imaging performance of an amorphous selenium digital mammography detector in a breast tomosynthesis system, *Med. Phys*, *35*, 1978–1987.

Zhao, C., and J. Kanicki (2014), Amorphous In–Ga–Zn–O thin-film transistor active pixel sensor x-ray imager for digital breast tomosynthesis, *Med. Phys.*, *41(9)*, 14–18.

Zhao, C., , J. Kanicki, A. Konstantinidis, and T. Patel (2015a), Large area CMOS active pixel sensor x-ray imager for digital breast tomosynthesis: Analysis, modeling and characterization, *Med. Phys.*, *42 (11)*, 6294–6308.

Zhao, C., J. Kanicki, A. Konstantinidis, and T. Patel (2015b), Large area CMOS active pixel sensor x-ray imager for digital breast tomosynthesis: Analysis, modeling and characterization, *Med. Phys*, *42*, 6294–6308.

Zhao, C., A. Konstantinidis, Y. Zheng, T. Anaxagoras, R. Speller, and J. Kanicki (2015c), 50 μm pixel pitch wafer-scale cmos active pixel sensor x-ray detector for digital breast tomosynthesis, *Phys. Med. Biol.*, *60*, 8977.

Zhao, W., and J. Rowlands (1995), X-ray imaging using amorphous selenium: Feasibility of a flat panel self-scanned detector for digital radiology., *Phys Med Biol.*, *22(10)*, 1595–1604.

Zhao, W., and J. Rowlands (1997), Digital radiology using active matrix readout of amorphous selenium: Theoretical analysis of detective quantum efficiency, *Med. Phys*, *24*, 1819–1833.

Zhao, W., W. Ji, A. Debrie, and J. Rowlands (2003), Imaging performance of amorphous selenium based flat-panel detectors for digital mammography: Characterization of a small area prototype detector, *Med. Phys*, *30*, 254–263.

Zuley, M., A. Bandos, M. Ganott, J. Sumkin, and A. K. et al (2013), Digital breast tomosynthesis versus supplemental diagnostic mammographic views for evaluation of noncalcified breast lesions, *Breast Cancer*, *266*, 89–95.